Mon. Not. R. Astron. Soc. **392,** 1295–1338 (2009) doi:10.1111/j.1365-2966.2008.14148.x

GEMINI 3D spectroscopy of BAL + IR + Fe II QSOs – I. Decoupling the BAL, QSO, starburst, NLR, supergiant bubbles and galactic wind in Mrk 231

S. Lipari,[1⋆] S. F. Sanchez,[2] M. Bergmann,[3] R. Terlevich,[4,5] B. Garcia-Lorenzo,[6] B. Punsly,[7] E. Mediavilla,[6] Y. Taniguchi,[8] M. Ajiki,[8] W. Zheng,[9] J. Acosta[6] and K. Jahnke[10]

[1]*Córdoba Observatory and CONICET, Laprida 854, 5000 Córdoba, Argentina*
[2]*Calar Alto Observatory, C/Jesus Durban Remon 2-2, E-04004 Almeria, Spain*
[3]*Gemini Observatory, La Serena, Chile*
[4]*Institute of Astronomy, Madingley Road, Cambridge CB3 OHA*
[5]*Instituto Nacional de Astrofisica Optica y Electronica (INAOE), Puebla, Mexico*
[6]*Instituto de Astrofisica de Canarias, 38205 La Laguna, Tenerife, Spain*
[7]*Centre for Relativistic Astrophysics, University of Rome La Sapienza, Italy and USA*
[8]*Astronomical Institute, Tohoku University, Aoba, Sendai 980-8578, and Ehime Universiy, Matsuyama, Japan*
[9]*Department of Physics and Astronomy, John Hopkins University, Baltimore, MD 21218, USA*
[10]*Astrophysics Institute of Potsdam, An der Sternwarte 16, 14482 Potsdam, Germany*

Accepted 2008 October 24. Received 2008 October 24; in original form 2005 November 16

ABSTRACT

In this paper we present the first results of a study of BAL QSOs (at low and high redshift), based on very deep Gemini GMOS integral field spectroscopy. In particular, the results obtained for the nearest BAL IR–QSO Mrk 231 are presented.

For the nuclear region of Mrk 231, the QSO and host galaxy components were modelled, using a new technique of decoupling 3D spectra. From this study, the following main results were found: (i) in the pure host galaxy spectrum an extreme nuclear starburst component was clearly observed, as a very strong increase in the flux, at the blue wavelengths; (ii) the BAL system I is observed in the spectrum of the host galaxy; (iii) in the clean/pure QSO emission spectrum, only broad lines were detected. 3D GMOS individual spectra (specially in the near-infrared Ca II triplet) and maps confirm the presence of an extreme and young nuclear starburst ($8 <$ age < 15 Myr), which was detected in a ring or toroid with a radius $r = 0.3$ arcsec $\sim$ 200 pc, around the core of the nucleus. The extreme continuum blue component was detected only to the south of the core of the nucleus. This area is coincident with the region where we previously suggested that the galactic wind is cleaning the nuclear dust.

Very deep 3D spectra and maps clearly show that the BAL systems I and II – in the strong '*absorption lines*' Na IDλ5889–95 and Ca II Kλ3933 – are extended (reaching $\sim$1.4–1.6 arcsec $\sim$ 1.2–1.3 kpc, from the nucleus) and clearly elongated at the position angle (PA) close to the radio jet PA, which suggest that the BAL systems I and II are 'both' associated with the radio jet.

The physical properties of the four expanding nuclear bubbles were analysed, using the GMOS 3D spectra and maps. In particular, we found strong multiple LINER/OF emission-line systems and Wolf–Rayet features in the main knots of the more external super bubble S1 ($r = 3.0$ kpc). The kinematics of these knots – and the internal bubbles – suggest that they are associated with an area of rupture of the shell S1 (at the south-west). In addition, in the more internal superbubble S4 and close to the core of the nucleus (for $r < 0.7$ arcsec ~ 0.6 kpc), two similar narrow emission-line systems were detected, with strong [S II] and [O I] emission and $\Delta V \sim -200$ km s^{-1}. These results suggest that an important part of the nuclear NLR is generated by the OF process and the associated low-velocity ionizing shocks.

⋆E-mail: sllipari@gmail.com

Finally, the nature of the composite BAL systems and very extended OF process – of 50 kpc – in Mrk 231 (and similar QSOs) are discussed. In addition, the '*composite hyperwind scenario*' (already proposed for BALs) is suggested for the origin of giant Lyα blobs. The importance of study the end phases of Mrk 231, and similar evolving elliptical galaxies and QSOs (i.e. galaxy remnants) is discussed.

Key words: ISM: bubble – galaxies: individual: Mrk 231 – quasars: absorption lines – galaxies: starburst.

1 INTRODUCTION

Theoretical models based on the hierarchical clustering scenario suggest that the first generation (i.e. Population III) massive stars could be born around $z = 30$ (0.5 Gyr after the big bang) and the galactic systems with masses higher than 10^{10} M$_\odot$ could be assembled at $z = 5$–10. On the other hand, there is increasing evidence that galactic outflow (OF) and BAL systems play a main role in the high-redshift universe, at $z > 5$ (Frye, Broadhurst & Benitez 2002; Maiolino et al. 2003, 2004a,b; Lípari et al. 2005, 2007a,b). Thus, a main step for the study of QSO and galaxy formation at high redshift is to understand the extreme OFs, BAL processes and explosions from very massive stars in nearby QSOs/galaxies. Motivated by this, our group began a program on investigations of BAL, OF and galactic winds (GWs) in nearby infrared (IR) QSOs and mergers (see for references Lípari et al. 2003, 2005, 2007a,b).

An evolutionary and composite scenario was proposed for BAL + IR + Fe II QSOs (by Lípari 1994; Lípari, Colina & Macchetto 1994; Lípari et al. 2003, 2005; Lípari & Terlevich 2006). Where mergers fuel extreme star formation processes and active galactic nuclei (AGN), resulting in strong dust and IR emission, large numbers of supernova (SN) and hypernova events (probably in the accretion discs and/or in the nuclear starburst ring/toroid) with expanding supergiant bubbles and shell. The BALs in IR + Fe II QSOs were associated with this composite nature of the OF process and young QSOs. In addition, it is important to remark that several works also suggested an evolutionary scenario for BALs/QSOs systems (see Hamann & Ferland 1993; Voit, Weymann & Korista 1993; Egami et al. 1996).

Mrk 231 is the nearest BAL + IR + Fe II + GW QSO. Specifically, it shows very interesting spectral characteristics, dominated in the optical by extremely strong Fe II and broad Balmer emission lines at $Z_{\rm em} \sim 0.042$, plus remarkable absorption-line systems. In particular, Mrk 231 shows two types of absorption-line systems: a clear stellar absorption at $Z_{\rm abs} \sim 0.042$ plus at least three strong broad absorption-line (BAL) systems. These strong BAL systems show the following velocity of ejection: $V_{\rm eject}$ of BAL I, II and III of ∼4700, ∼6000 and ∼8000 km s^{-1}, respectively (see for details and references Lípari et al. 2005, 2006).

On the other hand, Mrk 231 is one of the most luminous IR object in the local universe, with $L_{\rm IR[8-1000\,\mu m]} = 3.56 \times 10^{12}\,{\rm L}_\odot$, $L_{\rm IR}/L_B = 32$, $M_K = -24.7$ and $M_V = -22.5$ (Markarian 1969; Adams 1972; Rieke & Low 1972, 1975; Boksenberg et al. 1977; Cutri, Rieke & Lebofsky 1984 and others). The origin of this extreme IR luminosity is associated with the two main sources of nuclear energy: an AGN plus an extreme nuclear and circumnuclear starburst (see Lípari et al. 1994, 2005, 2006).

Throughout the paper, a Hubble constant of $H_0 = 75$ km s^{-1} Mpc^{-1} will be assumed. For Mrk 231 we adopted the distance of ∼168 Mpc (from Lípari et al. 2005 and from this paper: Sections 3, 11 and 12). This distance was obtained from the stellar absorption lines and the main emission-line component, with a final value of redshift $z = 0.042\,18$ and $cz = 12\,654 \pm 10$ km s^{-1}. Thus, the angular scale is 1 arcsec ≈ 814 pc.

2 GEMINI PROGRAMME OF BAL QSOS

In this paper we present the first results from a new part of our observational programme of BAL QSOs: a study of high spatial and spectral resolution of 3D Gemini spectroscopy of nearby BAL + IR + Fe II QSOs, selected from our data base of IR QSOs/mergers OF (Lípari et al. 2004c, 2005). We have observed seven nearby and high-z BAL QSOs, from our original sample of more than 50 IR QSOs/mergers with OF, plus submillinetre + radio Sloan Digital Sky Survey (SDSS) QSOs.

The general goal of this programme is to study the kinematics, physical conditions and morphology of the gas and the stars in the very nucleus of BAL + IR + Fe II QSOs. Some of the particular goals of this programme can be enumerated as follows.

(i) To study BALs associated with composite QSOs: AGN + starburst (with jet + accretions discs, shells). Specifically, to study in detail our finding that some BALs systems are linked with: (1) bipolar OF probably generated by subrelativistic jets (Lípari et al. 2005; Punsly & Lípari 2005) and (2) supergiant explosive events, probably associated with hypernovae (Lípari et al. 2005).

Our purpose is to study the spatial distribution, and the kinematics and physical properties of the ionized gas, stars and dust, all of which provide information about the evolutionary conditions of the interstellar medium (ISM) and the possible origins of extreme star formation and explosive processes.

(ii) To investigate the presence, properties, origin and importance of GWs, stellar populations and giant explosions in BAL + IR + Fe II QSOs/mergers.

In particular, it is important to study in detail the host galaxies of BAL + IR QSOs, specially the presence of GWs, young stellar populations [with Wolf–Rayet (WR) features, etc.], SN, HyN and giant arcs/shells.

(iii) To study possible links or evolutionary paths among mergers, starbursts, BAL, QSOs and galaxies. More specifically, to analyse the possible connection between IR mergers with extreme starburst + GW leading to IR composite QSOs with GW, and elliptical galaxies.

We have a special interest in studying the evolutionary role of IR QSOs with BAL + giant galactic shells (plus strong Fe II emission). These IR QSOs were defined as *composite and transition* objects between ULIRGs and standard QSOs, in the IRAS colour–colour diagram (Lípari 1994; Lípari et al. 2005): figs 5 and 15, respectively); e.g. Mrk 231, IRAS 07598+6508, IRAS 17002+5153, IRAS 04505−2958 and others.

Table 1. Journal of observations of Mrk 231.

Object	Date	Telescope/ instrument	Spectral region	Exposure time (s)	Comments
Gem data (north)					
Mrk 231	2005 April 06	8.1 m Gemini/GMOS–IFU	R831, λλ5750–7850 Å	900×1	Nucleus, ⟨FWHM⟩ = 0.7–0.8 arcsec
Mrk 231	2005 April 06	8.1 m Gemini/GMOS–IFU	R831, λλ5750–7850 Å	900×1	Arc, ⟨FWHM⟩ = 0.7–0.8 arcsec
Mrk 231	2005 April 30	8.1 m Gemini/GMOS–IFU	B600, λλ3420–6200 Å	1800×2	Nucleus, ⟨FWHM⟩ = 0.4–0.5 arcsec
Mrk 231	2005 April 30	8.1 m Gemini/GMOS–IFU	B600, λλ3420–6200 Å	1500×2	Arc, ⟨FWHM⟩ = 0.4–0.5 arcsec
Mrk 231	2005 April 30	8.1 m Gemini/GMOS–IFU	B600, λλ4550–7400 Å	1200×2	Nucleus, ⟨FWHM⟩ = 0.4–0.5 arcsec
Mrk 231	2005 April 30	8.1 m Gemini/GMOS–IFU	B600, λλ4550–7400 Å	900×2	Arc, ⟨FWHM⟩ = 0.4–0.5 arcsec
Mrk 231	2005 April 30	8.1 m Gemini/GMOS–IFU	R831, λλ7750–9850 Å	900×1	Nucleus, ⟨FWHM⟩ = 0.4–0.5 arcsec
HST data (archive)					
Mrk 231	1995 October 23	*HST*/WFPC2	F439W, λλ4283/464 Å	2226	⟨FWHM⟩ = 0.1 arcsec
Mrk 231	1995 October 23	*HST*/WFPC2	F814W, λ λ8203/1758 Å	712	⟨FWHM⟩ = 0.1 arcsec
Mrk 231	2003 March 17	*HST*/ACS	F330W, λ λ3354/588 Å	1140	⟨FWHM⟩ = 0.1 arcsec
Mrk 231	2003 September 09	*HST*/NICMOS	F160W, λ λ1.60/0.40 μm	640	⟨FWHM⟩ = 0.22 arcsec
Mrk 231	1992 November 27	*HST*/FOS	G190H, λλ1275–2320 Å	5760	
Mrk 231	1992 November 27	*HST*/FOS	G270H, λ λ2225–3295 Å	2880	
Mrk 231	1996 November 21	*HST*/FOS	G160L, λ λ1150–2300 Å	770	
WHT data La Palma					
Mrk 231	2001 April 12	4.2 m WHT/INTEGRAL	λλ6200–7600 Å	1800×3	⟨FWHM⟩ = 1.0 arcsec
NOT data La Palma					
Mrk 231	1991 May 11	2.5 m NOT	*V*	1200×3	⟨FWHM⟩ = 0.7 arcsec
KPNO Data					
Mrk 231	1991 February 15	2.15 m KPNO/GoldCam	λλ3350–5200 Å	900×2	PA = 90°, slit width = 1.5 arcsec
		2.15 m KPNO/GoldCam	λλ5100–7100 Å	900×2	PA = 90°, slit width = 1.5 arcsec

(iv) To study the origin of low-ionization BAL systems observed in IR QSOs (Boroson & Meyer 1992; Lípari 1994; Lípari et al. 1994). These absorption systems can be explained within the framework of the composite (starburst + AGN) OF scenario. We are particularly interested in making a detailed study of our proposition that some BAL systems and extreme Fe II emission could be associated with GWs that produce dusty expanding shells.

A second programme of this research is the study of OF/BAL in forming galaxies and QSOs at high redshift ($z > 2$). We are studying very deep 3D spectroscopic data of submillimetre and radio SDSS BAL QSOs, using Gemini + GMOS and ESO VLT + VIMOS. It is important to remark that some luminous submillimetre source at high z imply in the rest-frame luminous IR sources. Thus, probably we are studying the same type of objects in both programmes. We have already observed three high-z BAL QSOs.

3 GEMMINI OBSERVATIONS AND DATA REDUCTION

3.1 Gemini GMOS–IFU observations

The 3D deep optical spectroscopy of the nucleus and the more extended arc of Mrk 231 was obtained during two photometric nights in 2005 April, at the 8.1-m telescope in Gemini-North Observatory. The telescope was used with the Gemini Multi-Object Spectrograph (GMOS) in the mode integral field unit (IFU; Allington-Smith et al. 2002). The spectra covered all the optical wavelength range: from 3400 to 10 000 Å. The observations were made in photometric conditions, and with seeing in the ranges of ∼0.4–0.6 arcsec (in the observing run of 2005 April 30) and ∼0.7–0.8 arcsec (in 2005 April 6). For details of each observations, see Table 1.

The data were obtained with the IFU in one slit mode, which provide a spatial field of 3.5 × 5.0 arcsec^2 for each resulting science data cube. With this observing configuration, the GMOS–IFU comprises 750 fibres; each spans a 0.2 arcsec hexagonal region of the sky. 500 fibres make up the 3.5 × 5.0 arcsec^2 science field of view; and 250 fibres make up a smaller, dedicated sky field, which is fixed at 1 arcmin of distance of the science position (Allington-Smith et al. 2002). We used in the first night the R831 grating in GMOS, which has a ∼40 km s^{-1} spectral resolution. In addition, the B600 grating was used in the second night, which has a ∼120 km s^{-1} spectral resolution.

Very deep 3D spectra were obtained for all the observations the B600 grating, for this bright QSO. The typical exposure time were of ∼1 h (for the nucleus and for the arc, see for details Table 1). These very deep observations were performed in order to study multiple components in the OF/BAL process, the spectrum of the host galaxy, the extreme nuclear starburst (with massive star population) and the knots in the expanding shells/bubbles.

3.2 Reduction and analysis of Gemini GMOS–IFU data

The following software packages were used to reduce and to analyse the GMOS–IFU data: R3D + EURO3D visualization tool,[1] IRAF[2] and GEMINI.[3]

The 3D GMOS–IFU spectroscopic observations were reduced using a modified version of R3D software package (Sanchez & Cardiel 2005; Sanchez 2006). This reduction process was performed following the standard steps: (1) the data were bias subtracted; (2) the expected location of the spectra were traced on a continuum lamp exposure obtained before each target exposure; (3) the fibre-to-fibre response at each wavelength was determined from a continuum lamp exposure; (4) wavelength calibration was performed using arc lamp spectra and the telluric emission line in the science data; (5) the sky background spectrum was estimated before subtraction by averaging spectra of object-free areas; (6) the calibration flux was done using the observation of standard stars and (7) the observations of the nucleus and the arc (for the corresponding gratings) were then combined in mosaics. A total of 14 700 spectra – of Mrk 231 and sky – were reduced and calibrated, using this technique.

After this basic reduction process, a data cube was created for each exposure and for each mosaic. The cubes were then recentred spatially by determining the position of the core of the nucleus of Mrk 231. This recentring corrects for differential atmospheric refraction (DAR). It is important to note that we already performed a detailed study of the effect of the atmospheric refraction in the position of the core of the nucleus in 3D spectroscopy (for different wavelengths: from 7800 to 4200 Å; Arribas et al. 1997, their fig. 4a). From this study, a variation in the position of the core of the nucleus of ∼1.5 arcsec was found, at La Palma WHT. Therefore, for the very high spatial resolution GMOS data (and covering a very large wavelength range) it is important the recentring process.

To generate 2D maps of any spectral feature (intensity, velocity, width, etc.) the IDA and INTEGRAL software tools (García-Lorenzo et al. 2002) were used. We have found that the IDA package gets better results recovering 2D maps from low signal-to-noise ratio (S/N) data. The IDA interpolation is performed using the IDL standard routine TRIGRID, which uses a method of bivariate interpolation and smooth surface fitting for irregularly distributed data points (Akima 1978). Maps generated in this way are presented in the following sections.

In addition, we used the software SPECFIT,[4] plus SPLOT; both from the IRAF and STSDAS[5] packages. An example of SPECFIT deblending, using three components for each emission line in IRAS 01003−2238, was shown in fig. 2 of Lípari et al. (2003). In each GMOS spectrum the presence of OF components and multiple emission-line systems were confirmed by detecting these systems in at least two or three different emission lines ([N II]λ6583, Hα, [N II] λ6548, [S II]λλ6717/31, [O I]λ6300, [O III]λ5007 and Hβ).

Finally, it is important to note that in general the main parameters of the spectra [i.e. the fluxes, equivalent widths (EqWs), S/N, errors/σ, etc.] were carefully measured and their errors analysed using different software tasks described previously: i.e. R3D, EURO-3D, GEMINI-GMOS, IRAF, IDA, INTEGRAL, STSDAS, SPECFIT, GALFIT-3D, etc. In general, we follow for the analysis of the errors/σ, S/N, etc. the mathematical algorithms described in detail by Roederer (1963) and Bevington (1969). For the study of the kinematics, the ADHOC[6] software package was also used. For the analysis of the errors/σ in the kinematics, mainly the prescriptions suggested by Keel (1996) were used.

3.3 The GMOS–IFU mosaic of Mrk 231

Fig. 1 – NOT V wide field image – shows together the whole merger and the observed GMOS mosaics (in orange colour, and covering an area of ∼3.5 × 9.0 arcsec^2, ∼3 × 7.3 kpc). This mosaic was constructed by combining two individual Gemini + GMOS–IFU frame (of 3.5 × 5.0 arcsec^2). The first GMOS frame was centred in the core of the nucleus of Mrk 231, and the second one in the more extended bubble/arc (at 4 arcsec to the south, from the core of the nucleus).

Fig. 1 shows that Mrk 231 consists of a nearly elliptical main body (of $R \sim 10$ kpc) with a compact nucleus, plus two faint tidal tails (see for details Hamilton & Keel 1987; Neff & Ulvestad 1988; Lípari et al. 1994). Therefore, the GMOS mosaic covers the nuclear and circumnuclear region of the IR merger.

3.4 Multiple components in the GMOS–IFU emission-line spectra

An important point in the study of spectra obtained with relatively high spectral resolution is the analysis of multiple components (in each emission line, especially in the stronger lines [N II]λ6583 and Hα). This type of detailed study was performed for several nearby galaxies, including systems with OF process, e.g. NGC 1052, 3079, 3256, 4550, 5514, 7332, Cen A, etc. (e.g. Bland, Taylor & Atherton 1987; Veilleux et al. 1994; Plana & Boulesteix 1996; Lípari et al. 2000, 2004d, 2005). For Mrk 231, using the 3D GMOS spectra with high and moderate spectral resolution (R831 and B600 grating with spectral resolution of ∼40 and 120 km s^{-1}, respectively), a detailed study of multiple emission-line components was performed (especially in order to analyse OF motion). Fig. 2 shows the presence of these multiple emission (and stellar absorption) line systems.

In particular, from this study – of multiple component – the following main results were obtained.

(i) *Main component in the emission lines (MC-EMI, MC-EMI*)*

In the nucleus and the circumnuclear region of Mrk 231 a single strong/main emission-line component (MC-EMI) was detected. This ELC was measured and deblended using the software SPLOT (see Section 3.2). For this MC-EMI a redshift at $z = 0.042\,50$ (12 750 km s^{-1}) was measured.

In addition, at the south-west nuclear and circumnuclear regions (of the GMOS mosaic) this main component (MC-EMI*) was detected with a clear blueshift at $z = 0.042\,20$ (12 600 km s^{-1}).

(ii) *Blue OF emission components (OF-EB1, OF-EB2*, OF-EB3**

The presence of several strong OF components was observed, specially in the main knots of the supergiant shells. These ELCs are blueshifted, in relation to the systemic velocity and the

[1] R3D is the imaging analysis software facility developed by us at Calar Alto Observatory (Sanchez & Cardiel 2005; Sanchez 2006). EURO3D visualization tool is a software package for integral field spectroscopy, developed by EURO3D Research Training Network (Sanchez 2004).

[2] IRAF is the imaging analysis software developed by NOAO.

[3] GEMINI is the reduction and analysis software facility developed by Gemini Observatory.

[4] SPECFIT was developed and is kindly provided by Gerard A. Kriss.

[5] STSDAS is the reduction and analysis software facility developed by the Space Telescope Science Institute.

[6] ADHOC is a 2D/3D kinematics analysis software developed by Dr J. Boulesteix at Marseille Observatory.

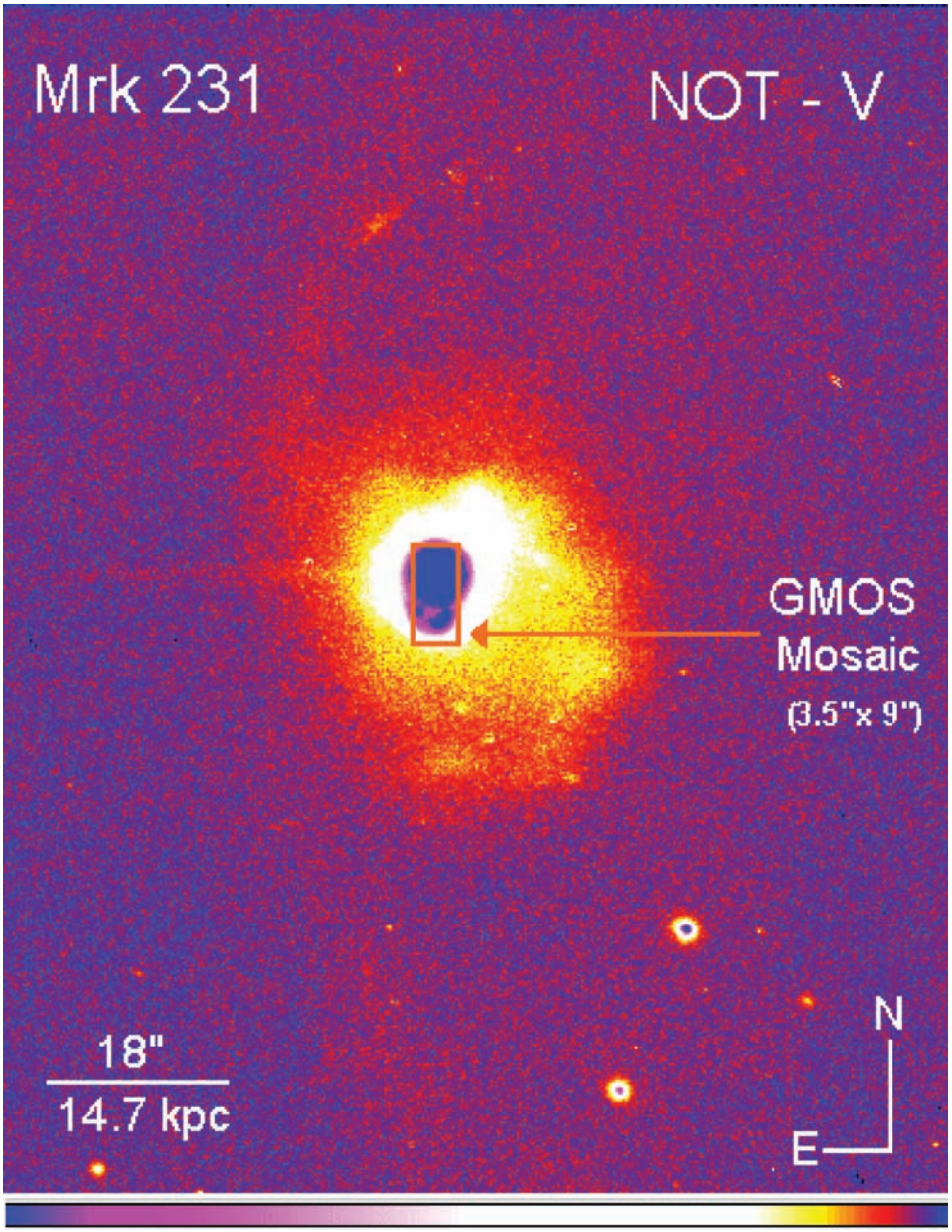

Figure 1. *V* broad-band image of the main body and the faint tails of Mrk 231 (obtained at the 2.5 NOT telescope, La Palma Spain) showing the mosaic field observed with Gemini + GMOS. This figure is adapted from Lípari et al. (2005).

MC-EMI of the merger; and they were deblended using the software SPECFIT.

(1) *OF-EB1*: This is a low-velocity blue OF component, which was detected in almost all the main knots of the four supergiant bubbles. We have measured for OF-EB1 a range of values of redshifts $z = [0.041\,40, 0.042\,10]$ (12 470, 12 630 km s^{-1}), $\Delta V = V$(OF-EB1) $- V$(MC-EMI) $= [-150, -300]$ km s^{-1}.

(2) *OF-EB2**: This is an intermediate velocity blue OF component, which was detected only in the main knots located in the south-west region of the four more external supergiant bubbles. We have measured for OF-EB2* a redshift $z = 0.040\,80$ (12 240 km s^{-1}), $\Delta V = V$(OF-EB2*) $- V$(MC-EMI*) $= -400$ km s^{-1}.

(3) *OF-EB3**: This is an extreme blue OF component, which was detected in the south-west border of our GMOS mosaic (we call this region as SW1, which is located at [1.7 arcsec west, 5.6 arcsec south]). We have measured for OF-EB3* a redshift $z = 0.039\,20$ ($cz = 11\,774$ km s^{-1}), $\Delta V = V$(OF-EB3*) $- V$(MC-EMI*) $= -905$ km s^{-1}.

(iii) *Red outflow component in the emission line (OF-ER1)*

This is a low-velocity red OF component, which was detected in the circumnuclear areas and in some knots of the supergiant bubbles. We have measured for OF-ER1 a range of redshifts $z = [0.042\,98, 0.043\,33]$ (12 895, 12 998 km s^{-1}), $\Delta V = V$(OF-ER1) $- V$(MC-EMI) $= [+150, +250]$ km s^{-1}.

In conclusion, with the spectral resolution of this study we can identify at least six different emission-line systems. These results are specially important for the study of the OF process of the multiple expanding supergiant bubbles/shells, and also for the generation and interpretation of the velocity fields (VFs) and emission-line ratio (ELR) maps.

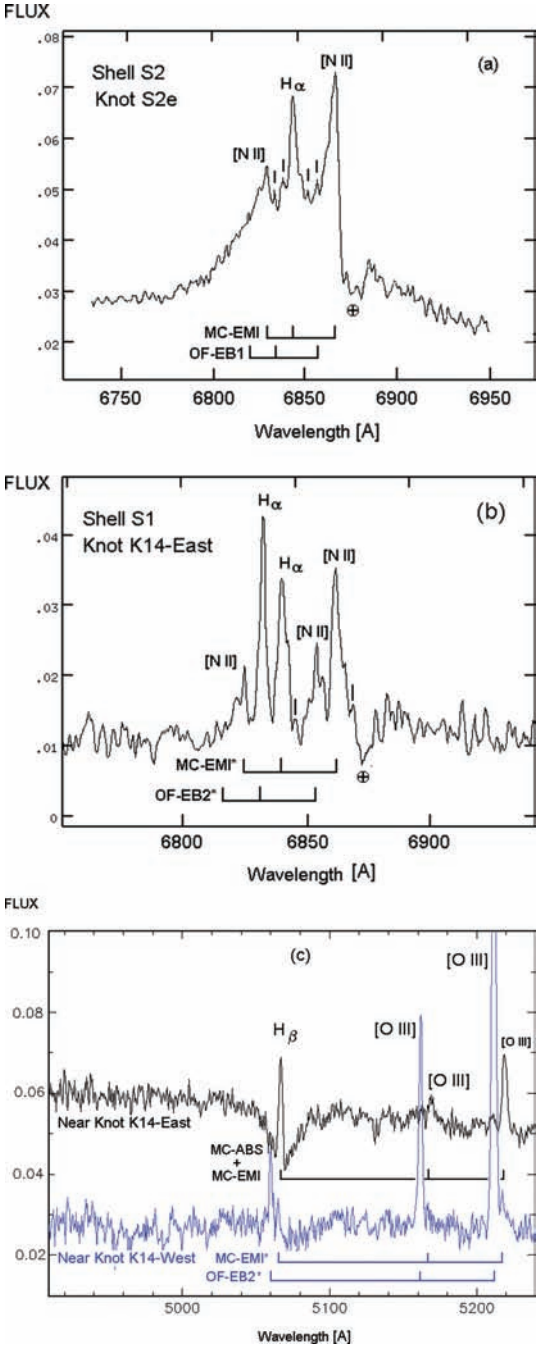

Figure 2. Example of GMOS spectra with multi or different emission and absorption-line components. The scales of flux are given in units of (erg cm^{-2} s^{-1} Å^{-1} $\times$ 10^{-16}). The tick marks show the positions of the peaks of different emission-line components (in panel 2a the upper tick marks show OF components). See the text (Section 3.4) for details of the main components (MC) and OF; of the emission and/or absorption lines (EMI, ABS).

4 *HST*-ARCHIVE DATA AND OUR PREVIOUS OBSERVATIONS

It is important to remark that the high spectral and spatial resolution GMOS observations – of Mrk 231 – were obtained in order to continue and to test our previous studies (which were performed at moderate/low spatial and spectral resolution, but for wide spatial fields). Therefore, in this paper is essential to compare the Gemini results with those obtained previously.

The technical details of our previous observations of Mrk 231 (obtained at La Palma/WHT, La Palma/NOT and Keat Peak/GoldCam) and the used archive data [from *Hubble Space Telescope* (*HST*)/WFPC2, *HST*/ACS, *HST*/NICMOS and *HST*/FOS] were already described by Lípari et al. (2005). However, in Table 1 a summary of these observations are presented. In addition, it is interesting to note that Lípari & Terlevich (2006) presented an evolutionary model for AGN and QSOs, in which a main point is the composite nature in the core of the nucleus of BAL + IR + Fe II QSOs. Thus, the Gemini plus previous data of Mrk 231 are an important test for the evolutionary theoretical model of composite AGN/QSOs.

5 DECOUPLING THE GMOS–IFU NUCLEAR SPECTRUM: HOST, QSO AND BAL COMPONENTS

Very recently, a new method for decoupling the spectra of the QSOs/AGN from the host galaxies – using 3D spectroscopy – was developed by us (see for references and details Wisotzki et al. 2003; Jahnke et al. 2004; Sanchez et al. 2004; Wisotzki et al. 2004; Garcia-Lorenzo et al. 2005; Sanchez et al. 2006a,b). Using this technique the clean 3D spectra of the host stellar population could be obtained.

The pure 3D spectra of the host galaxy combined with stellar population models allowed us to analyse the properties of the nuclear stellar component, in Mrk 231. In addition, the presence of a young and blue stellar component – in the core of the nucleus of Mrk 231 – was already suggested, in the framework of extreme GW scenario with multiple expanding shells (for this merger and for similar BAL + IR + Fe II QSOs/mergers; Lípari et al. 1994, 2003, 2005).

5.1 Description of the GALFIT-3D model, and the application of this technique to Mrk 231

Different techniques have been developed to decouple the main components of an image. A commonly used method is to fit the image with 2D models, including template for each different components. This type of technique is implemented in GALFIT (Peng et al. 2002), a program for modelling several components in images. On the other hand, Jahnke (2002) developed a method for decoupling the host and nuclear spectra of galaxies, for 1D long-slit spectroscopy.

Integral field (or 3D) spectroscopy combines characteristics of images and spectroscopy techniques. Thus, a natural extension of the modelling 2D images (plus decoupling 1D spectra) is to split the 3D spectra data cube in a set of narrow-band images of the width of the spectral pixel and treat them as individual images. This technique has been used successfully for the deblending of QSOs/AGN with 3D spectroscopy (see for references Sanchez et al. 2006a,b).

A more detailed description of the GALFIT-3D method is presented in Appendix A. In addition, also a more detailed description of the effect of the DAR is included in Appendix B.

For the nuclear region of Mrk 231 ($r < 1.7$ arcsec), the 3D image modelling of the nucleus and the host galaxy for each monochromatic image was performed using GALFIT-3D. The 3D model comprises a narrow Gaussian function (to model the nucleus) and a de Vaucouleurs law (to model the galaxy), both convolved with a point spread function (PSF). Thus, a main step in this technique is to obtain the best PSF, for the 3D data (specially, for spectra obtained with high spatial and spectral resolution).

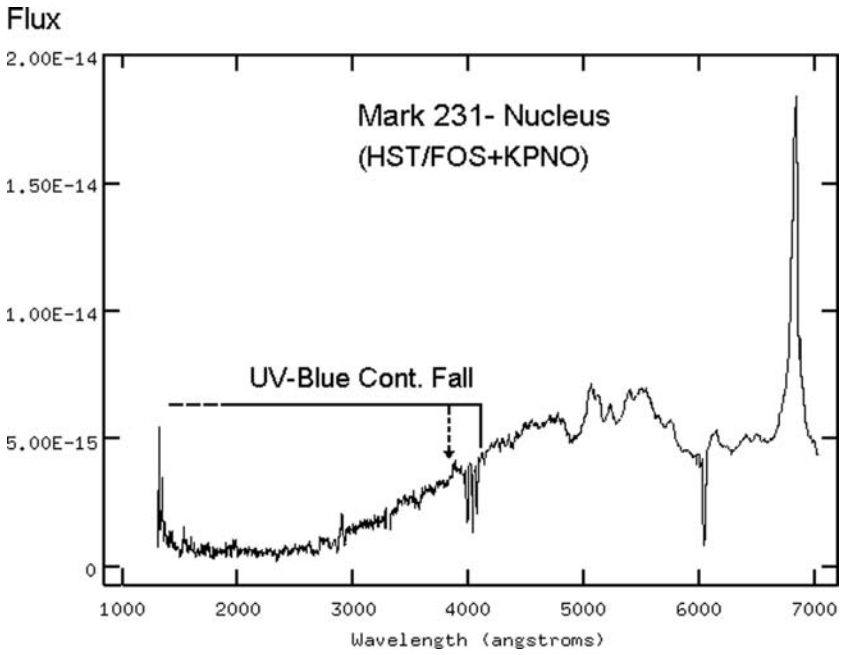

Figure 3. Combined 1D KPNO and *HST*/FOS spectra of Mrk 231. This figure is adapted from Lípari et al. (2005).

For the GMOS data, the PSF was carefully obtained from the core of the nucleus of Mrk 231 using the Hα and Hβ broad line emission. Thus, we have obtained a PSF, which was derived from the same 3D spectra that we study (similar to a PSF observed simultaneously with the scientific data: i.e. probably the best PSF available). In particular, the PSF was generated using the technique described in detail by Jahnke et al. (2004). For Mrk 231, the Hα and Hβ have a mix of broad line and continuum emission. By adding up the corresponding image slice and subtracting the appropriate background frame, the contained host and nuclear continuum emission were removed. This results in a pure BLR PSF.

Then, the fitting process was performed twice. A first iteration were all the morphological parameter of the host galaxy fitted freely, and second one were they are fix to the average values along the wavelength (as described in Sanchez et al. 2006a,b). This method ensures a clean decoupling of both spectra.

In addition, it is important to remark two main points about the process of modelling the 3D GMOS spectra of Mrk 231 nucleus.

(i) Only with the set of very deep Gemini GMOS–IFU observations (obtained with B600 grating, see Table 1), this method – for decoupling the 3D spectra – allowed a detailed study of the spectral feature of the host galaxy. Since the study of the faint host galaxy component requires 3D spectra with very high S/N.

Using the GMOS–IFU observations obtained with relatively short exposure time (i.e. those observed with R831 grating), we found that the pure spectrum of the host galaxy has very low S/N. Even for exposure of 900 s in a 8-m class telescope.

(ii) For the GMOS data obtained with B600 grating, we found that in almost all the observed spectral range the derived spectrum of the host galaxy shows high S/N values (larger than 10). Even at $\sim$3700 Å (close to the limit of blue wavelength range), the spectrum of the host galaxy shows good S/N (larger than 5). Obviously, this fact is due to the 'very' large exposure time of the B600 3D spectra (with more than 1 h of exposure time, for the nucleus).

On the other hand, it is important to remark that it is already known that the nuclear/QSO spectrum of Mrk 231 shows a strong continuum fall at wavelength shorter than 3800 Å (see Fig. 3, where the arrow depicts the strong continuum fall at this wavelength). Therefore, the blue limit for our 3D decoupling method was in the range $\lambda\lambda$3700–3800 Å.

5.2 Decoupling the BAL, host galaxy and QSO components in Mrk 231 (using the GALFIT-3D model)

Figs 4 and 5 show the spectra of the QSO and the host galaxy of Mrk 231 for the nuclear region ($r \sim 1.7$ arcsec), which were obtained using the technique of decoupling described in the previous subsection and from the 3D GMOS + B600 data. From this study and these plots, the following main results were found.

(i) *For the QSO component*: Figs 5(a), (b) and (c) clearly show – specially at Hα – that the broad emission lines are present, and thus the standard narrow line region (NLR) is absent. This is a very interesting property found in BAL IR QSOs (see for reference Lípari 1994; Turnsheck et al. 1997; Lípari & Terlevich 2006; Veron et al. 2006).

It is important to remark that in the blue wavelengths, the pure QSO spectrum shows a strong fall in the continuum. Furthermore, this strong fall in the blue continuum of the QSO is evident in Fig. 3: i.e. even before to perform any deblending technique. This feature –the drop in the blue continuum – is typical of low-ionization BAL QSOs and luminous IR QSOs/galaxies (Sprayberry & Foltz 1992; Lípari 1994; Turnsheck et al. 1997), which is associated mainly with strong nuclear reddening, by dust.

(ii) *For the host galaxy component*

(1) Fig. 5(c) depicts that the host galaxy has a strong nuclear blue/starburst component. Specifically, the flux of the host galaxy shows a very strong increase in the blue region of the optical spectrum. In addition, a similar result was found from the study of the emission and absorption lines in the individual GMOS spectra of the nuclear region (see the next sections).

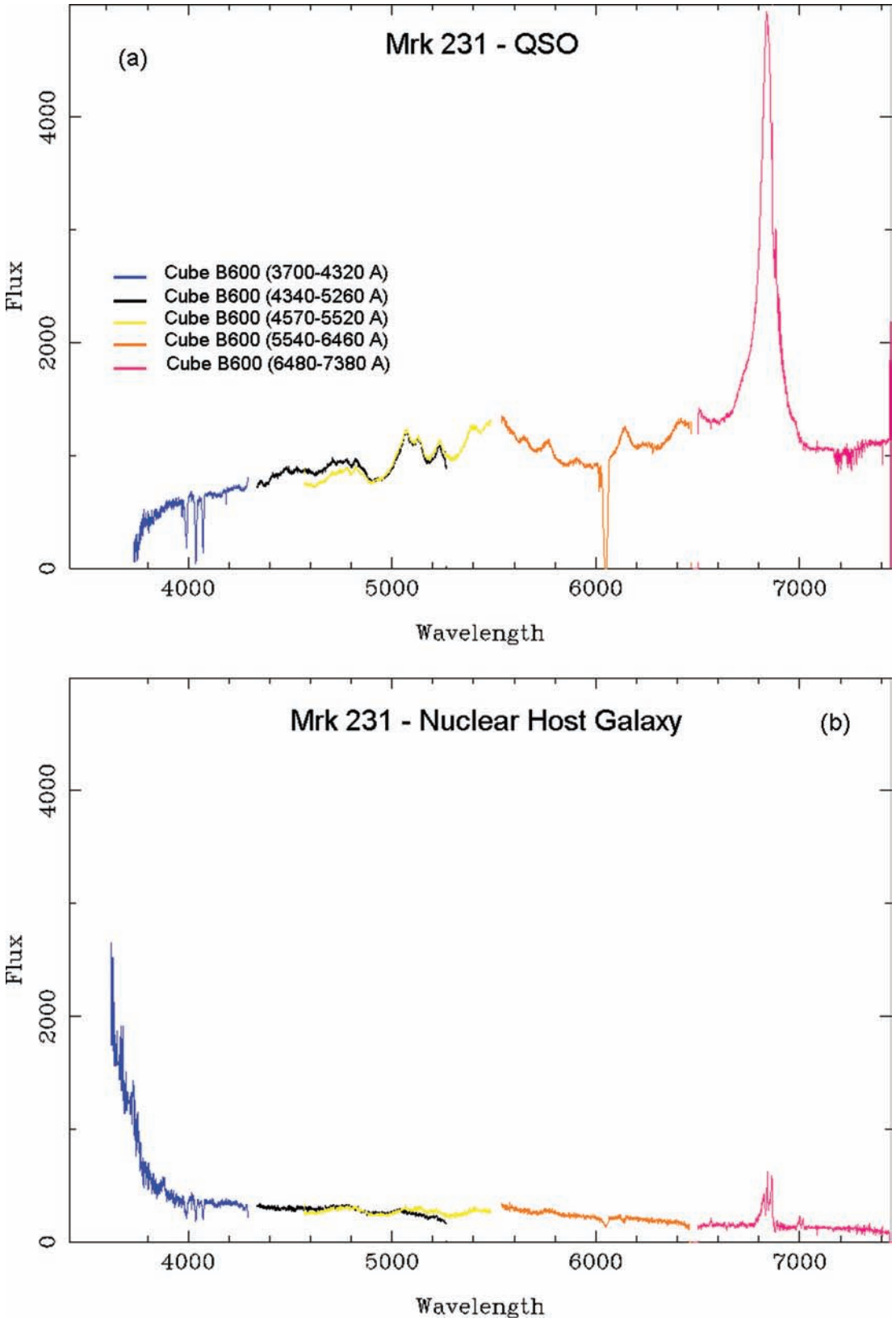

Figure 4. Decoupled QSO and host galaxy spectra of Mrk 231. These spectra were obtained from the decoupling of the Gemini GMOS–IFU B600 spectra, using the new technique described by Sanchez et al. (2004, 2006a,b) (see the text).

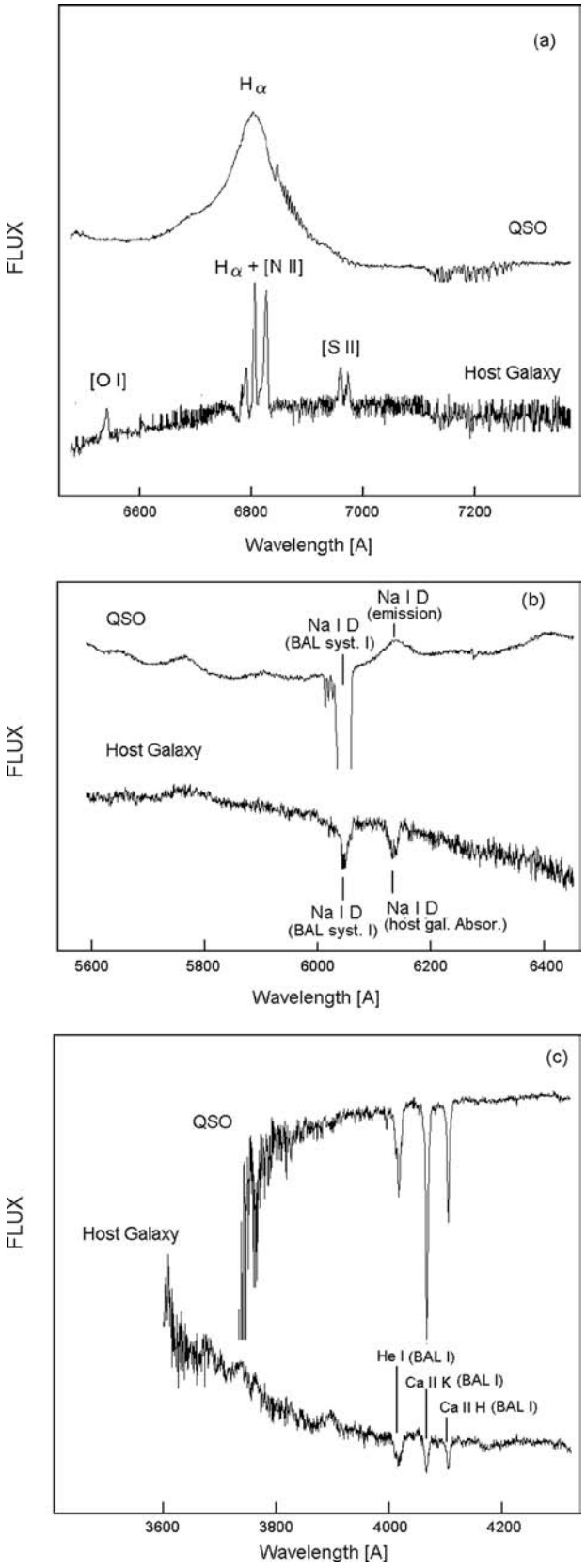

Figure 5. Detailed QSO and host galaxy nuclear spectra, of Mrk 231, for selected wavelength regions (using the B600 grating). In the panel 5(b) and for the host galaxy the *y*-axis was expanded (in order to show the weak narrow Na ID absorption lines).

(2) Figs 5(b) and (c) show that the BAL system I (at Na ID, He I and Ca II lines) are clearly observed in the host galaxy, i.e. the BAL I shows an extended morphology.

(3) Fig. 5(a) shows – at relatively low S/N – OF components in [N II]λλ6548 and 6583 emission lines, of the host galaxy.

(4) Figs 5(b) shows clearly the Na ID absorption in the host galaxy, at redshift of the system/merger.

An interesting explanation for point (i) is that the multiple nuclear explosive events (composite OF, detected previously in this QSO) probably expel the standard NLR. However, in the next sections we will present evidence of narrow emission-line systems – in the nuclear and circumnuclear regions – associated with the OF process.

6 MAPPING THE NUCLEAR CONTINUUM FLUX AND THE EXTREME BLUE COMPONENT WITH GMOS–IFU

In order to confirm one of the main results obtained in the previous section: i.e. the presence of an extreme blue component detected in the clean spectra of the host galaxy (for the nuclear region of Mrk 231), we have analysed – at different wavelength ranges – the shape of the continuum emission in each individual spectrum, for all the nuclear and circumnuclear regions.

Furthermore, it is important to remark that we already observed – using low spatial resolution 3D La Palma WHT + integral spectroscopy – some variations in the nuclear continuum shape (even in the red wavelength range, adjacent to Hα). Specifically, clear differences in the continuum shape were observed among figs 6(a), (b), (c) and (e) of Lípari et al. (2005), at different nuclear and circumnuclear areas.

Thus, a first basic qualitative study of GMOS spectra was performed, which was based in a direct/simple inspection of the continuum shape, at each spectrum. Figs 6 and 7 show two sequences of individual spectra (for the blue + [O II]λ3727 and visual + Hβ wavelength regions) along the north–south direction (PA = 00°). From this qualitative study of all the nuclear spectra, two very interesting results were found (which are evident in Figs 6 and 7): (i) in the southern nuclear area (from the core of the nucleus) an extreme blue continuum component was detected; (ii) in the northern area an extreme red continuum component was observed. These results were verified at almost all the observed wavelength ranges.

Then, a detailed quantitative study of the continuum was performed, using for this purpose a colour index defined – by us – as the difference of fluxes at the border of the wavelength range of each GMOS CCD (using the B600 grating; see Table 1 for details of the GMOS observation, and Allington-Smith et al. 2002 for details of the GMOS instrument):

(i) for the blue wavelengths: [Flux(λ4300) − Flux(λ3700)] × 10^{16},

(ii) for the visual wavelengths: [Flux(λ5250) − Flux(λ4350)] × 10^{16}.

Fig. 8 shows a map of the continuum colour index, for the wavelength region around Hβ (i.e. using the second colour index). This GMOS map confirms the presence of an extreme blue component in the continuum flux, which is located to the south of the nuclear region. This area is located in the region where we previously suggested that the GW – with superbubble/shells – is cleaning the nuclear dust. This fact is – probably – the reason that could explain,

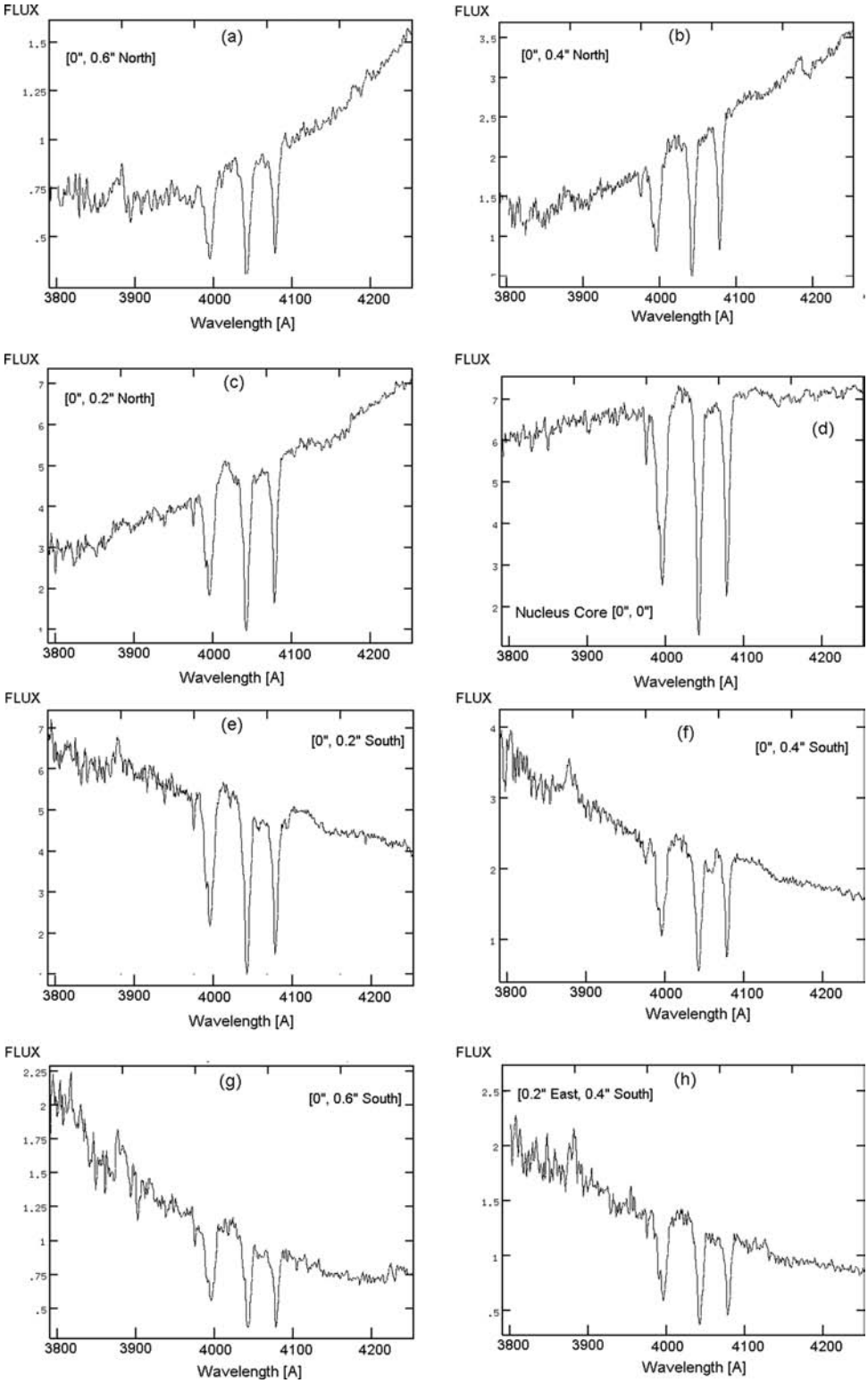

Figure 6. Sequence of individual GMOS spectra – at the blue wavelength region – of the core of the nucleus and the nuclear region of Mrk 231 – at PA = 00° – showing the presence of the strong blue (and red) continuum. The blue component was found in all the south region. The scales of flux are given in units of (erg cm^{-2} s^{-1} Å^{-1} × 10^{-16}).

that an extreme nuclear starburst is observed at optical wavelength (in an ultraluminous IR/dusty merger).

It is important to remark that: (i) for a radius $r < 1$ arcsec (from the nucleus) the errors in the values of the measured colour index [Flux(λ5250) − Flux(λ4350)] were less than 8–10 per cent. This fact is evident even if we see directly the different panels of Fig. 7: since the variations in the continuum are very strong and the spectra show very high S/N. (ii) We have measured the fluxes at λ4350

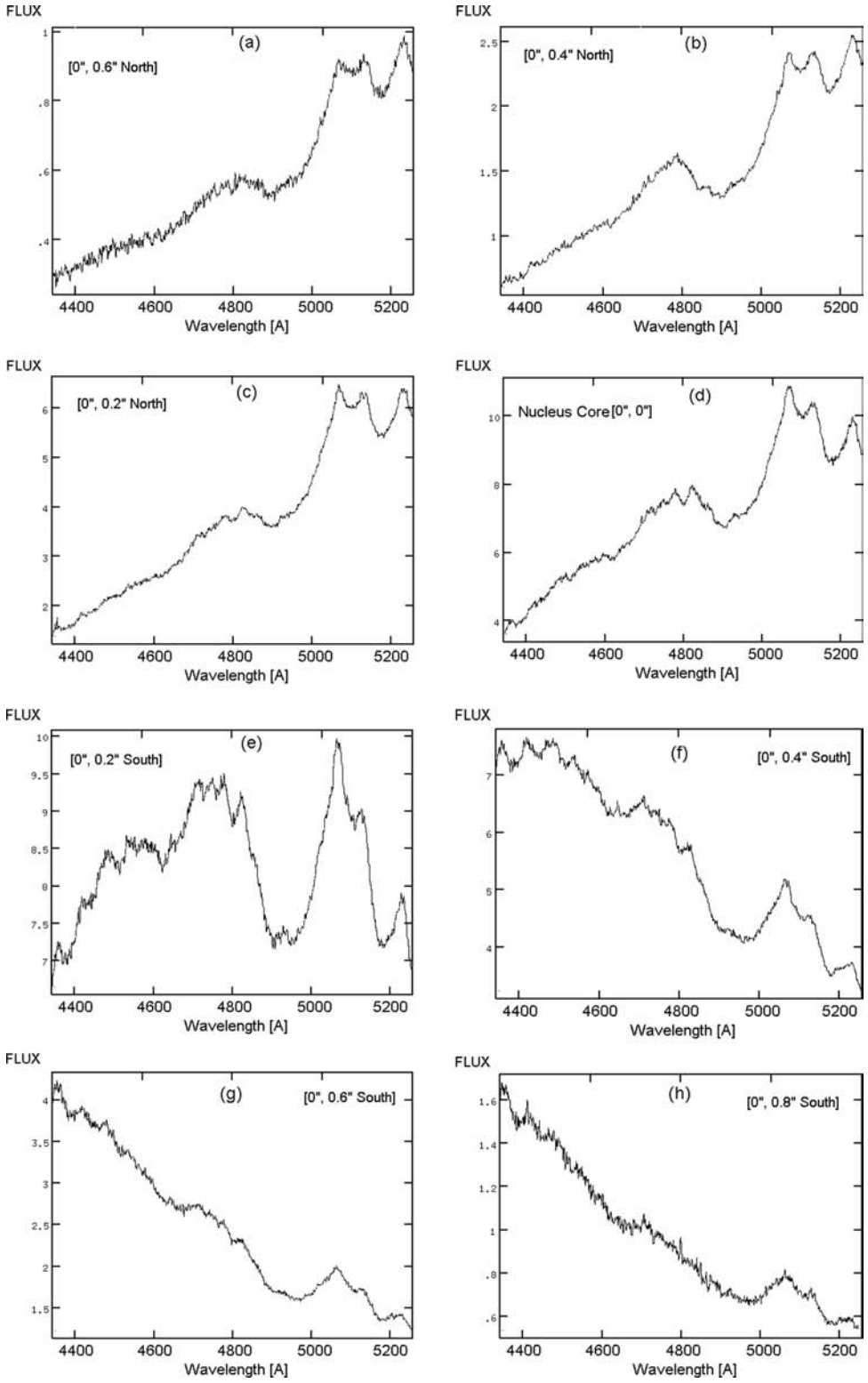

Figure 7. Sequence of individual GMOS spectra – at the Hβ wavelength region – of the core of the nucleus and the nuclear region of Mrk 231 – at PA = 00° – showing the presence of the strong blue (and red) continuum. The blue component was found in all the south region. The scales of flux are given in units of (erg cm^{-2} s^{-1} Å^{-1} $\times$ 10^{-16}).

and λ5250 Å using a wavelength window of Δ = 15 Å, which are almost free from emission lines.

The contour of this continuum colour index map (Fig. 8b) shows a clear peak in this blue continuum component, which is located at 0.3 arcsec to the south of the core of the nucleus. This position of the peak is located in the same position of the internal ring S5 (with also a radius of 0.3 arcsec; Lípari et al. 2005). Thus, this peak is probably positioned inside of the dusty ring or shell S5.

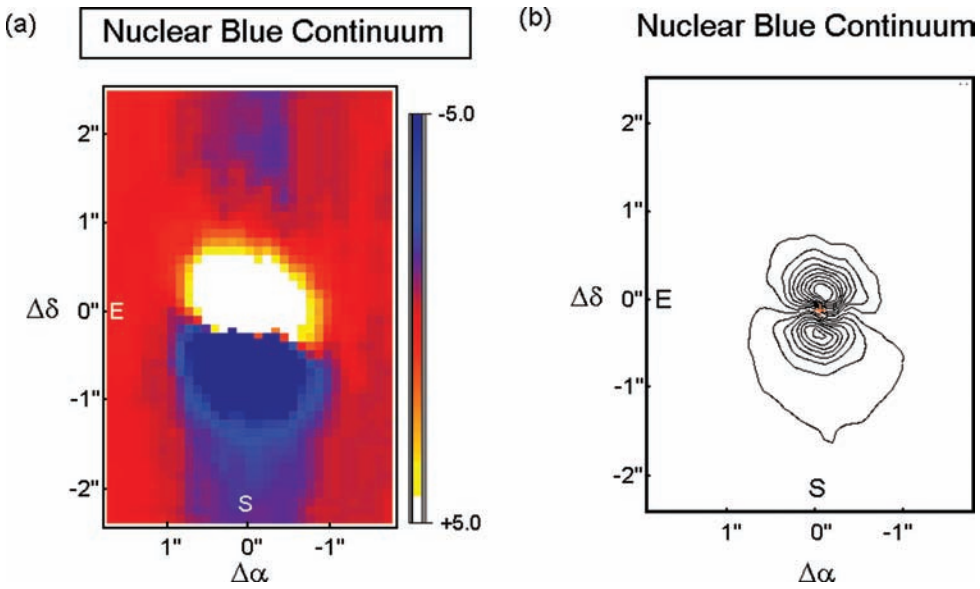

Figure 8. GMOS map and contour of the strong blue (and red) continuum components. The contours start from colour −6.0 to 4.3 (step of 0.6).

Furthermore, there is a symmetric red continuum peaks, positioned at 0.3 arcsec to the north of the core of the nucleus. The individual GMOS spectra of these two symmetric blue and red peaks show strong and narrow multiple emission-line components (with OF), specially in the lines.

(i) [O II]λ3727 (Fig. 6): The NLR in this line is absent at the core of the nucleus, but it is very strong and with double components at [0.4 arcsec south, 0.2 arcsec east], [0.4 arcsec south, 0.0 arcsec] from the core of the nucleus (which are in the area of the strong blue continuum peak). We have measured for these two [O II] component a $\Delta V = -400$ km s^{-1}, and full width at half-maximum (FWHM) of 160 km s^{-1}.

(ii) IR Ca IIλ8500 triplet: These lines show strong relatively narrow stellar emission and absorption 'only' at 0.4 arcsec to the north and south of the core of the nucleus (the areas of the red and blue continuum peaks). In the next section, this point (the emission and absorption of the IR Ca II triplet) will be analysed in detail.

(iii) [S II], [O I]λ6300, Hα, $H\beta$, [O III]λ5007: In Section 10, a detailed study of the NLR – at these lines – will be presented, for the core of the nucleus and the nuclear regions, we found that the nuclear NLR is associated to the nuclear OF process.

These results – specially the points (i) and (ii) – are the clear signature of a very young stellar population (close to the core of the nucleus). More specifically, the presence of two strong narrow [O II]λ3727 components (plus the ELRs found in this area) could be associated with young H II regions with strong OF process (Lípari et al. 2000, 2004a,d). The strong narrow emission plus absorption in the IR Ca IIλ8500 triplet is clearly associated with the peak of red supergiant (RSGs) activity, with age of 8 Myr < age < 15 Myr (see for references Lípari & Terlevich 2006).

On the other hand, different previous studies performed with very high spatial resolution at radio and millimetre wavelengths (using interferometric techniques) already proposed that in this area – of the ring S5 – there is a disc of molecular gas, with extreme star formation rate (SFR) of ∼100–200 $M_\odot$ yr^{-1} (Bryan & Scoville 1996; Carrilli, Wrobel & Ulvestad 1998; Downes & Solomon 1998; Taylor et al. 1999). Thus, our finding of a dusty ring or toroid with an extreme/young star formation process – around the nucleus of Mrk 231 – is in excellent agreement with previous studies performed at different wavelength regions and using different observational techniques.

7 MAPPING WITH GMOS–IFU THE NUCLEAR EMISSION OF THE NEAR-IR CA II TRIPLET

M231 is one of the few QSOs that show very strong near-IR broad Ca II triplet in emission (see for details and references Lípari & Terlevich 2006). Furthermore, our evolutionary and composite model for QSOs/AGN predicts the simultaneous occurrence of strong near-IR Ca II broad emission and strong Ca II stellar absorption, in young Fe II QSOs. Thus, the study of the high-resolution near-IR GMOS data (of Mrk 231) is: (i) an important test of our composite and evolutionary model of BAL + IR + Fe II QSOs; (ii) an important tool in order to study in detail the physical conditions in the nuclear and circumnuclear regions.

It is important to remark that the GMOS–IFU spectra of the near-IR Ca II triplet were obtained with the best spectral resolution of this instrument (∼40 km s^{-1}, using the GMOS grating R831). In addition, these data were obtained in our observing run with the best seeing/spatial resolution (see Table 1). Fig. 9 shows interesting GMOS data, at the near-IR Ca II triplet + O I, which were selected from the spectra of all the nuclear region. From this plot and study, we found very interesting results.

(i) In the core of the nucleus of Mrk 231, a blend of broad and strong emission – of the IR Ca II triplet – was detected (Fig. 9). Thus, at the core of the nucleus of Mrk 231, the NLR is probably absent. A similar result was found in Section 5, using GALFIT-3D method. Furthermore, similar results were detected for the BAL + IR + Fe II QSOs (i.e. the NLRs are absent at the cores).

(ii) At 0.4 arcsec north and 0.2 arcsec west, from the core of the nucleus of Mrk 231: strong narrow emission in the IR Ca II triplet + O I superposed with the broad blend – of Ca II emission – were detected (Fig. 9). The spectra of this region show the typical feature of a 'Seyfert 1.5' AGN.

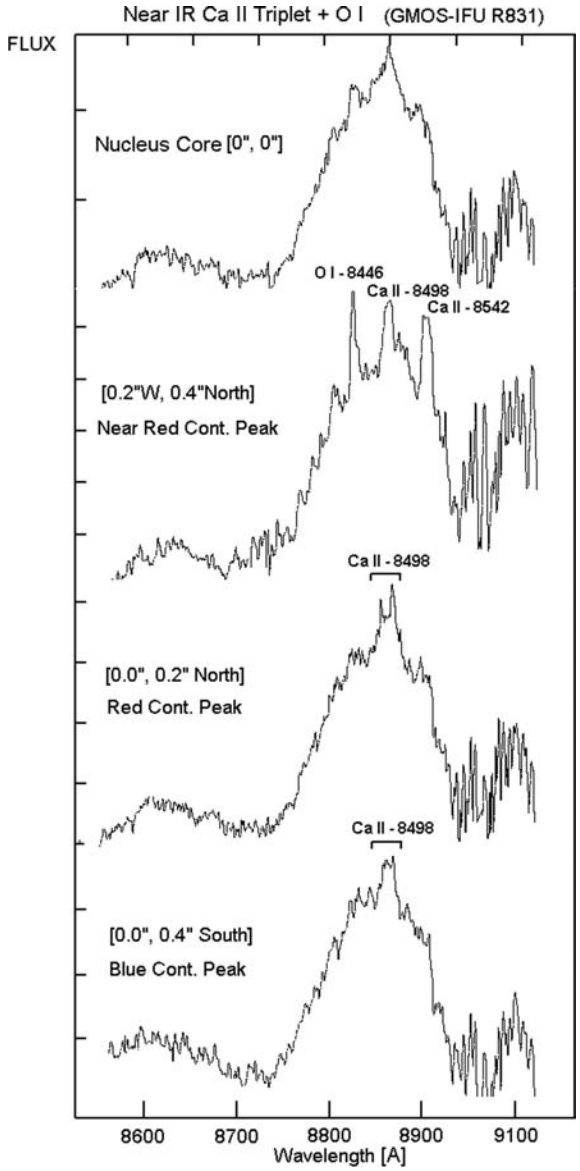

Figure 9. Selected GMOS spectra of the core of the nucleus and nuclear region of Mrk 231 – for the red wavelength – showing the IR Ca II triplet. These spectra were obtained with the best GMOS–IFU spectral resolution (and in our Gemini observing run with the best seeing/spatial resolution).

For the λ8446 O I and the IR λ8498, λ8542 Ca II lines, the following values of FWHM were measured: 190 and 370 km s^{-1}, respectively.

It is important to remark that in the GMOS R831 spectra (Fig. 9) the λ8662 Ca II line is positioned in the wavelength area of strong near-IR sky lines. Thus, this Ca IIλ8662 line (superposed with strong sky lines) was not used for this study.

(iii) At 0.2 arcsec north, from the core of the nucleus of Mrk 231: the narrow Ca II λ8498 line shows a clear emission with an 'unusual double peak' (see for typical IR Ca II triplet features, in AGN: Terlevich, Diaz & Terlevich 1991). This feature could be explained by the superposition of a strong narrow emission with a weak narrow absorption (Fig. 9).

It is important to remark that Lípari & Terlevich (2006) already suggested in their evolutionary unification composite model: i.e. the possible detection – in composite BAL + IR + Fe II QSOs/AGN – of the near-IR Ca II triplet, in emission and superposed with weak absorptions.

An explanation for this unusual double peak feature – observed at Ca II λ8498 line – is the interesting fact that the emission fluxes in the triplet is almost 1:1:1, but the absorption is 1:9:5. Thus, in this Ca II λ8498 line the emission and the absorption could be detected (together) more easily. Furthermore, for the same reason the line Ca II λ8542 is the more absorbed (Ca II line). This feature is also observed in Fig. 9 where the line λ8542 is almost absent.

It is important to remark that for the very near area, at 0.4 arcsec north and 0.2 arcsec west (from the core of the nucleus) the peaks of the Ca II λ8498 and λ8542 lines did not show any unusual double peaks/features.

(iv) At 0.4 arcsec south, from the core of the nucleus of Mrk 231, again the narrow Ca II λ8498 line shows a clear emission with an 'unusual double peak; and this feature could be explained by the superposition of a strong narrow emission with a weak narrow absorption (Fig. 9).

(v) A comparison of the flux and profile of the narrow near-IR Ca II λ8498 emission line, between the positions at [0.4 arcsec north, 0.2 arcsec west] from the core (which could be assumed as free of absorption) and at [0.2 arcsec north, 0.0 arcsec]: we found that the absorption in the Ca II λ8498 is close to 25–30 per cent of the emission line.

It is important to note that these results for the 'narrow' emission and absorption line of the near-IR Ca II triplet are free of any contamination from the core of the nuclear PSF. Since, the NLR is absent at the core of the nucleus of Mrk 231.

It is important to remark that these interesting areas at 0.2 arcsec to the north and 0.4 arcsec to the south of the core of the nucleus (i.e. the only regions where we detected the IR Ca II triplet with Seyfert 1.5 features plus the narrow Ca II λ8498 line with an 'unusual double peak feature; which is probably due to the emission plus absorption) could be associated with the previously detected ring S5 (Lípari et al. 2005). In this ring, the GMOS data also show the following.

(i) Two very strong peaks of blue and red continuum components (located at symmetric position, ∼0.3 arcsec from the core of the nucleus).

(ii) Very strong multi-emission-line components (with an OF of −400 km s^{-1}) in the [O II]λ3727 lines, and at the position of the blue continuum peak.

These finding are the typical evidence or signature of very young stellar population (or nuclear starburst), probably in a dusty starburst shell or ring/toroid. More specifically: the strong narrow *'emission plus absorption' in the IR Ca IIλ8500 triplet* is clearly associated with the peak of RSG activity, with age of, 8 Myr < age < 15–20 Myr, in metal-rich stellar populations (see for details Terlevich et al. 1991; Lípari & Terlevich 2006). This fact is an interesting prediction of the evolutionary and composite model for QSOs/AGN (Lípari & Terlevich 2006), which was confirmed using very deep high-resolution GMOS 3D spectroscopy.

On the other hand, the presence of a red peak of the continuum with narrow stellar emission plus absorption in the IR Ca II triplet lines (and thus associated with a very young stellar population) could be explained with the presence of large amount of dust in this type of very young starburst area, of the shell/ring (Lípari & Terlevich 2006).

8 MAPPING WITH GMOS–IFU THE BAL I AND II SYSTEMS

We have already started a study of the BAL systems, in Mrk 231, using 3D and 1D spectroscopy with moderate spatial and spectral resolution (∼1.0–1.5 arcsec and ∼100 km s^{-1}, respectively; Lípari et al. 2005). More specifically, we have studied: (i) the Hα blue emission bump, which is at the same OF velocity of the BAL I systems, and probably associated with this BAL I and (ii) the light-curve (LC) variability of the BAL III system, probably associated with SN or HyN.

In this paper, we have continued – using GMOS – our previous study of the BAL systems of Mrk 231, now using: the optical absorption lines, and improving the spectral and spatial resolution. Very deep Gemini GMOS–IFU/B600 data were obtained in the observing run of 2005 April 30, with the best spatial resolution of our observations (i.e. the best seeing of ∼0.4–0.5 arcsec, FWHM).

8.1 Study of individual 3D GMOS–IFU spectra

First the individual 3D Gemini GMOS spectra were studied, for the following reason: in the region of the line Na IDλ5889–95 we can see at the same time (without blending) the Na ID BAL systems and the broad emission line. The broad Na ID emission is originated in an almost point like BLR, and therefore it is one of the best trace – or the best upper limit – for the final instrumental seeing. Furthermore, the line Na IDλ5889–95 shows the strongest absorption of all the BAL observed in Mrk 231. Thus, using very deep 3D Gemini GMOS spectra, for the nearest BAL QSO, and for the strongest absorption line (Na ID BAL I): the high S/N of these 3D spectra allowed a detailed study of the extension of the BAL I system.

Fig. 10 shows a sequence of individual 3D Gemini GMOS–IFU spectra, along the north–south direction, from the core of the nucleus [at the position angle (PA) = 00°], with a step of 0.2 arcsec. This figure shows at that the broad emission of Na ID reach a radius r ∼0.8–1.0 arcsec ($r \sim$ 0.7–0.8 kpc), which is in agreement with the value derived for the GMOS-B600 seeing, of ∼0.4 arcsec FWHM. In addition, this plot clearly shows that the Na IDλ5889–95 BAL system I reach a radius $r \sim$ 1.4–1.6 arcsec ($r \sim$ 1.2–1.3 kpc). A similar behaviour was found, for the Na ID BAL system I, at several PAs including the PA in the direction of the jet (PA = −120°; Ulvestad, Wrobel & Carilli 1999a; Ulvestad et al. 1999b). Thus, these results suggest that the Na ID BAL system I is extended.

At the blue wavelength regions, we have verified that the BAL system I shows the same extended nature, in the absorption lines Ca II Hλ3969, Ca II Kλ3933 and He Iλ3889. In the next section a detailed study of the maps of some of these absorption lines will be presented.

On the other hand, all these results (about the extended nature of the BAl I system) are in excellent agreement with those obtained using GALFIT-3D method (see Section 5 and Figs 5b,c): the Na ID, Ca II Hλ3969, Ca II Kλ3933, and He Iλ3889 BAL I are clearly observed in the host galaxy; i.e. outside of the QSO/PSF spectrum.

Fig. 10 also shows the presence of narrow and weak Na ID absorption line at the redshift of the host galaxy (i.e. at the same wavelength position of the broad Na ID emission), at $r \sim$ 1.2–1.4 arcsec.

In order to confirm the possible extended nature of the Na ID BAL I system, it is important to analyse the contribution of the nuclear core-PSF at different offset. First, an interesting and general result is evident Figs 7 and 6: the different panels of these figures – with step of 0.2 arcsec – show only one main component, in each emission and absorption lines. This qualitative fact was quantitatively confirmed, by fitting these spectra, using the software SPECFIT. More specifically, we found that just one main component is required for the fit of each line in these spectra. These results are presented in Tables 12–15. Thus, this fact suggests that the contributions of the nuclear PSF, even at 0.2 and 0.4 arcsec are not too strong.

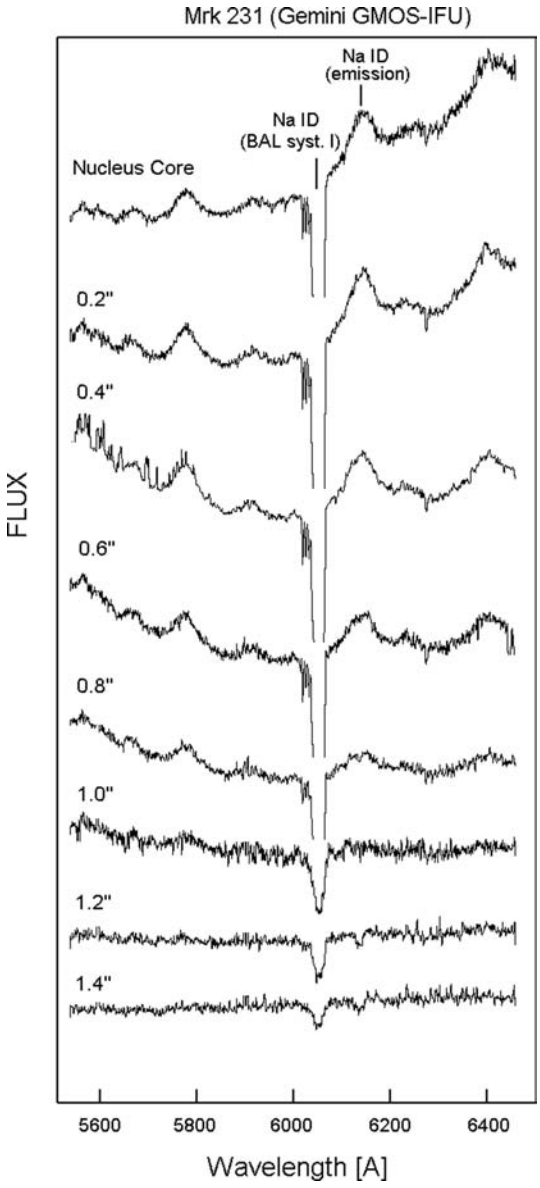

Figure 10. Sequence of 3D Gemini GMOS–IFU spectra, along the north–south direction (at PA = 00°) showing the extended nature of the Na IDλ5889–95 BAL system I. The scales of flux are given in units of (erg cm^{-2} s^{-1} Å^{-1}).

In addition, in Section 5 the PSF was carefully obtained from the core of the nucleus of Mrk 231 using the Hα and Hβ broad and strong emission lines. Using this PSF the contributions of the nuclear core-PSF at offset of 0.2, 0.4, 0.6 and 0.8 arcsec (from the core) were measured. We found that these contributions – at 0.2, 0.4, 0.6 and 0.8 arcsec – are 50, 10.4, 3.2 and 0.9 per cent (respectively), of the peak of the core. These values were derived using the PSF obtained for the GMOS–IFU B600 data (i.e. for the observation obtained with the best seeing of our Gemini GMOS data). Therefore, from these results it is important to remark two facts: (i) mainly the contribution of the PSF at offset of 0.2 arcsec is important; and thus at this offset we need to consider the contribution of the core-PSF

(if it is required); (ii) an empirical limit for the extension of the wing of the nuclear core-PSF is $r \sim 0.8$–1.0 arcsec. This limit is the same that we found from the study – in Fig. 10 – of the extension of the broad emission of the Na ID line.

All these Gemini GMOS–IFU results suggest that the BAL system I – in Mrk 231 – is extended, reaching a radius $r \sim 1.2$–1.3 kpc, which is in excellent agreement with previous studies of BAL QSOs, performed by de Kool et al. (2001, 2002), using Kech high-resolution spectroscopic data. They found that the BAL forming regions could reach radius of $r \sim 1.4$ kpc. See for details Section 13.2.1.

8.2 GMOS–IFU absorption maps for the BAL I and II systems

Figs 11(a), (b), (c), (d), (e) and (f) show the GMOS maps and contours for the absorption of the BAL I and II systems. These maps were constructed with the technique described in Section 3: i.e. we have measured for the BAL I and II systems the absorptions at each spectra, then with a table of absorption fluxes and the positions (of each spectra) these data were converted to FITS maps using the software IDA (see for details and references Section 3).

It is important to note that first we fit the absorption – in each spectra – using the main component. We have verified that this way is a simple and efficient way to detect small elongation. Since the study of absorption with multiple component, could include some problems (e.g. the selection of the number of components, etc.); which could be even more important than the very weak elongation (that we are searching).

In particular, these figures present the following interesting results.

(i) Figs 11(a) and (b) depict the map for the BAL I at the line Ca II Kλ3933. These two plots clearly show (specially the contour map) that the absorption of the BAL I system is elongate at the PA close to the radio jet direction (at PA $\sim -120^\circ$).

(ii) Figs 11(c) and (d) show the map for the BAL II at the line Na ID. Again, these two plots clearly depict that the absorption of the BAL II system is elongate at the PA close to the radio jet direction (at PA $\sim -120^\circ$).

(iii) Figs 11(e) and (f) depict the map for the BAL I at the line Na ID. In this case is evident that the fit (of the absorption lines) with only one component did not allow us to detect any elongation. The main reason for this fact is that the GMOS B600 and R831 spectra of this 'very strong' BAL I system (at Na ID), required for the fit more than one component. However, we already noted that the use of multiple components for the fit of this absorption present several problems, since the small elongation (that we are searching) could be masked by the errors in the technique of deblending.

A quantitative study of the elongation of the BAL I and II systems were performed using the software task ELLIPSES (from STSDAS, and developed by Dr Ivo Busko and kindly provided to us). This task allows us to fit ellipses to the BAL I and II absorption maps [original FITS files – obtained using the software task IDA – from which we derived Figs 11(a) and (c), respectively]. For the BAL I system, in the range of radius $0.35 < r < 0.8$ arcsec (from the nucleus), we found a very clear ellipticity, with a mean value of $b/a = (0.75 \pm 0.1)$ at PA $= -128^\circ$. Similar results were detected for the BAL II system, in the range of $0.4 < r < 0.70$ arcsec we found a mean value of ellipticity $b/a = (0.80 \pm 0.1)$ at PA $= -124^\circ$.

These results were also confirmed using a second method: fitting graphically ellipses to the contours (of the BAL I and II systems) in plots of high resolution. We found similar values to those obtained previously with the software ELLIPSES (for the BAL I and II).

Therefore, in general the results obtained in this section are in excellent agreement with the previous study of Hα emission (using 3D spectra with moderate spatial resolution; Lípari et al. 2005), where we found an OF emission bump, with a peak at the same velocity of the BAL system I (-4700 km s^{-1}). This Hα emission bump was detected in the nucleus and at 0.6–1.5 arcsec (from the nucleus) in the direction of the radio jet (at PA $= -120^\circ$ and 60°, see their table 4). Thus, these results are consistent with the fact that the blue Hα bump and the BAL I system could be associated with OF clouds of the small-scale jet. A detailed discussion of this point will be presented in Section 13.2.

8.3 Study of the BAL systems with GMOS high spectral resolution

Fig. 12(a) shows the BAL I and II systems in the strong line Na ID, for the best spectral resolution of GMOS–IFU: 40 km s^{-1} (using the grating R831). From this plot, we found interesting results.

(i) The BAL systems I and II do not show strong/clear variability in the last three decades, since all the spectra obtained with similar high resolution (e.g. Rudy, Foltz & Stocke 1985; Kollatschny, Dietrich & Hagen 1992; Forster, Rich & McCarthy 1995; Rupke, Veilleux & Sanders 2002) are very similar to that presented in Fig. 12(a).

(ii) The BAL I system shows clearly the presence of multi-absorption components. Previously, Forster et al. (1995) suggested that the fit of the strong Na ID absorption line require at least nine components, for the study of this BAL I system. Rupke et al. (2002, their fig. 11) plot a fit of the BAL system I – at the Na ID absorption line – using 12 components.

It is important to note that all these previous work fit with only one component the Na ID BAL II system. This point is important in order to confirm the result obtained in the Section 8.2, since we detected the weak elongation in the maps of the BAL systems, only when we fit the absorptions with only one component (i.e. when we avoid the problem of fitting the absorption line with a large number of components).

8.4 Deep GMOS–IFU observation of the Na ID BAL III systems: confirming the exponential variability/fall

The variability of the short-lived BAL III Na ID system was previously studied (by Lípari et al. 2005). We found that the BAL III LC is clearly asymmetric with a steep increase, a clear maximum and an exponential fall (similar to the shape of an SN LC). An important point – in this paper – is to confirm the exponential fall of this BAL III system, using very deep GMOS data. An important point, supporting the explosive scenario for Mrk 231, is the exponential fall in the BAL III LC.

The optical Na ID BAL systems of Mrk 231 was observed using three different GMOS grating configuration (see for details Table 1). Only with very deep GMOS spectra and using the grating B600 (with good transmission and spectral resolution, at the region of the Na ID BALs) we detected this very weak BAL III system: in 2005 April.

Fig. 12(b) depicts this weak Na ID BAL III system. In order to confirm the behaviour of the variability of this absorption system, we have measured the EqW ratio of BAL III/(BAL I + II). For this ratio a value of 0.007 was obtained, for 2005 April 30. This new

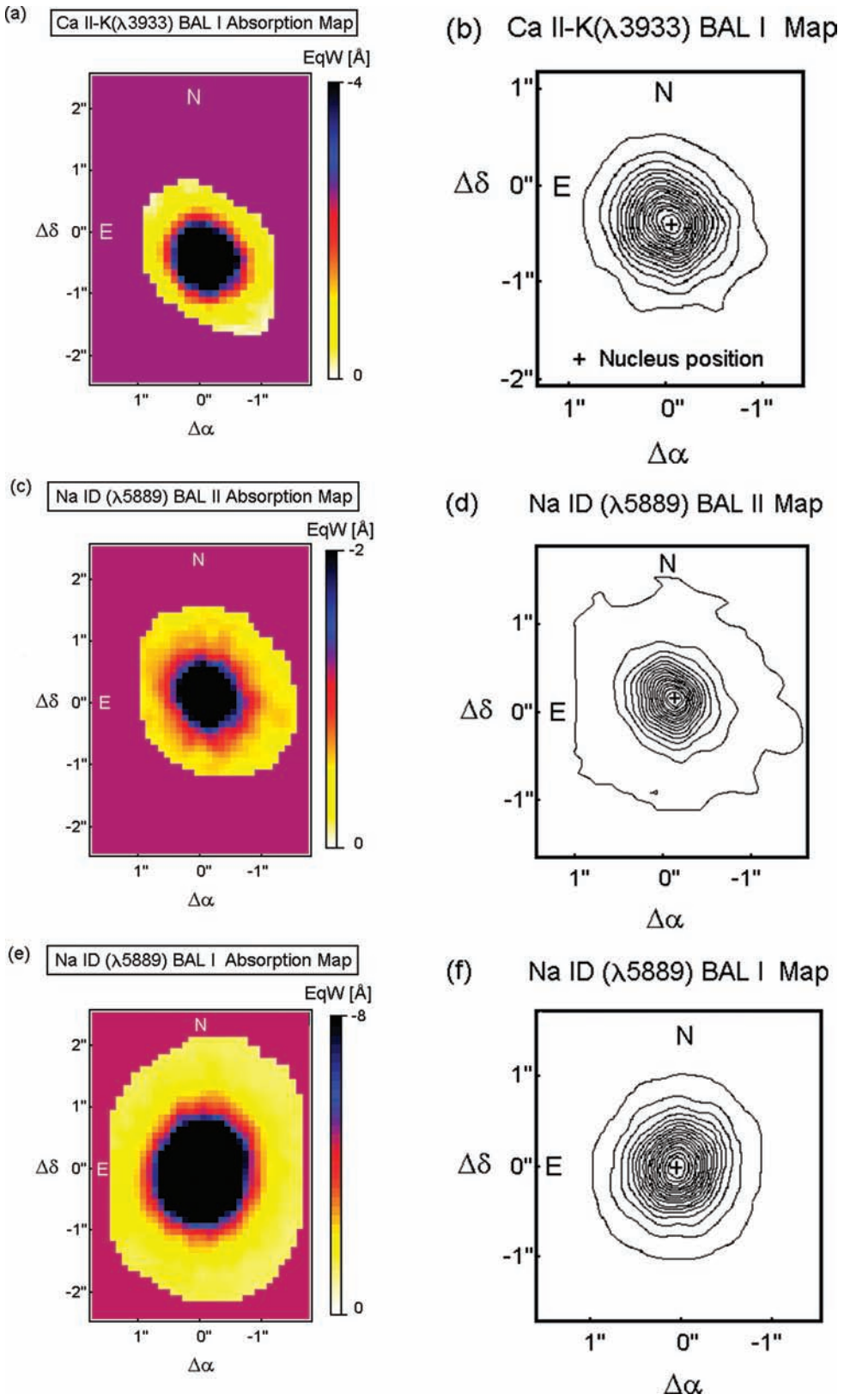

Figure 11. GMOS maps and contours of the absorption (EqW: Å) BALs systems. For the panels b, d and f, the contours – of absorptions – start from −1 to −8.5 (step 0.5), from −1 to −4 (step 0.2) and from −3 to 20 (step 1), respectively.

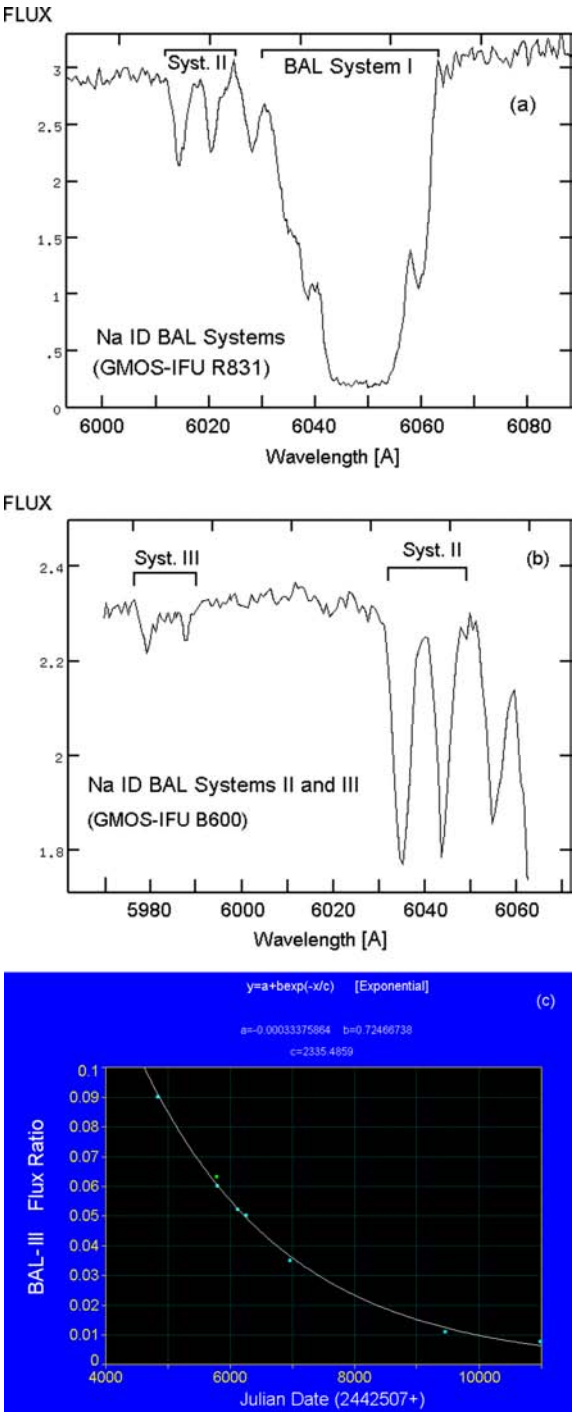

Figure 12. Na ID BAL I, II and III systems: (a) high-resolution (R831) spectrum of the BAL I and II systems; (b) medium resolution (B600) spectrum of the weak BAL III system; (c) LC variability of the Na ID BAL III system (for the fall, between 1988 and 2005). The errors (σ) in the BAL III Flux Ratios are in the range [0.001, 0.010] (see for details – of the errors – Kollatschny et al. (1992).

result was combined with those obtained previously by Lípari et al. (2005; their table 5) in Fig. 12(c). This plot shows the shape of the BAL III LC fall (including the new GMOS/2005 observation), plus the best fit. Again, we obtained the best fit of the LC fall, using an exponential function. In this figure the errors (σ, in the BAL III flux ratios) are in the range [0.001, 0.010]. For details – of the errors – see Kollatschny et al. (1992).

Thus, this study (using deep GMOS data) expand and confirm the previous study of variability of the Na ID BAL III system (covering almost all the period in which this system appeared). In general, the exponential shape of the BAL III system LC is similar to those LC of SN flux, emission line, etc.

9 GMOS–IFU DATA OF THE NUCLEAR EXPANDING SUPERGIANT SHELLS

Mrk 231 is probably the prototype of exploding QSOs. One of the main evidence of this explosive process is the presence of four nuclear expanding supergiant shells. In this paper, the main knots of these multiple nuclear shells were analysed – for this distant merger – using GMOS–IFU + *HST* data (of high spatial and spectral resolution).

It is important to study in detail these main knots detected in the multiple supergiant bubble with high-resolution 3D spectroscopic data, since they are the best and bright tracers of the expanding superbubbles.

In order to define the location of these main knots, in Fig. 13(a) we present high-resolution *HST* WFPC2 broad-band images of the nuclear region of Mrk 231; obtained in the optical wavelengths through the filter F439W ($\sim B$). This *HST* image shows the main concentric supergiant galactic shells. In order to depict in detail the structure – knots – of the shells, in Fig. 13(b) we show the result best example obtained from the subtraction of a smooth *HST* image of the main body of Mrk 231 (for the filter F439W $\sim B$).

The general properties of the three more external shells (S1, S2 and S3) were studied by Lípari et al. (2005). In this paper, we will study in detail the main knots of these shells (S1, S2 and S3) plus the nature of the inner shell S4 and the ring S5.

It is important to remark about the ring or shell S5 that this ring was observed in the *HST* optical ($I - B$) colour image, as a dusty ring (see Lípari et al. 2005: their fig. 4), which is located very close to the nucleus, with a radius $R_{S5} = 0.3$ arcsec $= 0.2$ kpc. In this paper (Sections 6, 7 and 13.1) we are presenting interesting results about this ring S5.

9.1 GMOS–IFU maps and cubes of nuclear region

Figs 14(a), (b), (c), (d), (e) and (f) show the red, green continuum and the Hα, Hβ, [O III]λ5007 and [S II]λ6717+31 emission-line images, obtained from the GMOS cubes. These figures show strong continuum (adjacent to Hα and Hβ, respectively) and emission line, associated with the nucleus and the more external superbubble/arc S1.

From these GMOS images, we remark the following new interesting feature.

(i) The Hα, Hβ and [S II]$\lambda\lambda$6717 + 31 emission images of the nucleus clearly show an asymmetry or elongation to the east and at $\sim$1 arcsec, from the core of the nucleus. The spectra in this region – call by us E1 – show H II region ELRs (see for detail Section 10). Furthermore, this region E1 is located very close to the position of the knot K3 (which is the main knot of the shell S3). This knot K3 also shows H II region ELR.

(ii) The external shell S1 shows a large and strong complex or association of several knots. This complex is located at 3.3 arcsec (3 kpc) to the south-west (of the nucleus) and the main members of this association are: the blue knots K11 and K12 and the red one K14 (see Figs 14 and 13).

(iii) The [O III]λ5007 emission-line image shows a strong emission, located very close to the knot K14 (at the north-west border

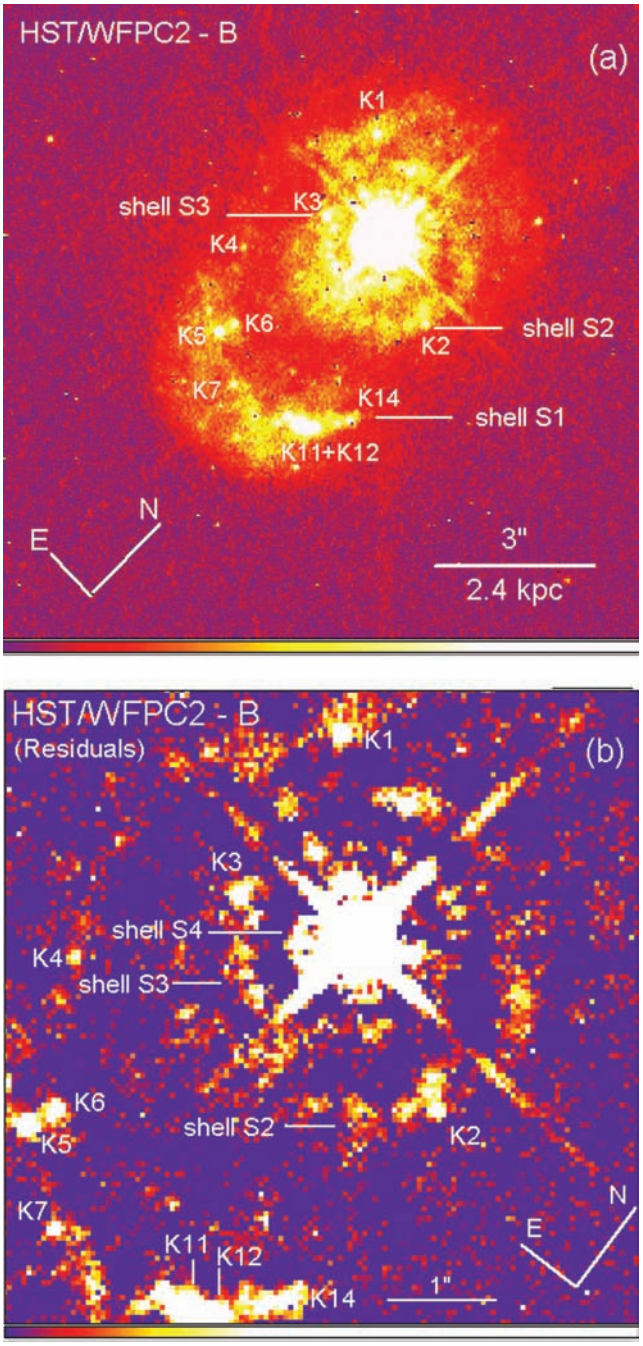

Figure 13. *HST*-WFPC2 F439W *B* image (a) and residuals image (b) of Mrk 231 are depicted, which shows the main shells and their knots (see the text). These images were adapted from Lípari et al. (2005).

of the strong complex of H II regions, in S1). Specifically, the position of the strong [O III] emission is –within the errors – almost coincident with the position of this knot K14. The study of the individual 3D spectra in this region shows that all the main knots (in this complex) have strong and multiple blue shifted components, in the [O III]λ5007 emission line.

Thus, this region will be associated with a strong source of OF, at the border of the superbubble S1. This OF process will be studied using the kinematics maps (combining the Gemini + GMOS and La Palma WHT + integral 3D spectroscopy data).

9.2 GMOS–IFU spectra of the knots in the expanding supergiant shells (of Mrk 231)

Table 2 and Fig. 13 present the location and properties of the strong knots, which are located in the more external supergiant shells S1, S2 and S3 (we used for these knots the same notation suggested by Surace et al. 1998). In addition, these knots are labelled in Figs 13(a) and (b). Surace et al. (1998) already studied in detail these knots using *HST* photometry, in the *B* and *I* bands. It is interesting to note that recently we started a detailed photometric study of all the *HST* broad-band images available: U, B, I and H (Lípari et al., in preparation). The main results of this last study is consistent with those obtained by Surace et al. (1998). In this section, we will study – for these and new knots – their GMOS spectra, and their relation with the OF process in the four shells.

Using the GMOS 3D spectra and maps (with a spatial resolution of ∼0.4–0.5 arcsec, for the observing run of 2005 April 30), we performed a detailed study of the morphological, kinematics and physical conditions of the main knots, of the multiple expanding bubbles. Fig. 15 depicts examples of the red 3D spectra of these main knots or H II regions/complex. Tables 3–11 show the values of the fluxes and FWHM of the emission lines and their ratios, for knots in the bubbles.

In order to study the GMOS spectra of the main knots of the supergiant expanding bubbles we used the following technique: (i) first the main knots of the four more external supergiant bubbles were selected, from the high spatial resolution *HST* WFPC2 and ACS images; (ii) then, using the *HST* position ($\Delta\alpha$ and $\Delta\delta$, offset from the core of the nucleus) of the main knots, we selected the nearest GMOS individual spectrum. Therefore, there are some differences between the offset obtained by Surace et al. (1998, using the peaks of the *HST* WFPC2 *B* and *I* images) and those presented in Tables 5–7. Our offsets were derived from the nearest GMOS spectra (of the corresponding knot peaks). On the other hand, we have verified also that the nearest spectrum – corresponding to each knot – shows the strongest value of continuum and line emission.

In addition, it is interesting to note that only in the very deep GMOS 3D data (with 1 h of exposure time, see Table 1) the spectra depict very high quality, with S/N > 5 in the weak OF components of the host galaxy. These deep GMOS spectra are required in order to study the weak knots of the more internal supergiant bubbles (S2, S3, S4 and S5). Only in the south-west circumnuclar areas, the OF components show strong values of flux in the emission lines.

It is also important to remark that in particular in the shell S2, S3 and S4 we have studied several new and interesting knots, which were included in the tables of fluxes, with the corresponding offset – right ascension (RA) and declination (Dec.) of the nearest GMOS spectra – from the core of the nucleus.

From this detailed study of the main knots of the four supergiant bubbles of Mrk 231 (see Tables 3–11), we remark the following main results.

(i) *General results*

The four external supergiant bubbles show – in ∼75 per cent of their extension – low-velocity OF velocities of $\Delta V \sim [-150, -250]$ km s^{-1}, with ELRs typical of shocks with low velocities (Heckman, Armus & Miley 1990; Dopita & Southerland 1995).

However, for the south-west region (in these four bubbles, with knots located at almost all the PAs) a clear blueshifted emission was detected, in the main and the OF components. With high value of OF, of ΔV = OF-EB2* = V(OF-EB2*) − V(MC-EMI*) ∼ −400 km s^{-1}.

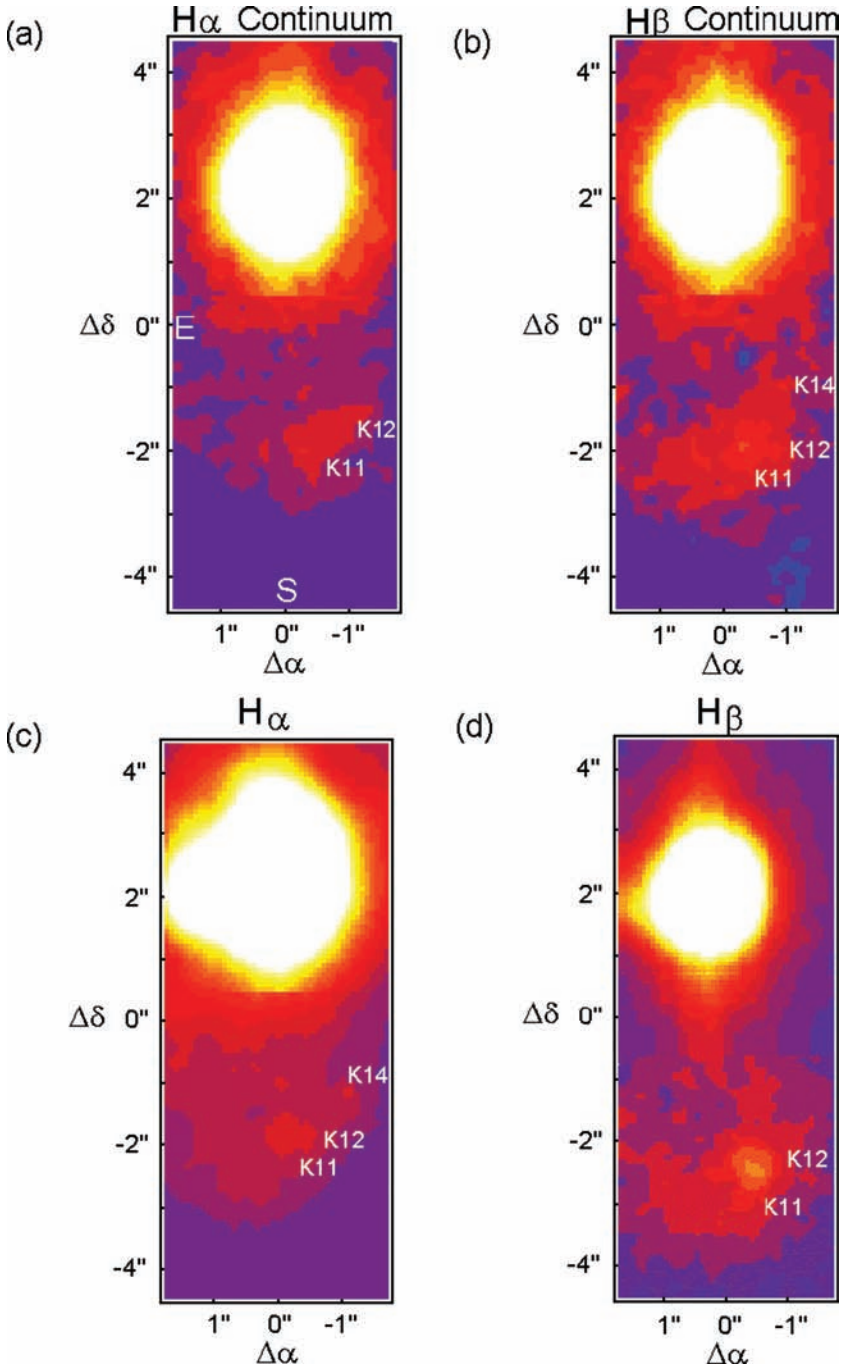

Figure 14. Gemini + GMOS mosaic maps (3.5×9 arcsec^2) of the continuum (a and b) and the narrow band of the redshifted Hα, Hβ, [O III]λ5007 and [S II]λ6716+31 (c, d, e and f) showing the main knots in the shell S1 (see the text). The nucleus (in each GMOS mosaic maps) is positioned at $\sim\Delta\alpha = 0$ arcsec, and $\sim\Delta\delta = +2$ arcsec. For the scales of fluxes of the main structures, see the scales of their GMOS spectra (Figs 6, 7, 15 and 16).

(ii) *Supergiant bubble/shell S1*

For the main knots of this bubble we remark the following results.

(1) Knot 14: Only in the knot K14-East and K14-West we detected a very strong OF emission-line component, which is similar in flux – or even stronger – that the main component (Table 4). Both components (the OF and MC systems) show LINER properties associated with shocks.

(2) In the three main knots of S1 (K14, K12 and K11) we found high values of OF velocities, with $\Delta V \sim -400$ km s^{-1}.

(3) At the strong knot K14, clear WR features were detected. Specially, in the east border of this knot K14 (K14-E, see Table 4).

(4) The other knots depict LINER properties. In addition, the knot K7 shows composite values of ELRs: between LINER and H II regions.

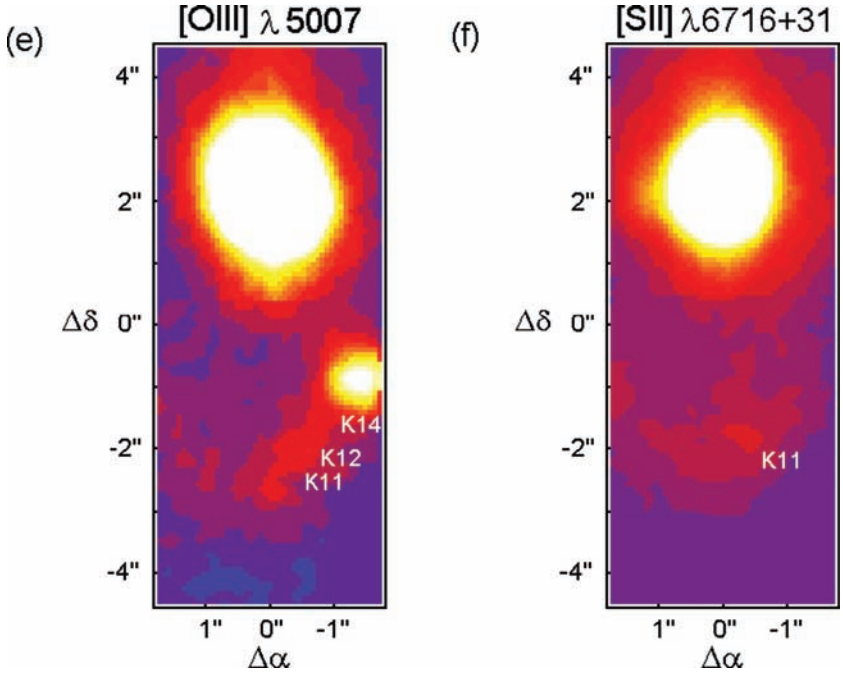

Figure 14 – *continued.*

Table 2. Main properties of the circumnuclear knots, associated with the supershells (in Mrk 231).

Knots[a]	$\Delta\alpha$[b] (arcsec)	$\Delta\delta$ (arcsec)	B_{F439W}[a] (mag)	I_{F814W}[a] (mag)	$B-I$	R_{eff}[a] (pc)	Shells
1	1.10	1.68	22.23	21.12	1.1	66	S1
2	−1.52	−0.90	23.27	20.86	2.4	<20	S2
3	1.10	−0.16	22.38	20.86	1.5	62	S3
4	2.12	−1.45	23.98	22.60	1.4	42	S1
5	1.70	−2.97	21.31	20.50	0.8	<20	S1
6	1.56	−2.74	22.97	22.28	0.7	71	S1
7	1.01	−3.70	22.69	21.47	1.2	38	S1
11	−0.46	−3.66	21.17	20.66	0.5	136	S1
12	−0.69	−3.61	21.46	20.70	0.8	31	S1
14	−1.20	−3.15	21.79	20.33	1.4	40	S1
29	−2.30	1.82	23.26	21.06	2.2	46	S1

[a]From Surace et al. (1998).[b] The offset positions of the knots [$\Delta\alpha$ (RA), $\Delta\delta$ (Dec.)] are given from the nucleus position (as 0,0). Surace et al. (1998) state that the colours are accurate to 0.2–03 mag; and the R_{eff} might be overestimate, but not by more than 40 per cent.

(iii) *Supergiant bubble/shell S2*

For the knots of this shell S2 the following main results were found.

(1) The main/strong knots (of this shell) are all located in the south-west region (knots S2a, S2b, S2c and S2d) with typical ELRs of LINER, associated with shocks of low velocity.

(2) The knots S2f and S2g show composite values of ELRs, which are between LINER and H II regions.

(iv) *Supergiant bubble/shell S3*

For the main knots of this shell S3 we found the following main results.

(1) The Knot S3a (also called K3, by Surace et al. 1998 and Table 2) shows values of ELRs clearly consistent with H II regions. This result is in good agreement with that obtained for the near area E1, which also shows H II region ELRs.

(2) The other knots (of this shell) show LINER properties, or composite values of LINERS and H II regions.

(v) *Supergiant bubble/shell S4*

For the main knots of the shell S4, very interesting results were found. In particular, we remark the following.

(1) This internal shell show in all the knot two similar emission line systems with strong [S II]λ6717/31 and [O I]λ6300. These are typical feature associated with shocks of low velocities in a dense medium [similar to those observed in the OF of supernova remnant (SNR) and Herving–Haro objects; Heckman et al. 1990; Shull & McKee 1979; Canto 1984; Binette, Dopita & Tuohy 1985].

(2) In addition, we have measured for these two emission-line systems an OF with $\Delta V \sim -200$ km s^{-1}, which is consistent with the presence of low-velocity shocks and the strong [S II] and [O I] emission.

In the next sections, the main physical and kinematics properties of the main knots/complexes of H II regions in the supergiant bubbles will be analysed (using individual 3D GMOS spectra and maps). Thus, interesting properties of these knots will be analysed in Sections 10 and 11. In particular, a detailed study of the ELRs of all these shells and knots will be presented in Section 10 (using emission-line maps and the main optical diagnostic diagrams of ionization).

9.3 Wolf–Rayet features in the main complex of knots in the external shell S1 (GMOS–IFU spectra)

An interesting result obtained from these GMOS spectra (Fig. 16 and Table 4) is the detection in the knot K14-East of clear WR features at λ4650 Å. These WR features suggest the presence of a high number of massive stars (probably in young superstar clusters), with ages $t < 6$–8×10^6 yr in this knot (which is associated with a

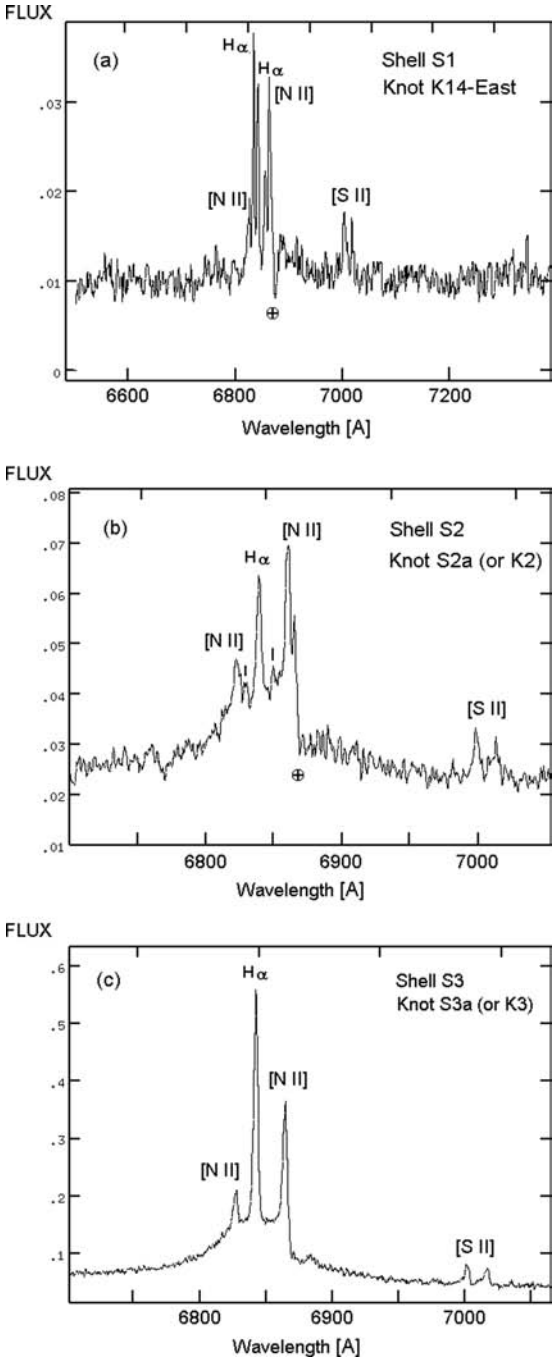

Figure 15. Examples of Gemini + GMOS 3D spectra in the main knots of the four external supergiant shells of Mrk 231 (showing several OF components). The scales of flux are given in units of (erg cm^{-2} s^{-1} Å^{-1} × 10^{-16}). The tick marks show the positions of the peaks of different emission-line components (in panel 15b the upper tick marks show OF components). See the text (Section 3.4) for details of the main components (MC) and OF; of the emission and/or absorption lines (EMI, ABS).

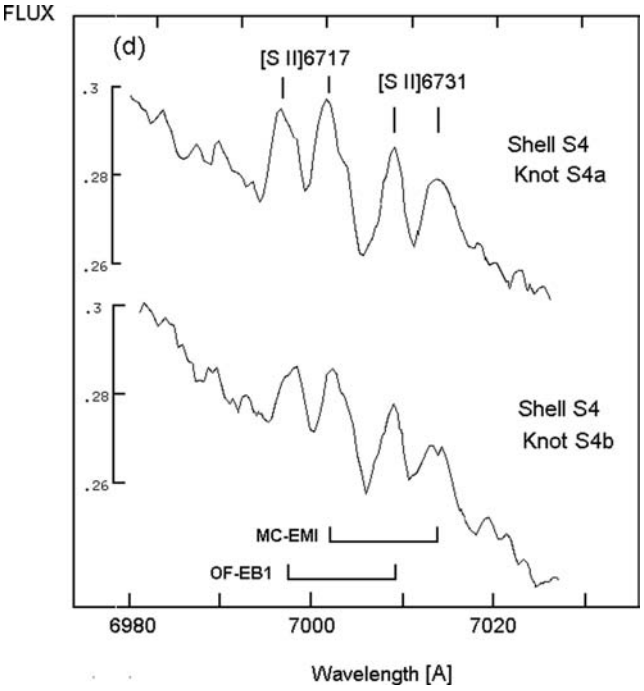

Figure 15 – *continued.*

complex of H II regions: K11 + K12 + K14). In the next subsection, we present evidence that this complex of H II regions is probably a point of rupture of the supergiant bubble S1.

It is interesting to remark that the [N I]λ5199 emission line was also found in this knot K14-East (where we detected the WR bump). A similar behaviour (i.e. strong WR and [N I] emission) was observed in the spectra of the prototype WR galaxy NGC 6754 (Osterbrock & Cohen 1982).

For a 'total' WRλ4650 flux of $F_{\rm WR} = 0.39 \times 10^{-16}$ erg cm^{-2} s^{-1} was measured; and the corresponding luminosity is $L_{\rm WR} = 1.31 \times 10^{38}$ erg s^{-1}. This last value is consistent with the presence of WR massive stars in similar young starburst knots (Lípari et al. 2003, 2004d).

Thus, for Mrk 231 we found a new example where WR stars are associated with a main complex of H II regions located at the border of a supergiant bubble (S1). A similar result was found for all the main points of rupture of the supergiant bubble of the nearby IR merger NGC 5514 (see Lípari et al. 2004d and the next subsection).

9.4 The OF in the strong complex of H II regions in the external shell S1

Hereafter, we call '*Aconcagua*' at this interesting complex of H II regions, located at the south-west border of the supergiant shell S1 and associated with the strong knots K11, K12 and K14. In our previous 3D kinematics study of Mrk 231 (based on La Palma WHT + integral spectroscopy for the central region 16.4 × 12.3 arcsec^2 ∼13 × 10 kpc) we found some evidence that this area could be associated to a main point of rupture of the supergiant shell/bubble S1. In particular, the Hα isovelocity colour map for the main component of the emission line (see Fig. 17, adapted from Lípari et al. 2005: their fig. 7) shows two opposite lobes – blue and redshifted – associated with this area, at the border of the shell S1.

In this paper, we found for this complex of H II region Aconcagua: (i) multiple OF components with high value of velocities (−400 km s^{-1}); (ii) a strong knot of [O III]λ5007 emission, which is very close to K14; (iii) the presence of high number of massive WR stars, in the knot K14-East.

It is important to remark, that previously we also detected the presence of several knots with massive WR stars in the supergiant bubble of NGC 5514 (and inside the areas of rupture of the

Table 3. Emission lines of the main knots of the shell S1 (located outside of the south-west region).

Lines	Component	Fluxes[a]				
		Knot 1 N-B043+R094	Knot 4 N-B022+R021	Knot 5 A-B043+R058	Knot 6 A-B044+R095	Knot 7 A-B140+R160
H$\beta\lambda$4861	MC-EMI	(0.10)	(0.08)	0.11	0.09	0.16
	OF-EB1	(0.01)	–	(0.01)	0.04	–
[O III]λ5007	MC-EMI	0.05	(0.10)	0.17	0.22	0.15
	OF-EB1	0.03	–	0.03	0.08	–
[O I]λ6300	MC-EMI	0.15	0.04	0.11	0.14	0.05
	OF-EB1	0.02	0.03	–	–	–
	OF-ER1	–	–	–	0.16	–
H$\alpha\lambda$6563	MC-EMI	0.85	0.22	0.39	0.35	0.54
	OF-EB1	0.06	0.05	0.04	0.11	0.06
	OF-ER1	0.03	0.04	0.05	0.09	0.02
[N II]λ6583	MC-EMI	0.97	0.23	0.48	0.48	0.38
	OF-EB1	0.09	0.15	0.05	0.12	0.08
	OF-ER1	0.05	0.06	0.04	0.12	0.03
[S II]λ6717	MC-EMI	0.30	0.14	0.20	0.15	0.15
	OF-EB1	0.02	0.10	0.08	0.06	0.04
[S II]λ6731	MC-EMI	0.28	0.11	0.15	0.10	0.13
	OF-EB1	0.03	0.09	0.05	0.06	0.04
Hα/Hβ	MC-EMI	(8.8)	(2.8)	3.5	3.9	3.4
	OF-EB1	(6.0)	–	4.0	2.8	–
FWHM Hα (km s^{-1})	MC-EMI	195	135	115	137	120
	OF-EB1	120	130	110	135	113

[a]The fluxes are given in units of 10^{-16} erg cm^{-2} s^{-1} (from GMOS/IFU-B600).
Line 2: N-Bmmm + Rnnn mean B600 spectrum at nucleus frame, blue mmm and red nnn number of the lenss.
Column 2: emission-line components, where MC-EMI, OF-EB1 and OF-ER1 are the
main component at $z = 0.042\,50$ ($cz = 12\,750$ km s^{-1});
OF blue component 1 at $z = [0.041\,40, 0.042\,10]$ ($cz = 12\,470, 12\,620$ km s^{-1}), $\Delta V = [-150$ to $300]$ km s^{-1};
OF blue component 3 at $z = 0.039\,20$ (11 749 km s^{-1}), $\Delta V = -905$ km s^{-1});
OF red component 1 at $z = [0.042\,98, 0.043\,33]$ (cz = 12 895, 12 998 km s^{-1}), $\Delta V = [+150, +250]$ km s^{-1}, respectively.
The values between parentheses are data with low S/N.
The errors/σ in the fluxes and FWHM are less than 10 per cent.

external shell). For NGC 5514 we already proposed that a population of very massive stars (like WRs) could be the source of multiple SN and HyN, and thus also the source of the rupture of the bubble.

In Sections 12 and 10 we will present more detailed evidence that Aconcagua (K14 + K12 + K11) is probably associated with the areas of ejection of the ionized gas and a main point of rupture of the more external supergiant bubble S1.

The properties of the four bubbles and their origin will be discussed in Section 13.3.

10 MAPPING WITH GMOS–IFU THE ELRs AND THE IONIZATION STRUCTURE

Using high spatial and spectral resolution GMOS–IFU data (which cover the main structures of the nuclear region and the supergiant bubbles) we have studied in detail the ionization and the physical conditions in the four supergiant shells; and also in the nuclear NLR. To study the NLR in Mrk 231 is important since the absence/weak standard NLR in Fe II + IR + BAL QSOs is well known (see for details Lípari et al. 1994; Turnsheck et al. 1997; Lípari & Terlevich 2006; Veron et al. 2006).

10.1 Mapping with GMOS the nuclear ionization structure

Figs 18(a) and (b) show the 3D maps (of $\sim$3.5 $\times$ 9.0 arcsec^2, $\sim$3 $\times$ 7.3 kpc, with a spatial sampling of 0.1 arcsec) of the ELRs [N II]λ6583/Hα, and [S II]λ6717 + 31/Hα. These maps were constructed using the techniques described in Section 3, for the main emission component.

Figs 18(a) and (b) show – with high spatial resolution – very interesting features. We note the following.

(i) The [S II]λ6717 + 31/Hα and [N II]λ6583/Hα maps show arcs and knots with high values: >0.8, at the border of the more extended superbubble or shell (S1). These arcs could be associated with shock processes at the border of the supergiant bubble S1.

(ii) The [N II]/Hα map shows two partial arcs (with several knots), to the north-west of the GMOS mosaic. These arcs depict white

Table 4. Emission lines of the strong knots of the shell S1 and the region SW1 (located at the south-west region).

Lines	Component	Fluxes[a]				
		Knot 11 A-B311+R342	Knot 12 A-B341+R392	Knot 14W A-B408+R445	Knot 14E A-B359+R407	Region SW1 A-B480+R482
WR bumpλ4650	MC-EMI*	–	–	(0.19)	0.32	–
H$\beta\lambda$4861	MC-EMI*	0.10	0.07	0.09	0.11	0.06
	OF-EB2*	–	–	0.05	0.06	–
	OF-EB3*	–	–	–	–	(0.07)
	OF-ER1*	–	0.11	–	0.07	–
[O III]λ5007	MC-EMI*	0.15	0.24	0.58	0.42	0.18
	OF-EB2*	0.08	0.06	0.08	0.07	–
	OF-EB3*	–	–	–	–	0.40
	OF-ER1*	0.10	0.10	–	0.08	–
[N I]λ5198	MC-EMI*	–	–	–	(0.11)	–
[O I]λ6300	MC-EMI*	0.06	0.02	0.03	0.05	0.03
	OF-EB2*	–	–	0.04	0.03	–
	OF-EB3*	–	–	–	–	0.03
	OF-ER1*	0.04	0.03	0.04	0.03	–
H$\alpha\lambda$6563	MC-EMI*	0.66	0.49	0.23	0.40	0.17
	OF-EB2*	0.09	0.12	0.37	0.35	–
	OF-EB3*	–	–	–	–	0.13
	OF-ER1*	0.01	0.03	0.07	0.08	–
[N II]λ6583	MC-EMI*	0.43	0.33	0.29	0.48	0.20
	OF-EB2*	0.17	0.12	0.25	0.28	–
	OF-EB3*	–	–	–	–	0.14
	OF-ER1*	0.12	0.10	0.06	0.05	–
[S II]λ6717	MC-EMI*	0.18	0.20	0.24	0.23	0.13
	OF-EB2*	0.03	–	(0.15)	0.06	–
	OF-EB3*	–	–	–	–	0.12
[S II]λ6731	MC-EMI*	0.15	0.18	0.18	0.14	0.11
	OF-EB2*	–	–	(0.15)	0.06	–
	OF-EB3*	–	–	–	–	0.11
Hα/Hβ	MC-EMI*	6.6	7.0	2.7	3.6	2.8
	OF-EB2*	–	–	7.4	5.8	–
	OF-EB3*	–	–	–	–	(2.0)
FWHM Hα (km s^{-1})	MC-EMI*	150	140	120	165	198
	OF-EB2*	115	149	125	115	–
	OF-EB3*	–	–	–	–	165

[a]The fluxes are given in units of 10^{-16} erg cm^{-2} s^{-1} (from GMOS/IFU-B600).
Line 2: N-Bmmm + Rnnn mean B600 spectrum at nucleus frame, blue mmm and red nnn number of the lenss.
Column 2: emission-line components, where MC-EMI*, OF-EB2*, OF-EB3*, OF-ER1* are the main component at SW region with $z = 0.042\,20$ (cz = 12 600 km s^{-1});
OF blue component 2 at $z = 0.040\,80$ (12 240 km s^{-1}), $\Delta V = -400$ km s^{-1});
OF blue component 3 at $z = 0.039\,20$ (11 749 km s^{-1}), $\Delta V = -905$ km s^{-1});
OF red component 1 at south-west region, at $z \sim 0.042\,80$ (cz = 12 840 km s^{-1}), $\Delta V \sim +200$ km s^{-1}.
The values between parentheses are data with low S/N.
The errors/σ in the fluxes and FWHM are less than 10 per cent.

colour, in Fig. 18(a), which are probably associated with shocks in the north-west part of the S2 and S3 supergiant bubbles.

(iii) The [S II] λ6717 + 31/Hα map depicts a structure with circular shape (like half of a bubble), with centre in the nucleus and at $r = \sim$1 arcsec. This structure is located to the east of the GMOS mosaic and depicts white colour, in Fig. 18(b), which is probably associated with shocks in the S3 superbubble.

(iv) For the circumnuclear area where we measured the narrow emission-line components: specially in the region of the supergiant shells, the [S II] λ6717 + 31/Hα and [N II]λ6583/Hα ELR maps show high values: >0.5.

10.2 GMOS ELR diagrams in the supergiant bubbles and the NLR

Using the individual spectrum of this GMOS data, an interesting study was performed of the ionizing source at supergiant bubbles, and the NLR.

Table 5. Emission lines of the main knots of the shells S2 (located to the south-west region, of the nucleus).

Lines	Component	Fluxes[a]						
		Knot S2a N-B419+R434 [1.4 arcsec west, 0.8 arcsec south]	Knot S2b N-B382+R418 [1.2 arcsec west, 0.9 arcsec south]	Knot S2c N-B331+R369 [0.9 arcsec west, 1.1 arcsec south]	Knot S2d N-B380+R320 [0.5 arcsec west, 1.3 arcsec south]	Knot S2e N-B122+R131 [0.7 arcsec east, 1.4 arcsec south]	Knot S2f N-B039+R090 [1.0 arcsec east, 0.4 arcsec north]	Knot S2g N-B159+R208 [0.2 arcsec east, 1.1 arcsec north]
H$\beta\lambda$4861	MC-EMI	–	–	–	–	0.07	0.21	0.41
	MC-EMI*	0.07	0.09	0.08	0.11	–	–	–
	OF-EB2*	0.04	–	–	–	–	–	–
[O III]λ5007	MC-EMI	–	–	–	–	0.20	0.20	0.40
	MC-EMI*	0.18	0.18	0.08	0.11	–	–	–
	OF-EB2*	0.14	–	–	–	–	–	–
[O I]λ6300	MC-EMI	–	–	–	–	0.05	0.11	0.11
	MC-EMI*	0.12	0.10	0.14	0.05	–	–	–
	OF-EB2*	0.03	0.05	0.02	0.02	–	–	–
H$\alpha\lambda$6563	MC-EMI	–	–	–	–	0.21	1.66	1.70
	MC-EMI*	0.30	0.36	0.45	0.40	–	–	–
	OF-EB1	–	–	–	–	–	–	0.10
	OF-EB2*	0.10	0.13	0.07	0.07	–	–	–
	OF-ER1*	0.02	0.02	0.11	0.04	–	–	–
[N II]λ6583	MC-EMI	–	–	–	–	0.41	1.22	1.27
	MC-EMI*	0.40	0.45	0.44	0.44	–	–	–
	OF-EB1	–	–	–	–	0.06	–	0.07
	OF-EB2*	0.10	0.15	0.06	0.11	–	–	–
	OF-ER1*	0.04	0.02	0.05	0.06	–	–	–
							–	–
[S II]λ6717	MC-EMI	–	–	–	–	0.18	0.40	0.70
	MC-EMI*	0.22	0.23	0.10	0.13	–	–	–
	OF-EB1	–	–	–	–	–	–	0.20
	OF-EB2*	0.02	0.04	0.04	0.06	–	–	–
	OF-ER1*	–	–	0.04	0.02	–	–	–
[S II]λ6731	MC-EMI	–	–	–	–	0.10	0.34	0.60
	MC-EMI*	0.16	0.24	0.17	0.12	–	–	–
	OF-EB1	–	–	–	–	–	–	0.16
	OF-EB2*	0.03	0.06	0.04	0.01	–	–	–
	OF-ER1*	–	–	0.06	0.01	–	–	–
Hα/Hβ	MC-EMI	–	–	–	–	3.0	7.9	4.2
	MC-EMI*	4.3	8.0	5.6	3.6	–	–	–
	OF-EB1	–	–	–	–	–	–	–
	OF-EB2*	2.5	–	–	–	–	–	–
FWHM	MC-EMI	–	–	–	–	130	135	185
Hα	MC-EMI*	120	150	215	220	–	–	–
	OF-EB1	–	–	–	–	–	–	–
	OF-EB2*	120	165	150	170	–	–	–

[a]The fluxes are given in units of 10^{-16} erg cm^{-2} s^{-1} (from GMOS/IFU-B600 spectroscopy).
Column 2: emission-line components, as in Table 4.
Line 4: the RA and Dec. offset (from the core of the nucleus, as 0,0) for each GMOS spectrum, in each knot.
The values between parentheses are data with low S/N.
The FWHM unit is km s^{-1}.
The errors/σ in the fluxes and FWHM are less than 10 per cent.

The log [S II]/Hα versus log [O I]/Hα emission-line diagram was used. Since, this diagram is an important tools for the study of OF process and shocks, in dense medium (see Shull & McKee 1979; Canto 1984; Binette et al. 1985; Heckman et al. 1990; Dopita 1995; Lípari et al. 2004a, 2004b,c, 2005).

Again, it is important to remark that only in the very deep GMOS 3D data (with 1 h of exposure time, see Table 1) the spectra show very high quality: S/N $>$ 5, in the weak narrow emission lines of the host galaxy, which is required in order to study the NLR and the OF process in the nuclear and circumnuclear regions (using individual GMOS spectra; which were obtained with lens of 0.2 arcsec).

Fig. 19(a) shows this log [S II]/Hα versus log [O I]/Hα diagram for the four more external supergiant bubbles. In Fig. 19(a), the

Table 6. Emission lines of the main knots of the shells S3 and region E1.

Lines	Component	Fluxes[a]						
		Knot S3a N-B085+R115 [0.9 arcsec east 0.3 arcsec south]	Knot S3b N-B118+R135 [0.7 arcsec east 0.6 arcsec south]	Knot S3c N-B169+R184 [0.4 arcsec east 0.8 arcsec south]	Knot S3d N-B318+R335 [0.7 arcsec west 0.6 arcsec south]	Knot S3e N-B317+R336 [0.7 arcsec west 0.4 arcsec south]	Knot S3f N-B113+R140 [0.7 arcsec east 0.4 arcsec north]	Region E1 N-B065+R088 [1.0 arcsec east 0.0 arcsec north]
H$\beta\lambda$4861	MC-EMI	0.51	0.20	0.09	–	–	0.20	0.73
	MC-EMI*	–	–	–	0.08	0.12	–	–
	OF-EB1	–	–	–	–	–	0.09	0.10
	OF-EB2*	–	–	–	0.06	–	–	–
[O III]λ5007	MC-EMI	0.25	0.10	0.10	–	–	0.10	0.39
	MC-EMI*	–	–	–	0.08	0.13	–	–
	OF-EB1	–	–	–	–	–	0.07	0.09
	OF-EB2*	–	–	–	0.07	–	–	–
[O I]λ6300	MC-EMI	0.07	0.08	0.16	–	–	0.18	0.13
	MC-EMI*	–	–	–	0.20	0.15	–	–
	OF-EB1	0.07	0.06	0.05	–	–	–	0.02
	OF-EB2*	–	–	–	0.19	0.26	–	–
H$\alpha\lambda$6563	MC-EMI	4.50	1.04	0.80	–	–	1.26	6.93
	MC-EMI*	–	–	–	0.55	0.83	–	–
	OF-EB1	–	0.35	0.30	–	–	–	–
	OF-EB2*	–	–	–	–	–	–	–
[N II]λ6583	MC-EMI	2.70	0.68	0.68	–	–	1.17	4.42
	MC-EMI*	–	–	–	0.20	0.31	–	–
	OF-EB1	–	0.11	0.10	–	–	–	–
	OF-EB2*	–	–	–	–	–	–	–
[S II]λ6717	MC-EMI	0.47	0.21	0.20	–	–	0.42	0.60
	MC-EMI*	–	–	–	0.24	0.22	–	–
	OF-EB1	–	0.06	0.07	–	–	–	–
	OF-EB2*	–	–	–	–	0.21	–	–
	OF-ER1	–	–	0.04	–	–	–	–
[S II]λ6731	MC-EMI	0.47	0.20	0.15	–	–	0.35	0.59
	MC-EMI*	–	–	–	0.20	0.18	–	–
	OF-EB1	–	0.03	0.04	–	–	–	–
	OF-EB2*	–	–	–	–	0.11	–	–
	OF-ER1	–	–	0.05	–	–	–	–
Hα/Hβ	MC-EMI	8.8	5.2	8.8	–	–	6.3	9.4
	MC-EMI*	–	–	–	6.9	6.8	–	–
	OF-EB1	–	–	–	–	–	–	–
	OF-EB2*	–	–	–	–	–	–	–
FWHM	MC-EMI	113	105	166	–	–	150	120
Hα	MC-EMI*	–	–	–	115	128	–	–
	OF-EB1	–	180	183	–	–	–	–
	OF-EB2*	–	–	–	–	–	–	–

[a]The fluxes are given in units of 10^{-16} erg cm^{-2} s^{-1} (from GMOS/IFU-B600 spectroscopy).
Column 2: emission-line components, as in Tables 3 and 4.
Line 4: the RA and Dec. offset (from the core of the nucleus, as 0,0) for each GMOS spectrum, in each knot.
The values between parentheses are data with low S/N.
The errors/σ in the fluxes and FWHM are less than 10 per cent.

values of ELRs (of the bubbles) were obtained from Tables 8–11. It is interesting to remark the following main points.

(i) Almost all the knots of the four external supergiant bubble are located in the area of SNR + HH (i.e. the shocks area), or in the transition/composite region between SNR + HH and H II regions. Thus in these knots and shells the OF process plays a main role.

(ii) Only the knot S3a (K3 in Table 2 and Surace et al. 1998) depicts ELRs typical of H II region.

(iii) In the more internal supergiant bubble S4, the ELR of all the knots show a position close to the upper right-hand part of this diagram (specially the knots located at the south-west area). This fact is consistent with the presence of strong [S II] and [O I] emission; and thus it is also consistent with shocks process of low velocities: of $\sim$200 km s^{-1} (see Shull & McKee 1979; Shull 1980; Binette et al. 1985; Heckman et al. 1990; Dopita & Southerland 1995).

It is important to study in detail also the narrow line emission in the core of the nucleus, and the nuclear/circumnuclear regions. Tables 12–17 show the fluxes and ELR for the core of the nucleus and for the nuclear area (for $r < 2.0$ arcsec) at

Table 7. Emission lines of the main knots of the shell S4.

Lines	Component	Fluxes[a]					
		Knot S4a B163+R190 [0.4 arcsec east, 0.4 arcsec north]	Knot S4b B188+R212 [0.2 arcsec east, 0.3 arcsec north]	Knot S4c B267+R286 [0.4 arcsec west, 0.4 arcsec south]	Knot S4d B288+R313 [0.5 arcsec west, 0.1 arcsec north]	Knot S4e B285+R315 [0.5 arcsec west, 0.3 arcsec south]	Knot S4f B167+R186 [0.4 arcsec east, 0.4 arcsec south]
H$\beta\lambda$4861	MC-EMI	0.16	0.30	0.08	0.11	–	0.13
	MC-EMI*	–	–	–	–	0.11	–
	OF-EB1	–	–	0.07	0.08	–	–
	OF-EB2*	–	–	–	–	0.09	–
[O III]λ5007	MC-EMI	0.09	0.17	0.19	0.15	–	0.20
	MC-EMI*	–	–	–	–	0.14	–
	OF-EB1	–	–	0.12	0.06	–	–
	OF-EB2*	–	–	–	–	0.11	–
[O I]λ6300	MC-EMI	0.33	0.43	0.29	0.20	–	0.23
	MC-EMI*	–	–	–	–	0.50	–
	OF-EB1	0.06	–	0.30	0.31	–	–
	OF-EB2*	–	–	–	–	0.55	–
H$\alpha\lambda$6563	MC-EMI	0.90	1.05	0.98	0.63	–	0.36
	MC-EMI*	–	–	–	–	0.48	–
	OF-EB1	–	–	–	–	–	–
	OF-EB2*	–	–	–	–	–	–
[N II]λ6583	MC-EMI	0.25	0.45	(0.40)	(–)	–	0.15
	MC-EMI*	–	–	–	–	(–)	–
	OF-EB1	–	–	–	–	–	–
	OF-EB2*	–	–	–	–	–	–
[S II]λ6717	MC-EMI	0.31	0.45	0.50	0.47	–	0.56
	MC-EMI*	–	–	–	–	0.33	–
	OF-EB1	0.22	0.37	0.40	0.48	–	0.42
	OF-EB2*	–	–	–	–	0.60	–
[S II]λ6731	MC-EMI	0.35	0.48	0.53	0.45	–	0.48
	MC-EMI*	–	–	–	–	0.45	–
	OF-EB1	0.20	0.29	0.45	0.40	–	0.40
	OF-EB2*	–	–	–	–	0.68	–
Hα/Hβ	MC-EMI	5.6	3.5	8.9	5.7	–	2.8
	MC-EMI*	–	–	–	–	4.4	–
FWHM Hα (km s^{-1})	MC-EMI	150	95	98	78	–	85
	MC-EMI*	–	–	–	–	80	–

[a]The fluxes are given in units of 10^{-16} erg cm^{-2} s^{-1} (from GMOS/IFU-B600 spectroscopy).
Column 2: emission-line components, as in Table 3 and 4.
Line 4: the RA and Dec. offset (from the core of the nucleus, as 0,0) for each GMOS spectrum, in each knot.
The values between parentheses are data with low S/N.
The errors/σ in the fluxes and FWHM are less than 10 per cent.

PA = 00°. At this PA – to the south – the OF process is collimate and very strong, at large and low galactic scales (see for details Lípari 1994; Lípari et al. 2005). Fig. 19(b) shows the log [S II]/Hα versus log [O I]/Hα diagram for the core of the nucleus and the nuclear region at PA = 00° (the values of these ELRs were obtained from Tables 16 and 17). From this plot and tables, it is interesting to remark the following points.

(i) In the regions close to the core of the nucleus (for $r <$ 0.7 arcsec $\sim$ 0.6 kpc), we detected similar properties to those observed in the more internal superbubble S4: i.e. two similar narrow emission-line systems, with strong [S II] and [O I] emission and $\Delta V \sim -200$ km s^{-1}. Furthermore, even at the core of the nucleus these two emission-line systems were detected.

(ii) In the log [S II]/Hα versus log [O I]/Hα diagram the ELR of the area close to the core of the nucleus ($r < 0.7$ arcsec) also shows a position close to the upper right-hand part of this diagram. Again, this fact is consistent with the presence of strong [S II] and [O I] emission; and thus it is consistent with shocks process of low velocities ($\sim$200 km s^{-1}; Heckman et al. 1990; Dopita & Southerland 1995). These results suggest that – in Mrk 231 – the NLR could be associated – mainly – with the OF process.

(iii) The ELR of the nuclear region (at PA = 00°, and for $r <$ 2.2 arcsec $\sim$ 1.8 kpc) are located in the log [S II]/Hα versus log [O I]/Hα diagram in the area of shocks: SNR + HH. However, in the south nuclear region (where we detected the blowout phase of the bubble) the ELR are located – again – in the upper right-hand

Table 8. ELRs of the main knots of the shell S1 and the region SW1.

Regions	Component	log[O III]/Hβ^a	log[O I]/Hα^a	log[N II]/Hα^a	log[S IIs]/Hα^a	Spectral type
Knot 1						
	MC-EMI	(−0.10)	−0.75	0.06	−0.17	LINER
	OF-EB1	(–)	−0.48	0.18	−0.08	LINER
Knot 4						
	MC-EMI	(0.00)	−0.74	0.02	0.06	LINER
	OF-EB1	–	−0.22	0.48	0.58	LINER
Knot 5						
	MC-EMI	0.19	-0.55	0.09	−0.05	LINER
	OF-EB1	(–)	–	0.10	0.51	LINER
Knot 6						
	MC-EMI	0.39	−0.40	0.14	−0.15	LINER
	OF-EB1	0.30	–	0.04	0.04	LINER
Knot 7						
	MC-EMI	−0.03	−1.03	−0.15	−0.28	LINER + H II
	OF-EB1	–	–	0.13	0.13	LINER
Knot 11						
	MC-EMI*	0.18	−1.04	−0.19	−0.30	LINER
	OF-EB2*	–	–	0.28	–	–
Knot 12						
	MC-EMI*	0.53	−1.39	−0.17	−0.11	LINER
	OF-EB2*	–	–	0.00	–	–
Knot 14W						
	MC-EMI*	0.76	−0.88	0.10	0.26	LINER
	OF-EB2*	0.20	−0.97	−0.17	(−0.09)	–
Knot 14E						
	MC-EMI*	0.58	−0.90	0.08	−0.03	LINER
	OF-EB2*	0.07	−1.12	−0.10	(−0.46)	–
Region SW1						
	MC-EMI*	0.48	−0.75	0.07	0.15	LINER
	OF-EB3*	0.56	−0.52	0.15	(0.36)	–

[a][O III]λ5007; [O I]λ6300; [N II]λ6583; [S IIs]λλ6716+6731.
Column 2: emission-line components, as in Table 3.
Column 7: spectral type, using the diagrams log [S II]/Hα versus log [O I]/Hα, log [O III]/Hβ versus log [S II]/Hα, log [O III]/Hβ versus log [O I]/Hα (from Heckman et al. 1990: Fig. 14; Lípari et al. 2004d). The values between parentheses are data with low S/N.
The errors/σ in the ELRs are less than 15 per cent.

border of this diagram, which is consistent with the presence of strong [S II] and [O I] emission and shock process.

11 MAPPING WITH GMOS–IFU THE NUCLEAR/CIRCUMNUCLEAR A-TYPE STELLAR POPULATION

Adams (1972), Adams & Weedman (1972), Boksenberg et al. (1977) and others detected the presence of an interesting stellar absorption-line system, in the nuclear and circumnuclear spectra of Mrk 231. This stellar system is observed with the GMOS data as strong absorptions in the blue Balmer H lines in Hδ, Hγ and Hβ.

From the study of the GMOS spectra of this A-type stellar population, new interesting results were found.

(i) For Hβ a range of EqW of 7–15 Å, and FWHM of 400–470 km s^{-1} were measured. These absorptions were detected at almost all the field covered by the GMOS mosaic (the nuclear area and the more extended bubble S1).

These values (of Hβ) were obtained using the wavelength windows suggested by Gonzalez Delgado, Leitherer & Heckman (1999), which allowed to compare our results with their synthetic spectra of H Balmer and He I absorption lines (for starbursts and post-starburst galaxies). The errors (σ) in the EqW of Hβ is less than 1.5 Å. For details of the method and errors, see Gonzalez Delgado et al. (1999).

In addition, for the H Balmer: Hβ, Hγ, Hδ, etc. the absorption spectra were analysed using – for comparison/fit – the observational templates of stellar populations and stellar clusters (provided by Piatti et al. 2002; Bica 1988), which are templates spectra obtained for with different ages of the post-starbursts and starbursts. Using the observational method, similar result was found, to that obtained with the theoretical method.

(ii) Using the lines Hβ and Hγ a redshift $z = 0.042\,55$ ($cz = 12\,765$ km s^{-1}) was measured, for this stellar absorption system, which is very close to that obtained for the main component of the emission line.

(iii) In addition, an interesting result was found when the position of the strong Hβ absorptions were plotted: they are located close to the external border of the two more external supergiant shells S1 and S2 (and thus with also 'arc shape').

Finally, a detailed study of the nuclear kinematics of this A-type stellar population (using the Hγ absorption line) was performed. In the next section the main results of this study will be presented. In addition, in Section 13.1, the properties of this stellar population will be discussed.

Table 9. ELRs of the main knots of the shell S2.

Regions	Component	log[O III]/Hβ^a	log[O I]/Hα^a	log[N II]/Hα^a	log[S IIS]/Hα^a	Spectral type
Knot S2a						
	MC-EMI*	0.41	−0.40	0.13	0.10	LINER
	OF-EB2*	0.37	−0.43	0.10	−0.20	LINER
Knot S2b						
	MC-EMI*	0.30	−0.56	0.10	0.02	LINER
	OF-EB2*	–	−0.41	0.06	−0.11	LINER
Knot S2c						
	MC-EMI*	0.43	−0.51	−0.01	−0.21	LINER
	OF-EB2*	–	−0.54	−0.06	0.06	LINER
Knot S2d						
	MC-EMI*	0.00	−0.90	0.04	−0.20	LINER
	OF-EB2*	–	−0.54	0.20	0.10	LINER
Knot S2e						
	MC-EMI	0.46	−0.62	0.29	0.12	LINER
	OF-EB1	–	–	–	–	–
Knot S2f						
	MC-EMI	−0.02	−1.18	−0.13	−0.35	LINER + H II
	OF-EB1	–	–	–	–	–
Knot S2g						
	MC-EMI	−0.01	−1.19	−0.12	−0.11	LINER + H II
	OF-EB1	–	–	−0.15	–	–

[a][O III]λ5007; [O I]λ6300; [N II]λ6583; [S IIS]λλ6716+6731.
Column 2: emission-line components, as in Table 3.
The values between parentheses are data with low S/N.
The errors/σ in the ELRs are less than 15 per cent.

Table 10. ELRs of the main knots of the shell S3 and the region E1.

Regions	Component	log[O III]/Hβ^a	log[O I]/Hα^a	log[N II]/Hα^a	log[S IIS]/Hα^a	Spectral type
Knot S3a						
	MC-EMI	−0.31	−1.80	−0.22	−0.68	H II
	OF-EB1	–	–	–	–	–
Knot S3b						
	MC-EMI	−0.34	−1.11	−0.19	−0.40	LINER + H II
	OF-EB1	−–	−0.77	−0.50	−0.59	LINER
Knot S3c						
	MC-EMI	0.18	−0.70	−0.07	−0.36	LINER
	OF-EB1	–	−0.78	−0.48	−0.44	LINER
Knot S3d						
	MC-EMI*	0.00	−0.44	−0.44	−0.10	LINER
	OF-EB2*	0.07	–	–	–	–
Knot S3e						
	MC-EMI*	0.03	−0.74	−0.43	−0.32	LINER
	OF-EB2*	–	–	–	–	–
Knot S3f						
	MC-EMI	−0.30	−0.85	−0.03	−0.21	LINER
	OF-EB1	–	–	–	–	–
Region E1						
	MC-EMI	−0.19	−1.73	−0.19	−0.77	H II
	OF-EB1	−0.05	–	–	–	–

[a][O III]λ5007; [O I]λ6300; [N II]λ6583; [S IIS]λλ6716+6731; [S II]/[S II] λ6716/λ6731.
Column 2: emission-line components, as in Table 3.
The values between parentheses are data with low S/N.
The errors/σ in the ELRs are less than 15 per cent.

12 MAPPING WITH GMOS–IFU THE NUCLEAR/CIRCUMNUCLEAR KINEMATICS

In this paper we preset – for the first time – a study of the kinematics of the stellar population of the nuclear region of Mrk 231 (plus the kinematics of the ionized gas). This study was performed in two main steps: first, the general properties of the absorption and emission lines. Using the corresponding VF maps and individual GMOS spectra. Then from the observed stellar VF a rotation curves (RCs) and the nuclear mass were derived (for a radius $r < 0.7$ kpc).

We already presented in previous sections the Hα VF for the central region of Mrk 231: 16.4 × 12.3 arcsec^2, with a spatial sampling

Table 11. ELRs of the main knots of the shell S4.

Regions	Component	log[O III]/Hβ^a	log[O I]/Hα^a	log[N II]/Hα^a	log[S IIS]/Hα^a	Spectral type
Knot S4a						
	MC-EMI	−0.25	−0.44	−0.56	−0.13	LINER
	OF-EB1	–	–	–	–	–
Knot S4b						
	MC-EMI	−0.25	−0.39	−0.38	−0.05	LINER
	OF-EB1	–	–	–	–	–
Knot S4c						
	MC-EMI	0.38	−0.53	(−0.39)	0.02	LINER
	OF-EB1	0.23	–	–	–	–
Knot S4d						
	MC-EMI	0.14	−0.50	–	0.17	LINER
	OF-EB1	−0.12	–	–	–	–
Knot S4e						
	MC-EMI*	0.11	0.02	–	0.21	LINER
	OF-EB2*	0.09	–	–	–	–
Knot S4f						
	MC-EMI*	0.19	−0.19	−0.38	0.46	LINER
	OF-EB2*	–	–	–	–	–

[a][O III]λ5007; [O I]λ6300; [N II]λ6583; [S IIS]λλ6716+6731; [S II]/[S II] λ6716/λ6731.
Column 2: emission-line components, as in Table 3.
The values between parentheses are data with low S/N.
The errors/σ in the ELRs are less than 15 per cent.

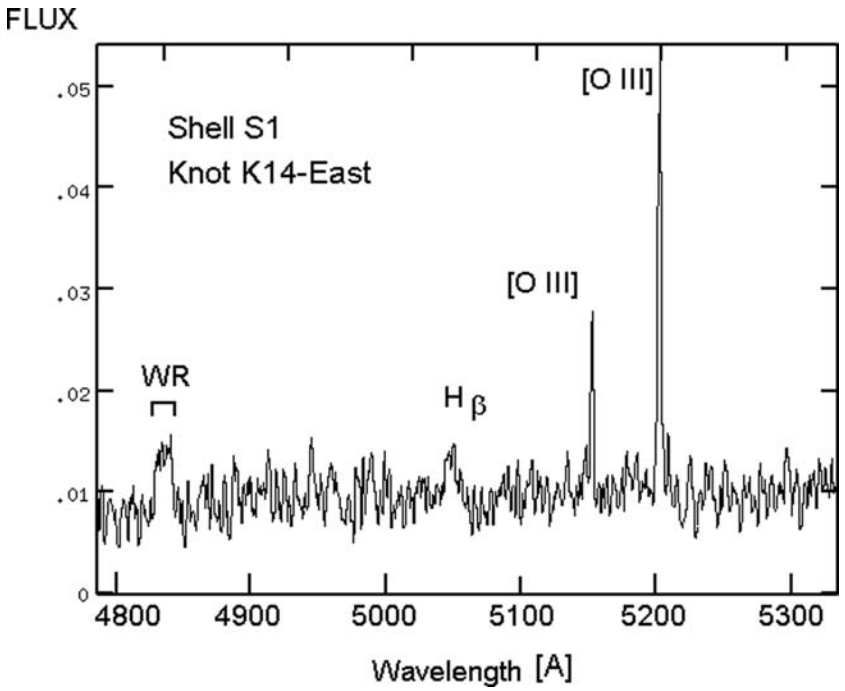

Figure 16. GMOS spectra showing WR feature, in the knot K14-East, at the more external shell S1 (see the text).

of 0.9 arcsec (Fig. 17; where also the area of the GMOS mosaic is depicted). This VF was obtained by Lípari et al. (2005), from La Palma WHT + integral. In this paper this La Palma Hα–VF of Mrk 231 will be compared with the GMOS kinematics data. Furthermore, this VF/figure is important for the study of the rupture of the shell S1 (at the H II region complex: Aconcagua) and for the extended OF process.

12.1 Mapping with GMOS–IFU the ionized gas kinematics ([O III]λ5007 and Hα)

Figs 20(a) and (b) show – for the ionized gas – the Hα and [O III]λ5007 VF maps for the nuclear and circumnuclear region of ∼3.5 × 9.0 arcsec^2 (∼3 × 7.3 kpc, with high spatial resolution or sampling of 0.1 arcsec). This map was constructed using

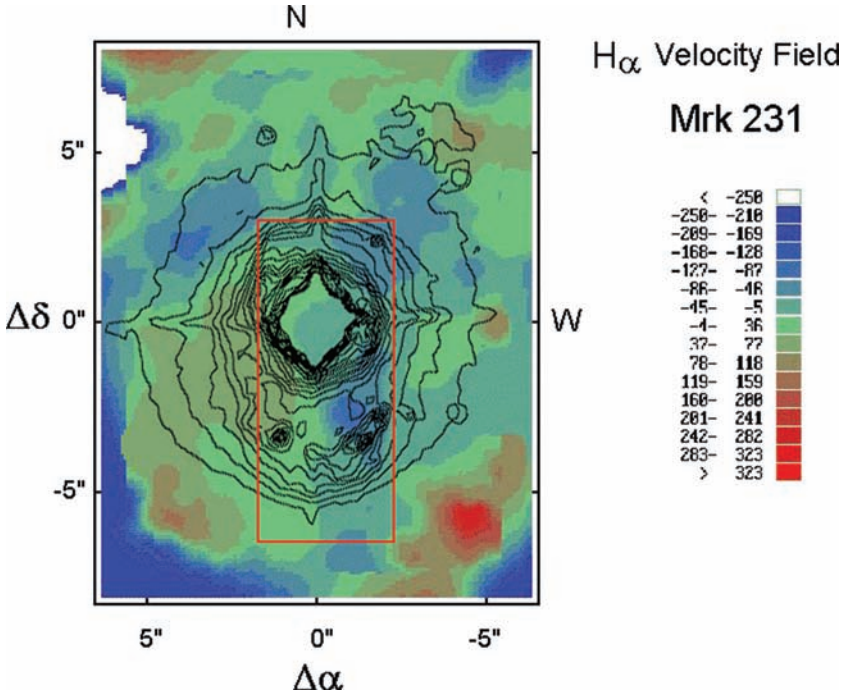

Figure 17. Superposition of the WHT + INTEGRAL Hα VF map for the ionized gas (of the central region of Mrk 231) and the *HST* WFPC2-I contour image. This figure is adapted from Lípari et al. (2005).

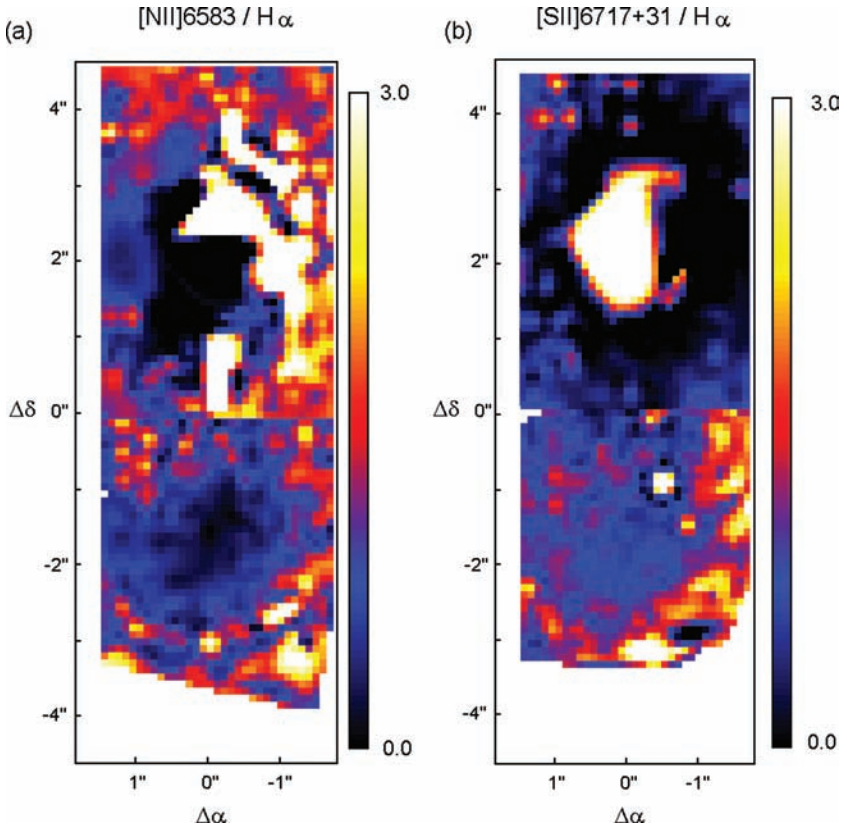

Figure 18. GMOS maps of the ELRs: [N II]/Hα and [S II]/Hα. The nucleus (in each GMOS mosaic maps) is positioned at $\sim\Delta\alpha = 0$ arcsec and $\sim\Delta\delta = +2$ arcsec.

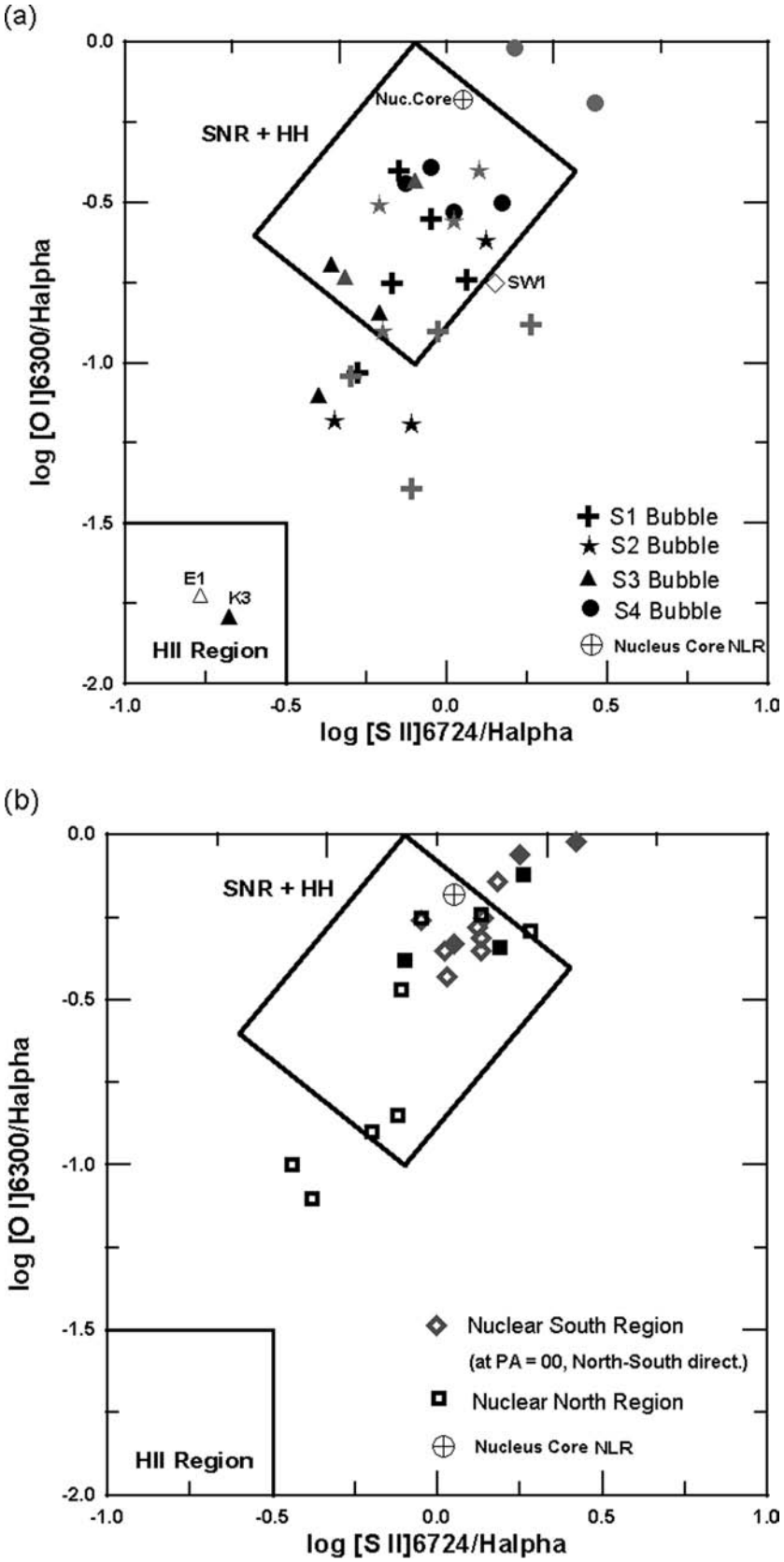

Figure 19. ELR diagnostic diagram (a) of the main knots of the four external supergiant bubbles (grey symbols are knots located in the south-west area); (b) for a sequence of the GMOS spectra, for the core of the nucleus and the nuclear region (with step of 0.2 arcsec and at the PA = 00). The filled symbols show the values for $r < 0.6$ arcsec. The main areas of these figures were adapted from Heckman et al. (1990; their fig. 14). The errors in the ELRs are less than 15 per cent.

Table 12. Emission lines of the core of the nucleus and south nuclear region (at north–south direction, PA = 180°).

Lines	Component	Fluxes[a]					
		Nucleus–Core N-B215+R238	0.2 arcsec south N-B216+R237	0.4 arcsec south N-B217+R236	0.6 arcsec south N-B218+R235	0.8 arcsec south N-B219+R234	1.0 arcsec south N-B220+R233
H$\beta\lambda$4861	MC-EMI	0.19	0.33	0.17	(0.28)	0.11	0.08
	OF-EB1	0.22	0.45	0.18	(0.19)	–	–
[O III]λ5007	MC-EMI	0.15	0.40	0.11	0.17	0.10	0.09
	OF-EB1	0.18	0.55	0.10	(–)	–	–
[O I]λ6300	MC-EMI	0.80	0.95	0.68	0.20	0.27	0.29
	OF-EB1	0.75	0.80	0.85	0.40	–	–
H$\alpha\lambda$6563	MC-EMI	1.20	0.85	0.40	(–)	0.85	0.53
	OF-EB1	1.80	0.84	0.48	0.85	–	–
[N II]λ6583	MC-EMI	(0.80)	(–)	(–)	–	0.36	0.33
	OF-EB1	1.47	(–)	(–)	0.37	–	–
[S II]λ6717	MC-EMI	1.05	0.60	0.50	0.58	0.50	0.25
	OF-EB1	1.14	0.66	0.45	0.46	(0.35)	–
[S II]λ6731	MC-EMI	1.25	0.80	0.52	0.48	0.40	0.18
	OF-EB1	0.92	0.50	0.42	0.55	0.55	–
Hα/Hβ	MC-EMI	6.3	3.0	3.1	–	7.7	6.6
FWHM Hα (km s^{-1})	MC-EMI	85	80	87	95	110	155

[a]The fluxes are given in units of 10^{-16} erg cm^{-2} s^{-1} (from GMOS/IFU-B600 spectroscopy).
Column 2: emission-line components, as in Table 3.
The values between parentheses are data with low S/N.
The errors/σ in the fluxes and FWHM are less than 10 per cent.

Table 13. Emission lines of the core of the nucleus and south nuclear region (at PA = 180°).

Lines	Component	Fluxes[a]					
		1.2 arcsec south N-B221+R232	1.4 arcsec south N-B222+R231	1.6 arcsec south N-B223+R230	1.8 arcsec south N-B224+R229	2.0 arcsec south N-B225+R228	2.2 arcsec south N-B226+R227
H$\beta\lambda$4861	MC-EMI	0.08	0.07	0.07	0.05	0.06	0.08
[O III]λ5007	MC-EMI	0.09	0.11	0.07	0.08	0.08	0.10
[O I]λ6300	MC-EMI	0.25	0.15	0.16	0.12	0.13	0.12
H$\alpha\lambda$6563	MC-EMI	0.44	0.38	0.33	0.27	0.18	0.25
[N II]λ6583	MC-EMI	0.36	0.45	0.40	0.32	0.25	0.30
[S II]λ6717	MC-EMI	0.30	0.20	0.22	0.19	0.13	0.15
[S II]λ6731	MC-EMI	0.29	0.19	0.22	0.17	0.14	0.16
Hα/Hβ	MC-EMI	5.5	5.4	4.7	5.4	3.0	3.1
FWHM Hα (km s^{-1})	MC-EMI	150	145	190	180	195	180

[a]The fluxes are given in units of 10^{-16} erg cm^{-2} s^{-1} (from GMOS/IFU-B600 spectroscopy).
Column 2: emission-line components, as in Table 3.
The values between parentheses are data with low S/N.
The errors/σ in the fluxes and FWHM are less than 10 per cent.

the techniques described in Section 3, and for the main component of the emission lines. The errors vary from approximately $\pm$10 km s^{-1} in the nuclear and central regions (where the emission lines are strong), to $\sim$20 km s^{-1} for the weakest lines away from the nuclear areas. For the study of the kinematic errors/σ, we are using – in general – the prescriptions suggested by Keel (1996).

The Hα and [O III]λ5007 isovelocity colour maps (Figs 20(a) and (b)) show some interesting new structures.

(i) The Hα VF in general shows redshifted velocity values in the east area of the merger, and blueshifted values to the west. However, very high blueshifted values were found in the south and south-west

Table 14. Emission lines of the north nuclear region (at north–south direction, PA = 00°).

Lines	Component	Fluxes[a]				
		0.2 arcsec north N-B214+R239	0.4 arcsec north N-B213+R240	0.6 arcsec north N-B212+R241	0.8 arcsec north N-B211+R242	1.0 arcsec north N-B210+R243
Hβλ4861	MC-EMI	0.15	0.12	0.13	0.08	0.13
[O III]λ5007	MC-EMI	0.13	0.11	0.08	0.05	0.11
[O I]λ6300	MC-EMI	0.78	0.66	0.48	0.28	0.23
Hαλ6563	MC-EMI	1.70	0.95	1.15	0.55	0.80
	OF-EB1	–	–	–	0.40	0.50
[N II]λ6583	MC-EMI	(–)	(–)	0.40	0.35	0.61
	OF-EB1	–	–	–	(–)	(–)
[S II]λ6717	MC-EMI	1.20	0.78	0.35	0.55	0.30
	OF-EB1	0.98	0.93	0.34	0.11	0.20
[S II]λ6731	MC-EMI	1.45	0.85	0.48	0.50	0.40
	OF-EB1	0.70	0.61	0.25	0.10	0.10
Hα/Hβ	MC-EMI	11.3	8.0	8.8	7.0	6.2
FWHM Hα (km s^{-1})	MC-EMI	85	95	120	115	125

[a]The fluxes are given in units of 10^{-16} erg cm^{-2} s^{-1} (from GMOS/IFU-B600 spectroscopy).
Column 2: emission-line components, as in Table 3.
The values between parentheses are data with low S/N.
The errors/σ in the fluxes and FWHM are less than 10 per cent.

Table 15. Emission lines of the north nuclear region (at PA = 00°).

Lines	Component	Fluxes[a]					
		1.2 arcsec north N-B209+R244	1.4 arcsec north N-B208+R245	1.6 arcsec north N-B207+R246	1.8 arcsec north N-B206+R247	2.0 arcsec north N-B205+R248	2.2 arcsec north N-B204+R249
Hβλ4861	MC-EMI	(0.15)	0.20	0.21	0.15	(–)	(–)
[O III]λ5007	MC-EMI	(0.10)	0.22	0.16	0.12	(–)	(–)
[O I]λ6300	MC-EMI	0.16	0.13	0.15	0.10	0.15	0.17
	OF-EB1	0.14	0.10	–	0.07	–	–
Hαλ6563	MC-EMI	1.68	1.64	1.18	0.70	0.44	0.31
	OF-EB1	–	–	0.18	–	–	–
[N II]λ6583	MC-EMI	0.95	1.23	1.19	0.61	0.45	0.40
[S II]λ6717	MC-EMI	0.26	0.33	0.44	0.33	0.18	0.20
	OF-EB1	0.15	0.22	0.10	0.08	–	–
[S II]λ6731	MC-EMI	0.35	0.35	0.30	0.24	0.16	0.25
	OF-EB1	0.10	0.10	0.07	0.10	–	–
Hα/Hβ	MC-EMI	(11.2)	8.2	5.6	4.7	–	–
FWHM Hα (km s^{-1})	MC-EMI	140	160	180	195	190	185

[a]The fluxes are given in units of 10^{-16} erg cm^{-2} s^{-1} (from GMOS/IFU-B600 spectroscopy).
Column 2: emission-line components, as in Table 3.
The values between parentheses are data with low S/N.
The errors/σ in the fluxes and FWHM are less than 10 per cent.

regions, which is good agreement with the fact that these two regions (south and south-west) are both areas associated with the rupture of supergiant bubble S1 (i.e. associated with a very strong OF process).

(ii) The [O III]λ5007 and Hα VFs show – in general – similar shape, but in the region of the nucleus ($\sim\Delta\alpha = 0$, and $\sim\Delta\delta = +2$ arcsec) the [O III] VF depicts very interesting substructure. In particular, filaments structures were detected, in the north and

Table 16. ELRs of the core of the nucleus and south nuclear regions (at north–south direction, PA = 180°).

Regions	Component	log[O III]/Hβ^a	log[O I]/Hα^a	log[N II]/Hα^a	log[S IIs]/Hα^a
Nucleus–Core					
	MC-EMI	−0.09	−0.18	(−0.18)	0.05
0.2 arcsec south					
	MC-EMI	0.07	0.01	–	0.25
0.4 arcsec south					
	MC-EMI	−0.18	0.25	–	0.42
0.6 arcsec south					
	MC-EMI	−0.18	−0.33	–	0.05
0.8 arcsec south					
	MC-EMI	−0.04	−0.43	−0.37	0.03
1.0 arcsec south					
	MC-EMI	0.55	−0.26	−0.20	−0.05
1.2 arcsec south					
	MC-EMI	0.05	−0.25	−0.09	0.14
1.4 arcsec south					
	MC-EMI	0.19	−0.35	0.07	0.02
1.6 arcsec south					
	MC-EMI	0.00	−0.31	0.31	0.13
1.8 arcsec south					
	MC-EMI	0.20	−0.35	0.07	0.13
2.0 arcsec south					
	MC-EMI	0.06	−0.14	0.14	0.18
2.2 arcsec south					
	MC-EMI	0.05	−0.28	0.11	0.12

For all these regions the ELR are consistent with LINERS.
[a][O III]λ5007; [O I]λ6300; [N II]λ6583; [S IIs]λλ6716+6731.
Column 2: emission-line components, as in Table 3.
The values between parentheses are data with low S/N.
The errors/σ in the ELRs are less than 15 per cent.

Table 17. ELRs of the north nuclear regions (at north–south direction, PA = 00°).

Regions	Component	log[O III]/Hβ^a	log[O I]/Hα^a	log[N II]/Hα^a	log[S IIs]/Hα^a
0.2 arcsec north					
	MC-EMI	−0.07	−0.34	–	0.19
0.4 arcsec north					
	MC-EMI	−0.13	−0.12	–	0.26
0.6 arcsec north					
	MC-EMI	−0.21	−0.38	–	−0.10
0.8 arcsec north					
	MC-EMI	−0.25	−0.44	−0.56	−0.13
	MC-EMI	−0.20	−0.29	0.21	0.28
1.0 arcsec north					
	MC-EMI	−0.07	−0.25	−0.12	−0.05
1.2 arcsec north					
	MC-EMI	−0.12	−1.00	−0.25	−0.44
1.4 arcsec north					
	MC-EMI	0.04	−1.10	−0.12	−0.38
1.6 arcsec north					
	MC-EMI	−0.12	−0.90	0.00	−0.20
1.8 arcsec north					
	MC-EMI	−0.09	−0.85	−0.06	−0.12
2.0 arcsec north					
	MC-EMI	−0.10	−0.47	0.00	−0.11
2.2 arcsec north					
	MC-EMI	–	−0.24	0.11	0.13

For all these regions the ELR are consistent with LINERS.
[a][O III]λ5007; [O I]λ6300; [N II]λ6583; [S IIs]λλ6716+6731.
Column 2: emission-line components, as in Table 3.
The errors/σ in the ELRs are less than 15 per cent.

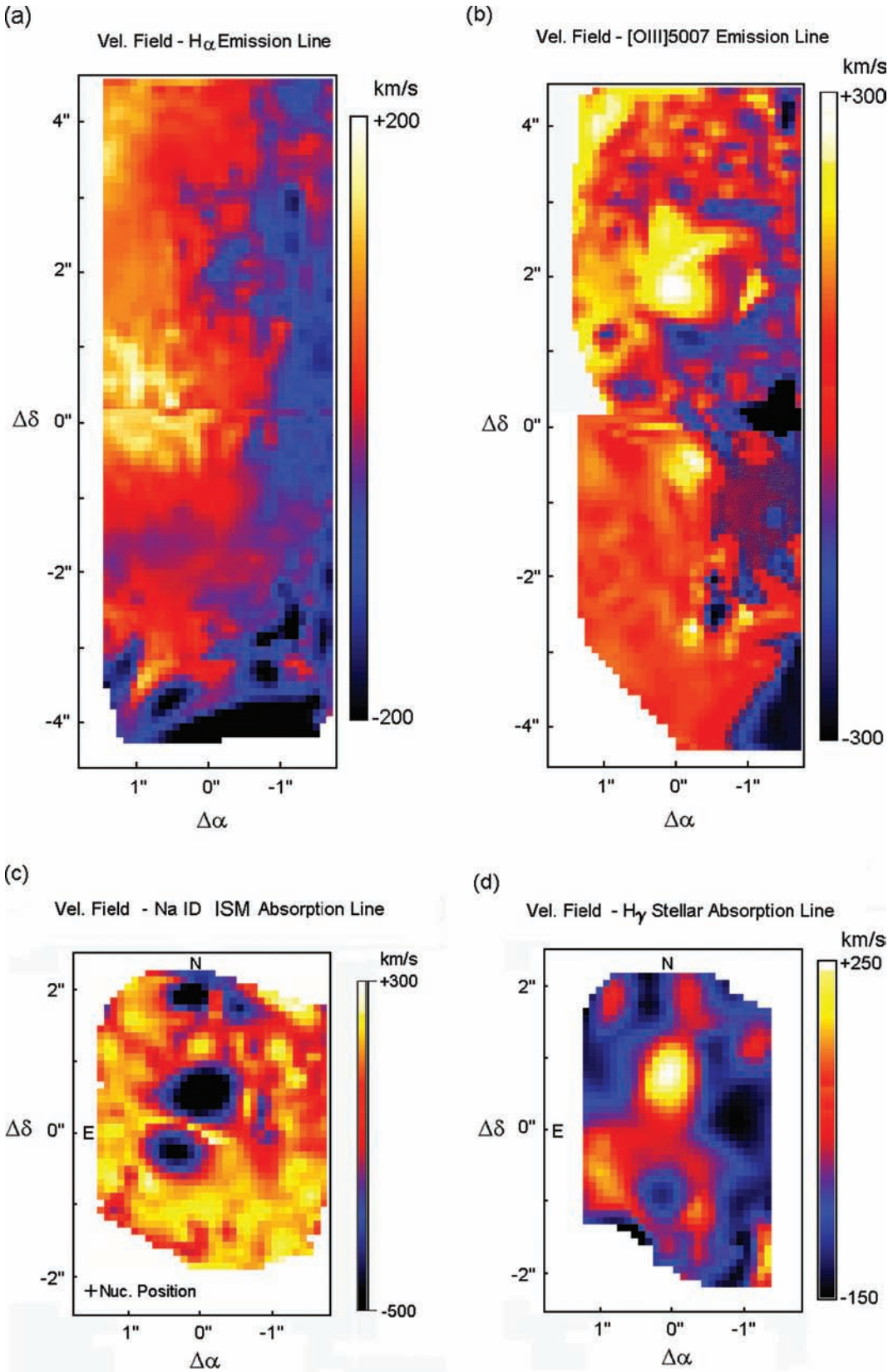

Figure 20. GMOS VF maps (a, b, c, d) for emission and stellar, ISM absorption lines. In the GMOS mosaic maps (a and b) the nucleus is positioned at $\sim\Delta\alpha = 0$ arcsec and $\sim\Delta\delta = +2$ arcsec. For the GMOS one frame maps (c and d) the nucleus is positioned at $\sim\Delta\alpha = 0$ arcsec, and $\sim\Delta\delta = 0$ arcsec. The panel (e) shows the radial velocity curve, for the nuclear region, which was derived from the Hγ stellar absorption VF (panel d).

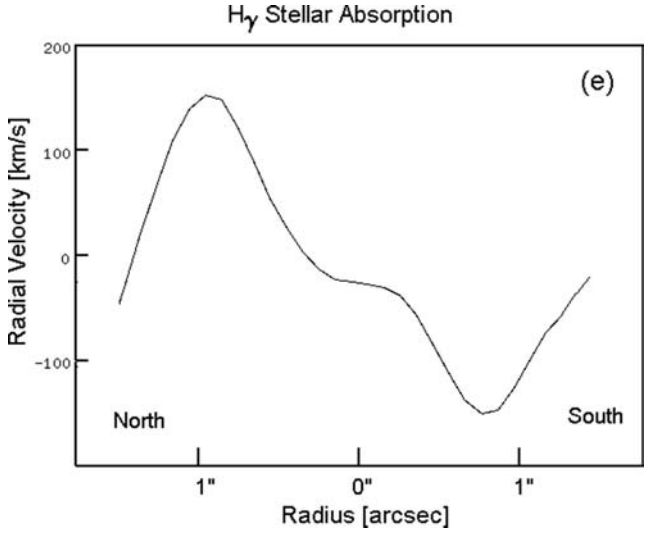

Figure 20 – *continued.*

north-east region. These structures in the VF are in good agreement with the results obtained by Krabbe et al. (1997), using near-IR 3D spectroscopic data.

(iii) At the south-west regions/border of the Hα and [O III]λ5007 VFs the highest blueshifted values were found (close to the position of the complex of H II regions Aconcagua, in the supergiant bubble S1). Thus, these kinematics structures are probably associated with the knots of rupture and blowout process (i.e. the knots K11 + K12 + K14).

Therefore, it is important to remark that – both – the GMOS–IFU and La Palma-Integral 3D spectroscopic studies suggest that the complex Aconcagua is a main point of rupture and blowout of the supergiant shell S1.

12.2 Mapping with GMOS–IFU the ISM kinematics (using the galactic Na ID absorption line)

Fig. 20(c) shows the GMOS VF map obtained from the galactic Na ID absorption line: i.e. the Na ID detected at the systemic velocity of the merger ($cz = 12\,654$ km s^{-1}).

From Fig. 20(c) it is interesting to note the following points.

(i) In all the nuclear and in the nearest circumnuclear area – specially in the core of the nucleus – there is a clear OF process: with two strong blueshifted lobes. This result is clearly consistent with the previous studies of the OF process (in the nuclear region of Mrk 231), which detected extreme velocity OF of ionized gas.

(ii) There is also a weak blueshifted lobe (and filaments) in the north and north-west region, at a radius $r \sim 2$ arcsec. For this area Krabbe et al. (1997) reported several OF and filaments.

12.3 Mapping with GMOS–IFU the stellar kinematic and the nuclear rotation curve

Fig. 20(d) shows the map of the stellar VF from the Hγ absorption line, and for the nuclear region of $\sim$3.5 $\times$ 5.0 arcsec^2 ($\sim$3 $\times$ 4 kpc, with a spatial resolution/sampling of 0.1 arcsec). This field (Fig. 20(d)) cover only the 'nuclear' GMOS–IFU frame; i.e. this plot does not cover all the GMOS mosaic (since the Hγ absorption is very week in almost all the GMOS frame of the southern arc).

In this nuclear stellar VF is evident the presence, close to the core of the nucleus (at 0.8–0.9 arcsec and at PA = 00°), of two symmetric lobes: i.e. a blueshifted circular lobe located to the south (of the core of the nucleus) and a redshifted circular lobe to the north. This is the typical structure of circular motion around the core of the nucleus.

Thus, from this stellar VF and for the region close to the core of the nucleus ($r < 1.4$ kpc) an RC was constructed, using the software ADHOC and the technique already described by Lípari et al. (2004a). Specifically, the RC was obtained from the extraction in the VF of an angular sector of $\pm$ 20° around the line/axis north–south (at PA 00°). The shape of the observed 'nuclear' RC of Mrk 231 – with a monotonic increase in the more external nuclear regions, and after reaching a maximum, a symmetrical fall outwards – has been called a 'sinusoidal' shape (see for details Ruvin & Ford 1983; Zepf 1993; Mendez de Olivera et al. 1998; Lípari et al. 2000, 2004a). In the advanced mergers NGC 3256 and 2623, we already found similar sinusoidal RCs, but at larger scale (i.e. for all the radius of the galaxy/merger). We suggested that this sinusoidal feature could be a common characteristic of advanced major merger systems, and probably associated with OF in the more external regions (Lípari et al. 2000, 2004a,c).

From the RC (Fig. 20e) we derive a Keplerian mass, inside a radius $r = 700$ pc, $M_{\rm dynam}(700\,{\rm pc}) \sim (0.5 \pm 0.2) \times 10^{10}\,{\rm M}_{\odot}$. In order to confirm this result and to analyse more physically the RC, we fitted this nuclear RC with several well-known mass distribution models: following the step and technique described in detail in our study of the RCs of NGC 2623 and 3256 (see Lípari et al. 2000, 2004a,c). The best fit to the nuclear RC was obtained with a Plummer–Kuzmin law (Binney & Tremaine 1987), which correspond to a spherical or disc mass distribution. For the Plummer–Kuzmin potential, we have used the relation

$$\Phi(r) = \frac{-GM_{\rm T}}{\sqrt{r^2 + r_0^2}}, \tag{1}$$

where G is the gravitational constant, $M_{\rm T}$ is the total mass and r_0 is the scalelength corresponding to $r_{\rm max}/\sqrt{2}$, $r_{\rm max}$ being the turnover radius of the RC. The circular velocity in the equatorial plane is, in cylindrical coordinates,

$$V_{\Theta}^2(R, 0) = \frac{GM_{\rm T}R^2}{\left[R^2 + R_0^2\right]^{3/2}}. \tag{2}$$

The best fit was obtained with $M_{\rm T} = M_{\rm TOT.NUC.} = (0.9 \pm 0.1) \times 10^{10}\,{\rm M}_{\odot}$; and with the following geometry PA$_0$ = 00° $\pm$ 5°, $i = 45° \pm 5°$ (a mean value) and $V_{\rm sys} = 12\,650 \pm 10$ km s^{-1}. The value of mass (derived using a Plummer–Kuzmin law) is consistent with the value obtained for a Keplerian mass. For details of the fit process, derived mass, etc. of the CRs and VFs, see the kinematics studies of NGC 2623 and 3256 (Lípari et al. 2004a,c).

Furthermore, it is important to remark that our derived values of the nuclear mass (obtained in this paper and for the inner 0.7 kpc) are within the errors similar, or slightly lower than the value obtained by Downes & Solomon (1998) for the dynamical mass, inside the radius $r = 0.5$ kpc: $1.2 \times 10^{10}\,{\rm M}_{\odot}$. Another interesting point – about this last work – is the fact that the radius of $\sim$0.5 kpc (used by Downes & Solomon 1998, for their study of the mass in the nuclear region of Mrk 231; using CO interferometric-IRAM observations and models), is also the radius of a starburst disc/ring. This CO disc/ring with a starburst could be related or associated with the dusty starburst ring S5. Thus, in general there is a good agreement between the GMOS and IRAM high spatial resolution studies, performed at different wavelength regions and using different techniques.

13 DISCUSSION OF THE GMOS–IFU RESULTS

13.1 Decoupling with GMOS–IFU the very young nuclear starburst from the QSO

13.1.1 The GMOS nuclear extreme blue/starburst component (and the composite evolutionary model for BAL QSOs)

In this paper, using the GMOS–IFU spectra and GALFIT-3D model we found: (i) in the pure host galaxy spectrum an extreme nuclear starburst component (for the first time, at optical wavelength), which was detected as a very strong increase in the flux; (ii) 3D GMOS individual spectra and maps confirm the presence of an extreme blue/starburst component, which was detected in a nuclear dusty ring or toroid.

More specifically, in Section 6 we found in the map of the nuclear blue continuum (or colour index, Fig. 8b) two clear, symmetric and strong peaks, which are located at 0.3 arcsec to the south and to the north, of the core of the nucleus. This position of the peak is coincident with the location of the ring S5. Thus, these two peaks are probably positioned inside of the dusty shell/ring S5. In addition, different previous studies, performed at radio wavelength, already proposed that in this area there is a disc of molecular gas, with extreme SFR of $\sim$100–200 $M_{\odot}$ yr^{-1} (Bryan & Scoville 1996; Downes & Solomon 1998; Carrilli et al. 1998; Taylor et al. 1999).

On the other hand, in these regions (of the blue and red peaks) the individual GMOS spectra show strong and narrow multiple emission-line components (with OF), specially in the lines [O II]λ3727; plus stellar narrow emission and absorption in the IR Ca II triplet. These are clear signature of a very young stellar population. The presence of two strong narrow [O II]λ3727 components could be associated with young H II regions with strong OF.

The strong narrow emission plus absorption in the IR Ca IIλ8500 triplet (detected in the symmetric areas of the red and blue continuum peaks) is clearly associated with the peak of RSGs activity, with age of: 8 < age < 15 Myr (in metal-rich stellar populations; see Terlevich et al. 1991; Lípari & Terlevich 2006). The red continuum peak could be associated with a very dusty region of the nuclear starburst. Furthermore, probably both areas (of the blue and red continuum peaks) are associated with the shell/ring S5.

It is important to remark that the south nuclear and circumnuclear area (with blue continuum) is coincident with the region where we previously suggested that the nuclear GW in Mrk 231 is cleaning the nuclear dust. Specifically, we suggested that the more external supergiant bubble S1 is in the blowout phase: i.e. cleaning all the south area of the whole merger. Probably, for this reason/fact the extreme nuclear starburst is observed.

It is interesting to note that the derived dynamical time for the more external supergiant bubble S1: $\sim 5 \times 10^6$ yr, suggests that this bubble could be generate in the first phases of this very young starburst, which is probably associated with the interaction between the star formation process with the AGN + accretion disc. In addition, it is interesting to note that the last/young starburst activity detected in this merger must have occurred very late in the history of the interaction, since the age of the starburst is only 5–20 $\times$ 10^6 yr. This is in agreement with the results published by Mihos & Hernquist (1996) for models of starburst in disc/bulge/halo major mergers process (their figs 4 and 2), where extended massive star formation processes occurred late in the history of the interaction.

Therefore, the detection of a very young nuclear starburst in Mkr 231 (by the presence of a strong blue continuum flux, the detection of the near-IR Ca II triplet in emission plus absorption, etc.) is a clear confirmation of the proposed *evolutionary and composite model* for young BAL + Fe II + IR QSOs.

13.1.2 The GMOS data of the extended post-starburst (or A-type stellar population)

In Section 11, for the absorption of Hβ, a range of equivalent width of 7–15 Å was obtained. First, this result was analysed using the evolutionary stellar population synthesis models of Gonzalez Delgado et al. (1999). Specifically, we compared the Hβ EqW observed for Mrk 231 with the grid of EqW of the models (for H Balmer and He I lines). The model used corresponds to a cluster with instantaneous burst, solar metallicity and Salpeter IMF, between $M_{\rm low} = 1\,M_{\odot}$ and $M_{\rm up} = 80\,M_{\odot}$. From this study, a range of age of 30–500 Myr was obtained for the A-type stellar population of Mrk 231 and a $T_{\rm eff}$ of 9000 K. This result is in good agreement with the idea that this A-type stellar population could be associated with the first phases of the merger process of Mrk 231. Since, for example the time-scale of mergers with prograde orbit is 0.5 $\times$ 10^9 yr (Noguchi 1991; Barnes 1992).

Then, we have confirmed this result using for the study of the absorption GMOS spectra [for the H Balmer lines: Hβ, Hγ, etc.: the observational templates of stellar clusters populations (Piatti et al. 2002)].

On the other hand, an interesting result obtained in Section 11 is the fact that the regions with strong H Balmer absorption lines show 'arc shape' (which are located very close to the external border of the supergiant shells S1 and S2). A simple explanation for this result could be that the OF process – in these shells – is cleaning the nuclear dust. Thus, this cleaning process is probably the fact that allows us to see clearly – and strongly – the absorptions of this A-type stellar population (close to the external parts of the expanding shells).

13.2 Decoupling with GMOS–IFU the BAL systems: the jet-wind nature of the BAL I and II systems (plus the explosive nature of the BAL III)

13.2.1 The AGN jet-wind and the extended nature of the BAL systems I and II

Main predictions of the AGN and composite models for BALs. In general, there are two groups of models about the structure and dynamics of the gas near the core of AGN. Specifically, in the broad absorption-line region (BALR) and the broad emission-line region (BELR). In these models the gas may exist as: (i) continuous winds: spectral analysis of Arav, Li & Begelman (1994), Arav et al. (1997, 1998, 2001, 2005) seems to show that continuous winds might be better suited to explain high-resolution spectra of BALR and BELR; (ii) discrete clouds: the idea that gas is partitioned into discrete clouds is the more traditional approach to BELR and BALR (see Bottorff et al. 1997; Everett, Konigl & Kartje 2000).

The two main AGN theoretical models for BALs (jets and accretion discs) predict some clear effects that could be detected with high spatial and spectral resolution observations (and with high-quality/SN spectra). The deep GMOS–IFU data presented in this paper are probably one of the best and most complete set of data available to date for this purpose. Furthermore, these GMOS data were obtained for the nearest BAL QSO.

Specifically, these two models predict some very simple and clear effects (see for a discussion of this point Murray et al. 1995; Punsly

1999a,b; Proga, Stone & Kallman 2000a; Punsly & Lípari 2005). Here, we present a summary of the most clear prediction of these two AGN models.

(i) *Jet model for BAL*: This model predicts that the jet wind is collimate, bipolar and aligned with the jet direction. Thus any possible elongation will be detected in the jet direction. It is important to note that in order to detect any elongation in a BAL system, an extended nature of the studied BAL it is required, in a scale similar to the spatial resolution of the instrument (for GMOS ∼0.4–0.5 arcsec). Different effects could explain the extended nature of some BALs (Punsly & Lípari, in preparation).

(ii) *Accretion disc model for BAL*: In this second model the accretion disc wind is located close to the plane of the disc, i.e. for AGN with detected jets, the wind associated with accretion disc is located perpendicular to the direction of the jet. Thus, any possible elongation in the BAL will be detected perpendicular to the jet direction.

It is interesting to remark that in the composite + supergiant shell scenario for BALs, some elongations could also be generated. Specially, the elongations could be observed in the case of collimate/bipolar expansion of the GW + supergiant shells. This type of OF could generate elongations at the PA of the direction/axis of the bipolar GW (or hyperwind) + supershells.

The jet-wind nature of the BAL I and II systems. In this paper, we have studied (using high-resolution very deep 3D GMOS spectra) all the optical 'absorption' lines associated with the BAL systems I and II. The deep 3D GMOS spectra and maps clearly show that the BAL system I (in the Ca II Kλ3933 absorption map) and the BAL system II (in the Na ID λ5889–95 absorption map) are clearly elongated at the PA close to the radio jet PA. This strongly suggest that the BAL systems I and II are 'both' associated with the radio jet, and supporting the bipolar jet-wind model for some BALs. Thus, this new study (based on deep GMOS–IFU spectroscopy) is in excellent agreement with the previous 3D integral spectroscopy study of the Hα emission bump.

In addition, the very deep 3D GMOS spectra (Fig. 10) and maps (Fig. 11) clearly show the extended nature of the BAL system I: reaching ∼1.4–1.6 arcsec ∼ 1.2–1.3 kpc, from the nucleus; which are also in excellent agreement with the extended nature found previously (from the 3D integral study of Hα bump) of the BAL I. Furthermore, de Kool et al. (2001, 2002) found similar results – extended nature of two BAL systems – in their Keck high-resolution spectroscopic study of BALs in the QSOs FIRST J104459.6+365605 and FBQS 0840+3633. They found that the distances between the AGN and the region where the OF gas generate the BAL line are at ∼700 and ∼230 pc, respectively. Therefore, for Mrk 231 (BAL system I), FIRST J104459.6+365605 and FBQS 0840+3633 the distances found between BAL forming regions and the continuum source (AGN) are large, ∼200–1400 pc. BALs are generally thought to be formed in OF at a much smaller distance from the nucleus (see for references de Kool et al. 2001).

13.2.2 The explosive nature of the BAL III system

A very important point about the explosive scenario for Mrk 231 is the detection (together with the multiple expanding shells) of an exponential fall in the variability of the short-lived BAL III Na ID system. In this paper, this exponential fall in the BAL III Na ID was confirmed (for almost all the period in which this system appears, 1984–2005), using very deep 2005 GMOS–IFU spectra. The origin of this exponential fall in the BAL III system could be explained, in the framework of an *extreme explosive event*, probably associated with hypernova explosions. An explosive scenario for the origin of the BAL III system could explain also the presence (in the nucleus) of multiple concentric expanding superbubbles with circular shape.

It is important to remark that Lípari et al. (2005) already analysed and discussed – in detail – the main possible explanations for the LC variability of BAL III system in Mrk 231. However, they concluded that only a giant explosive event could explain this SN shape LC (since the other proposed scenarios and models generate mainly symmetric LC variability).

13.2.3 Mrk 231 and the rare class of Fe II and low-ionization BAL QSOs

A very interesting point is the fact that Mrk 231, FIRST J104459.6+365605 and FBQS 0840+3633 (which shows extended BAL systems) are all member of the rare class of low-ionization BAL QSOs. Furthermore, these three QSOs are also member of the 'very' rare subclass of Fe II low-ionization BAL QSOs with very strong reddening in the ultraviolet (UV) continuum. In particular, for Mrk 231 Lípari et al. (2005, their fig. 11a) clearly shows – in the UV spectrum – the presence of strong absorption in the Fe II and Mg II lines; which are the standard lines that define the Fe II low-ionization BAL QSO subclass.

We already suggested that low – and specially Fe II low – ionization BAL QSOs are young and composite/transition QSOs: in the phase that the OF process with GWs, expanding supergiant bubbles and exploding HyN are cleaning the nuclear dust (which is generated, at least in part by the extreme nuclear starburst). Thus, the strong reddening in the UV continuum is also associated with their composite nature. In addition, Lípari (1994) and Lípari et al. (2005) found – in the IR colour–colour evolutionary diagram – a clear sequence of transition BAL + Fe II + IR QSOs, which are – almost all – members of the rare class of *low-ionization BALs QSO* (like Mrk 231; IRAS 075988+6508; IRAS/PG 17002+5153, etc.).

Very recently, from a study of a very large sample of 37 644 SDSS QSOs, from the third Data Release (DR3) and for all redshift (in the range: $0 < z < 5$): White et al. (2006) found that the radio properties of the rare class of low-ionization BALs QSOs are different from the group of non-BAL QSOs + high-ionization BAL QSOs, at all redshifts. This result could be explained in the framework of an evolutionary unified scenario for BAL QSOs, in close agreement with the model proposed by Lípari & Terlevich (2006). Where low-ionization BAL QSOs are young, transition, and composite QSOs in the phase of a strong/composite OF, with supergiant expanding shells (probably associated with exploding HyN and jets); which are cleaning the nuclear dust.

13.3 Decoupling with GMOS–IFU the nuclear OF and the expanding superbubbles, in Mrk 231

In this paper, we have confirmed with high spatial and spectral resolution GMOS data the presence of multiple concentric expanding supergiant bubbles/shells, with centre in the nucleus and highly symmetric circular shape. These shells could be associated with giant symmetric explosive events. These explosive events could be explained in a composite scenario, where the interaction between the starburst and the AGN could generate giant explosive events: i.e. HyN (Artymowicz, Lin & Wampler 1993; Collin & Zahn 1999). Furthermore, we derived for the kinetic energy of the OF of the shell

S1, $E_{\rm KINOF-S1} \sim 2.0 \times 10^{54}$ erg (Lípari et al. 2005). This very high level of kinetic energy, obviously required the presence of multiple SN events, or an unusual type of 'giant SN' or hypernovae (with $E_{\rm KINHyN} > 10^{52}$ erg; see Nomoto et al. 2004, 2006, 2007). This is also in good agreement with the extreme starburst and composite scenario for the nucleus of Mrk 231.

In this paper we have also presented GMOS morphological and kinematics evidence that the main complex of H II regions (K11 + K12 + K14: 'Aconcagua') could be associated to a main point of rupture of the border of the bubble S1 (with a large number of massive/WR stars). In the next subsections this point is discussed in detail.

13.3.1 GMOS evidence of the rupture of the external supergiant shell

In Sections 9, 10 and 12 we have studied the 3D GMOS spectra and images of the main knots of the multiple expanding nuclear bubbles. In particular, we found strong multiple [O III]λ5007 emission and WR features in the main complex (K11 + K12 + K14: '*Aconcagua*') of the more external supergiant bubble S1. These results are in good agreement with those obtained previously, in the sense that the H II region complex 'Aconcagua' is probably associated with a main point of rupture of the bubble.

More specifically, in this paper we found the signature of a large number of WR and very massive stars in the strong knot K14-East associated with a main complex of H II regions, located at the south-west border of the more external supergiant bubble S1. It is important to remark that populations of massive stars are the main progenitors of 'multiple' core–collapse SNe/HyN, which are the main objects capable of generating the rupture phase of the galactic bubbles (Heiles 1979; Norman & Ikeuchi 1989).

Recently, a similar result was found for all the main points of rupture of the supergiant extranuclear bubble in NGC 5514: i.e. the presence of WR stars in all the knots of rupture of the supergiant shell. Furthermore, for NGC 5514 we already proposed that a population of very massive stars (like WRs) could be the source of multiple SN and HyN, and thus also the source of the rupture of the bubble.

Therefore, using deep GMOS–IFU high spatial resolution 3D spectra, we found – in this paper and for the distant IR merger Mrk 231 – very similar results to those previously detected in the nearby merger NGC 5514 (this last object is considered the prototype of a IR merger with a supergiant bubble in the rupture phase).

13.3.2 GMOS data and the nature of the nuclear multiple expanding suprergiant shells

In Sections 9, 10 and 12 we found new interesting results about the physical and kinematics properties of the nuclear expanding bubbles. Here, these properties and the nature of these five nuclear expanding supergiant bubbles/shells are discussed.

Specifically, we remark the following main points.

(i) *Supergiant bubble/shell S1*

In this paper we found strong evidence that this supergiant bubble is in the blowout phase. Furthermore, the typical kinematics, morphological and physical properties of a point of rupture of the bubble were found (in the knot K14-East, of this relatively distant IR merger).

This region of rupture of the bubble S1 (south-west area) and also several knots in the four external supergiant bubbles show clear blueshifted emission, in the OF and – even – in the main components. With a value of OF, of $\Delta V \sim -400$ km s^{-1}.

(ii) *Supergiant bubble/shell S2*

The main/strong knots (of this shell) are all located in the south-west region with typical ELRs of LINER, associated with shocks of low velocity.

(iii) *Supergiant bubble/shell S3*

The knots of this shell show composite values of ELRs, between LINER and H II regions. In addition, the knot S3a (also called K3) shows typical values of ELRs of H II regions.

This last result is in good agreement with that obtained for the near area E1 (where we detected very strong Hα emission), which also shows typical ELRs of H II regions.

(iv) *Supergiant bubble/shell S4*

In this internal bubble – and close to the core of the nucleus, for $r < 0.7$ arcsec ~ 0.6 kpc – two similar narrow emission-line systems were detected, with strong [S II] and [O I] emission (with $\Delta V \sim -200$ km s^{-1}). These results are consistent with ionization by OF + shocks of low velocity and in a dense ISM.

(v) *Ring or toroid S5*

In this paper we found evidence that this ring is probably associated with a toroid of very young and strong star formation process of 8 < age < 15 Myr (see for detail Sections 6 and 7).

13.4 GMOS data and the nature of the nuclear NLR and BLR (in Mrk 231)

In general, the main results obtained in Sections 10 and 12 clearly show that the kinematics, morphology and physical properties of the multiple narrow emission-line systems (in the core of the nucleus and the nuclear region, for $r < 2.2$ arcsec ~ 1.8 kpc) are all consistent with an ionization process generated by the OF with low-velocity shocks. In addition, only few nuclear areas were detected, where the dominant ionization could be associated with H II regions.

More specifically, the following results are consistent with a nuclear NLR associated with the OF gas and with an ionization process by shocks.

(i) In the area close to the core of the nucleus (for $r < 0.7$ arcsec $\sim$ 0.6 kpc), two similar narrow emission-line systems were detected, with strong [S II] and [O I] emission and $\Delta V \sim -200$ km s^{-1}. In addition, even at the core of the nucleus these two emission-line systems were observed.

(ii) In the log [S II]/Hα versus log [O I]/Hα diagram the ELR of the area close to the core of the nucleus ($r < 0.7$ arcsec) also shows a position close to the upper right-hand part of this diagram (specially in the south area).

This fact is consistent with the presence of strong [S II] and [O I] emission; and thus it is consistent with shocks process of low velocities ($\sim$200 km s^{-1}; Shull & McKee 1979; Heckman et al. 1990; Dopita & Southerland 1995).

(iii) All the ELR for the nuclear region (at PA = 00°, and for $r < 2.2$ arcsec ~ 1.8 kpc) are located in the log [S II]/Hα versus log [O I]/Hα diagram in the shock area: of SNR + HH. In the south nuclear region (where we detected the blowout phase of the bubble) the ELR are positioned – again – in the upper right-hand border of this diagram.

Therefore, these results suggest that – in the nuclear and circumnuclear region Mrk 231 – the NLR could be associated with the OF process. It is important to remark that even in dusty IR Galaxies we have found several standard NLRs, in which the nuclear ELRs are

all consistent with ionization by the Seyfert/AGN activity. For example, in IRAS 15480−0344 (Lípari, Bonatto & Pastoriza 1991) we detected a typical standard/Seyfert NLR. In addition, new detailed high-resolution narrow-band images and spectra – of this extended NLR – show only ionization associated with the Seyfert activity (Tsvetanov, private communication). However, this is not the case for the NLR of Mrk 231, where we did not detect any ionization in the NLR associated with the Seyfert activity. For Mkr 231, the ELRs of the NLR are clearly consistent with an ionization process dominated by the OF + shock events.

On the other hand, we already proposed that even the broad line *emission* region of Mrk 231 could be generated by an OF process. In particular, we showed that explosive and OF events (more constant that a single and standard SN) could generate the unusual BLR spectrum observed in the core of the nucleus of Mrk 231 (see for details Lípari et al. 2005 and their fig. 14).

14 THE COMPOSITE HYPERWIND MODEL FOR MRK 231, BAL + IR + FE II QSOS AND LYα BLOBS

In order to analyse the extended nature of the OF of Mrk 231 (and BAL + IR + Fe II QSOs), it is important to remark two previous studies at radio wavelengths, which are important for the discussion of the extended and composite OF process. In particular, we note the following.

(i) VLA images at 4.9 Ghz (Baum et al. 1993) and at 1.5 Ghz (Ulvestad et al. 1999a) show a very large structure of ∼35–50 kpc, elongated in the direction north–south.

(ii) VLBI images at 1.7 Ghz (Neff & Ulvestad 1988; Lonsdale et al. 2003) and VLBA images at 2.3 Ghz (Ulvestad et al. 1999a) show a triple structure with a central unresolved core and two symmetric resolved lobes with a total extension of ∼40 pc. This radio structure is elongated also in the direction north–south.

These results clearly suggest that these extended structures (from scale of few parsec to 50 Kpc) are probably associated with the main components of a composite OF process: the blowout phase of the more external bubble S1 (at PA = 00° and at large/kpc scale). These results (for Mrk 231) are in good agreement with those obtained previously for several BAL + IR + Fe II QSOs: like IRAS 04505−2958 (see Lípari et al. 2007a,b).

14.1 Composite hyperwind model for BAL + IR + Fe II QSOs

In several BAL + IR + Fe II QSOs we detected extended OF processes (similar to the extended Lyα blobs found at very high redshift; by Steidel et al. 2000) which are probably associated with the composite nature of the very nucleus of QSOs/AGN (Lípari et al. 2003, 2005). In particular, Lípari et al. (2005) proposed a *composite hyperwind scenario* in order to explain the very extended blob/shell – of ∼30 kpc – found in the new BAL QSO IRAS 04505−2958.

In addition, in the study of IRAS 07598+6508 and IRAS/PG 17002+5153, Lípari (1994) already suggested that nearby and high-redshift *low–ionization BAL QSOs* could be explained by a violent ejection during the first onset of the QSO activity, similar to a 'giant SN explosion' (previously proposed by Hazard et al. 1984). This approach is very similar to that suggested for Mrk 231, where 'multiple nuclear expanding superbubbles' were found, associated – in part – with giant SN or hypernova explosions. Therefore, it is important to study the possible role of composite hyperwind/OF in the evolution of supermassive black holes (SMBHs) and QSOs.

It is important to remark that very recently our suggestion of the existence of *extreme type IIn SN explosive events* associated with very massive progenitors (like Eta Carinae) was confirmed (Lípari et al. 2003; Lípari & Terlevich 2006). In particular, the discovery of the SN 2006gy (in NGC 1260, Smith et al. 2007), that reached a peak of absolute magnitude of −22, and remain brighter than −21 mag for about 100 d. Thus, this SN (of type IIn) is one of the most luminous SN ever recorded, powered by the death of an extremely massive star like Eta Carinae. This fact confirm one of the main suggestion of the evolutionary and explosive model for composite AGN: the existence of giant SN/HyN explosions, associated with very massive stars. Furthermore, Smith et al. (2007) even proposed that giant SN explosions from very massive progenitors could be more numerous in Population III stars (in young objects and in the early universe) than previously believed. Finally, it is important to remark that this SN 2006gy shows very strong Na ID and H&K Ca II absorption lines (i.e. very similar to those of Mrk 231).

Furthermore, very recently the discovery of new giant SN or HyN similar to 2006gy (SN 2006tf and 2005ap) confirm the presence of extreme explosive events. These type IIn HyNs and their remnant are powered by the death of extremely massive stars could help to explain several main themes in Astrophysics. Specifically, the recently detection of extremely energetic cosmic rays associated with AGN, could be explained in the framework of the explosive, evolutionary and composite model for AGN/QSOs. Since remnant of HyN – a main component of this model – could be a very probable source of extremely energetic cosmic rays (see for references and details Lípari et al. 2007b).

14.2 Composite hyperwind model for Lyα blobs

The ionizing radiation from the newly formed young stars should lead to prominent Lyα emission due to recombination of the hydrogen in the ISM. Thus, extended Lyα emission could be an important spectral signature of young and composite systems, specially at very high z (Terlevich et al., in preparation).

Recently, we have started a study of 3D spectroscopic data of high-redshift submillimtere and radio BAL QSOs, using Gemini + GMOS and ESO VLT + VIMOS. Specifically, we have already performed a detailed study of Gemini GMOS–IFU data of the – low-z – BAL QSO IRAS 04505−2958 and high-redshift submillimetre SDSS BAL QSOs (Lípari et al., in preparation). The result of this paper is the second paper of our Gemini GMOS–IFU programme of BAL QSOs. In general, we found that IRAS 04505−2958 and Mrk 231 show similar extended OF process (of 100 and 50 kpc, respectively). Even both QSOs have 'relatively narrow' – or mini/associated – BALs (see for details Lípari et al. 2007a,b).

Therefore, we are studying if extreme OF associated with giant explosions and hypernovae (plus AGN jets) could generate BAL systems and extended blobs (Lípari 1994; Dey et al. 1997; Guillemin & Bergeron 1997; Tenorio-Tagle et al. 1999; Bond et al. 2001; Lípari et al. 2003; Reuland et al. 2003; Lípari et al. 2005; Punsly & Lípari 2005; Lípari & Terlevich 2006; Lípari et al. 2007a). The main goal of this study is to test our proposed composite hyperwind scenario for some BAL QSOs at low and high redshifts (Lípari & Terlevich 2006; Lípari et al. 2007a,b; see also Magain et al. 2005).

15 THE EVOLUTIONARY END OF Mrk 231, ELLIPTICAL AND QSOs (AND FUTURE WORKS)

The GMOS results obtained for Mrk 231 (combined with theoretical and observational studies, for mergers with OF) suggest that extreme starbursts and extreme GWs play an important role in galaxy/QSO evolution (see Larson 1998; Bromm, Coppi & Larson 1999; Larson 1999; Scannapieco & Broadhurst 2001; Bromm & Loeb 2003; Larson 2003; Lípari & Terlevich 2006; Lípari et al. 2007a).

On the other hand, several results (for the merger Mrk 231) suggest that the nuclei of the colliding galaxies have coalesced into a common nucleus, and that the merger is in a very advanced phase: a relaxed system probably evolving into an elliptical galaxy (see Soifer et al. 2000; Quillen et al. 2001; Lípari et al. 1994; Condon et al. 1991; Hamilton & Keel 1987). Thus, a very interesting point is to follow this evolutionary study of Mrk 231 and similar evolving elliptical galaxies with composite and extreme OF (observed as extreme BAL + IR + Fe II QSOs), even to the end phase of their evolution.

It is important to note that in the last years several possible *links* between *mergers, starbursts, IR QSOs and elliptical* have been proposed. Specifically, Lípari et al. suggested the following evolutionary links.

Merger/s → extreme starburst + GW (inflow + OF) → IR + Fe II + BAL composite/transition QSOs → standard QSOs and elliptical → galaxy remnants.

In this evolutionary sequence a main and interesting step is the end phase, of the evolution of the host galaxies + QSOs. We have started observational and theoretical studies in order to analyse if extreme and explosive OF process – in composite BAL + IR + Fe II QSOs – could be associated with three main steps in the evolution of QSOs and their host galaxies (including the end phases). In particular, we are studying the role of explosive events in the following.

(i) To stop the accretion process in QSOs/SMBHs.

(ii) The formation of satellite and companion galaxies (by explosions).

(iii) To define the final mass of the host galaxies, and even if the explosive nuclear OF is extremely energetic, this process could disrupt an important fraction (or even all) of the host galaxies.

Therefore, giant QSO explosion is an interesting process in order to consider as the base for a first model of galaxy end. Our observational GMOS–IFU results for Mrk 231, IRAS 04505−2958, IRAS/PG 17002+5153, IRAS 07598+6508 and others BAL + IR + Fe II QSOs, plus the theoretical works performed by Ikeuchi (1981), Ostriker & Cowie (1981), Berman & Suchkov (1991) show a good agreement with explosive models for the formation and end of some type of galaxies (which are associated with explosive BAL + IR + Fe II QSOs; see for details Lípari et al. 2007a,b).

16 SUMMARY AND CONCLUSIONS

In this paper we have presented the first results of a study of BAL QSOs (at low and high redshift), based on very deep Gemini GMOS–IFU spectroscopy. In particular, the results obtained for the nearest BAL IR–QSO Mrk 231 are presented. These GMOS data are combined with 3D and 1D spectroscopy (obtained previously at La Palma/WHT, *HST*/FOS and KPNO observatories) and deep *HST* broad-band images of Mrk 231.

The main results and conclusions can be summarized as follows.

(i) For the nuclear region of Mrk 231, the QSO and host galaxy components were modelled, using a new technique of decoupling 3D spectra: GALFIT-3D. From this paper, the following main results were found.

(1) In the pure host galaxy spectrum a strong/extreme nuclear starburst component was clearly observed (for the first time, at optical wavelength), as a very strong increase in the flux, at the blue region.

(2) The BAL system I is observed in the spectrum of the host galaxy, i.e. confirming their extended morphology.

(3) In the clean/pure QSO emission spectrum, only broad lines were detected.

(4) 3D GMOS individual spectra (specially the IR Ca II triplet and [O II]λ3727) and maps confirm the presence of an extreme young nuclear starburst component, which was detected in a toroid or ring at $r = 0.3$ arcsec ~ 200 pc.

(5) The nuclear starburst plus the bubbles are cleaning the nuclear dust, specially in the south region. This area is coincident with the region where we previously suggested that the GW – with superbubble/shells – is in the blowout phase.

(6) On the other hand, the 3D spectra of the knots of the multiple expanding nuclear bubbles were analysed. In particular, we found the following.

(i) Strong multiple emission-line systems (with LINER properties) and WR features in the main knots of the more external superbubble S1. The kinematics of these knots – and the internal bubbles – suggest that these knots are probably associated with a main area of rupture of the supergiant bubble (at the south-west region).

(ii) In the more internal superbubble S4 and close to the core of the nucleus (for $r < 0.7$ arcsec ~ 0.6 kpc), two similar narrow emission-line systems were detected, with strong [S II] and [O I] emission and $\Delta V \sim -200$ km s^{-1}. These results suggest that for the nuclear region an important part of the NLR emission is generated by the OF process (and the associated low-velocity ionizing shocks).

Very deep 3D spectra and maps clearly show that the BAL systems I and II – in the strong 'absorption lines' Na ID λ5889–95 and Ca II Kλ3933 – are extended (reaching ∼1.4–1.6 arcsec ∼ 1.2–1.3 kpc, from the nucleus) and clearly elongated at the PA close to the radio jet PA, which suggest that the BAL systems I and II are 'both' associated with the radio jet, and supporting the bipolar jet-wind model for some BALs.

The composite nature of the BAL systems of Mrk 231 is discussed. In addition, using deep 3D GMOS spectra we have confirmed that the variability LC of the BAL systems III shows an exponential fall, associated with giant explosions.

A *composite hyperwind scenario* (already proposed for BALs) was suggested – in this paper – for the origin of giant Lyα blobs, at high redshift. The importance of studying the end phases of Mrk 231, elliptical galaxies and QSOs (i.e. galaxy remnants) was briefly discussed.

Finally, it is important to remark the interesting fact that these 3D GMOS results are strongly consistent between them, and also with previous works. In particular, the new GMOS results obtained using the new 3D techniques of decoupling the QSOs and host galaxies spectra (GALFIT-3D) show an excellent agreement with the study performed in Sections 6, 7 and 8.4.

ACKNOWLEDGMENTS

This work is based on observations obtained at the Gemini Observatory, which is operated by AURA under cooperative agreement with the NSF-USA on behalf of the Gemini partnership: NSF-USA, PPARC-UK, NRC-Canada, CONICYT-Chile, ARC-Australia, CNPq-Brazil and CONICET-Argentina. This research was based also on observations of La Palma and KPNO observatories, and archive data of the NASA and ESA satellite *HST* (obtained from the archive of ESO Garching and STScI, Baltimore). The authors thank P. Candia and H. Dottori for discussions and assistance. We specially thank the Director of Gemini-North Observatory and the Manager of the Gemini Argentina Office, J. Roy and H. Levato, for the help in the early schedule (and the change of target) of the Gemini GMOS observations, of Mrk 231. Finally, we wish to thank the referee for constructive and valuable comments, which helped to improve the content and presentation of the paper.

REFERENCES

Adams T. F., 1972, ApJ, 176, L1
Adams T. F., Weedman D. W., 1972, ApJ, 172, L19
Akima H., 1978, Trans. Math. Software (ACM), 4, 148
Allington-Smith J. et al., 2002, PASP, 114, 892
Arav N., Li Z., Begelman M., 1994, ApJ, 432, 62
Arav N., Barlow T., Laor A., Blandford R., 1997, MNRAS, 288, 1015
Arav N., Barlow T., Laor A., Sargent W., Blandford R., 1998, MNRAS, 297, 990
Arav N. et al., 2001, ApJ, 561, 218
Arav N., Kaastra J., Kriss G., Gabel J., Proga D., 2005, ApJ, 620, 665
Arribas S., Mediavilla E., Garcia-Lorenzo B., Burgo C., 1997, ApJ, 490, 227
Arribas S., Mediavilla E., Garcia-Lorenzo B., Burgo C., Fuensalida J. J., 1999, A&AS, 136, 189
Artymowicz P., Lin D., Wampler E., 1993, ApJ, 409, 592
Barnes J., 1992, ApJ, 393, 484
Baum S., O'Dea C., Dellacassa D., de Bruyn A., Pedlar A., 1993, ApJ, 419, 553
Berman V. G., Suchkov A., 1991, Ap&SS, 184, 169
Bevington P., 1969, Data Reduction and Error Analysis for the Physical Sciences. McGraw-Hill, New York
Bica E., 1988, A&A, 195, 76
Binette L., Dopita M., Tuohy I., 1985, ApJ, 297, 476
Binney J., Tremaine S., 1987, Galactic Dynamics. Princeton Univ. Press, Princeton, NJ
Bland J., Taylor K., Atherton P., 1987, MNRAS, 228, 591
Boksenberg A., Carswell R., Allen D., Fosbury R., Penston M., Sargent W., 1977, MNRAS, 178, 451
Bond N., Churchill C., Charlton J., Vogt S., 2001, ApJ, 562, 641
Boroson T., Meyer K., 1992, ApJ, 397, 442
Bottorff M., Korista K., Shlosman I., Blandford R., 1997, ApJ, 479, 200
Bromm V., Loeb A., 2003, Nat, 425, 812
Bromm V., Coppi P., Larson R., 1999, ApJ, 527, L5
Bryan P., Scoville N., 1996, ApJ, 457, 678
Canto J., 1984, in Peimbert M., ed., Temas Selectos de Astrofisica. Univ. Nac. Autonoma de Mexico, Mexico, p. 115
Carilli C., Wrobel J., Ulvestad J., 1998, AJ, 115, 928
Collin S., Zahn P., 1999, A&A, 344, 433
Condon J., Huang Z., Yin Q., Thuan T., 1991, ApJ, 378, 65
Cutri R., Rieke G. H., Lebofsky M., 1984, ApJ, 287, 566
de Kool M., Arav N., Becker R., Gregg M., White R., Laurent-Muehleisen S., Price T., Korista K., 2001, ApJ, 548, 609
de Kool M., Becker R., Arav N., Gregg M., White R., 2002, ApJ, 570, 514
Dopita M., 1995, Astrophys. Space Sci., 233, 215
Dopita M., Southerland R., 1995, ApJ, 455, 468
Downes D., Solomon P. M., 1998, ApJ, 507, 615
Dunlop J. S. et al., 2003, MNRAS, 340, 1095
Egami E., Iwamuro F., Maihara T., Oya S., Cowie L., 1996, AJ, 112, 73
Everett J., Konigl A., Kartje J., 2000, in Petterson, Polidan R., Pogge R., eds, ASP Conf. Ser. Vol. 224, Probing the Physics of Active Galactic Nuclei by Multiwavelength Monitoring. Astron. Soc. Pac., San Francisco, p. 441
Filippenko A. V., 1982, PASP, 94, 715
Forster K., Rich R., McCarthy J., 1995, ApJ, 450, 74
Frye B., Broadhurst T., Benitez N., 2002, ApJ, 568, 558
García-Lorenzo B., Acosta-Pulido J., Megias-Fernandez E., 2002, in Rosado M., Binette L., Arias L., eds, ASP Conf. Ser. Vol. 282, Galaxies: The Third Dimension. Astron. Soc. Pac., San Francisco, p. 501
Garcia-Lorenzo B., Sanchez S. F., Mediavilla E., Gonzales-Serrano J., Cristensen L., 2005, ApJ, 621, 146
Guillemin P., Bergeron J., 1997, A&A, 328, 499
Gonzalez Delgado R., Leitherer C., Heckman T. M., 1999, ApJS, 125, 489
Hamann F., Ferland G., 1993, ApJ, 418, 11
Hamilton D., Keel W., 1987, ApJ, 321, 211
Hazard C., Morton D., Terlevich R., McMahon R., 1984, ApJ, 282, 33
Heckman T. M., Armus L., Miley G., 1990, ApJS, 74, 833
Heiles C., 1979, ApJ, 229, 533
Heger A., Woosley S., 2002, ApJ, 567, 532
Ikeuchi S., 1981, PASJ, 33, 211
Jahnke K., 2002, PhD thesis, Univ. Hamburg
Jahnke K., Wisotzki L., Sanchez S. F., Cristensen L., Becker T., Keltz A., Roth M., 2004, Astron. Nachr., 325, 128
Keel W., 1996, ApJS, 106, 27
Kollatschny W., Dietrich M., Hagen H., 1992, A&A, 264, L5
Krabbe A., Colina L., Thatte N., Kroker H., 1997, ApJ, 476, 98
Larson R., 1998, MNRAS, 301, 569
Larson R., 1999, in Favata F., Kaas A., Wilson A., eds, ESA SP-445, Star Formation from the Small to Large Scale. ESA Publications Division, Noordwijk, p. 13
Larson R., 2003, Rep. Prog. Phys., 66, 1651
Lípari S. L., 1994, ApJ, 436, 102
Lípari S. L., Terlevich R., 2006, MNRAS, 368, 1001
Lípari S. L., Bonatto Ch., Pastoriza M., 1991, MNRAS, 253, 19
Lípari S. L., Colina L., Macchetto F., 1994, ApJ, 427, 174
Lípari S. L., Diaz R., Taniguchi Y., Terlevich R., Dottori H., Carranza G., 2000, AJ, 120, 645
Lípari S. L., Terlevich R., Diaz R., Taniguchi Y., Zheng W., Tsvetanov Z., Carranza G., Dottori H., 2003, MNRAS, 340, 289
Lípari S. L., Mediavilla E D. R., Garcia-Lorenzo B A. J., Agüero M., Terlevich R., 2004a, MNRAS, 348, 369
Lípari S. L. et al., 2004b, in Storchi Bergmann T., Ho L., Schmitt H., eds, ASP Conf. Ser., IAU Symp. 222, The Interplay Among Black Hole Stars and IGM in Galactic Nuclei. Astron. Soc. Pac., San Francisco, p. 529
Lípari S. L. et al., 2004c, MNRAS, 354, L1
Lípari S. L. et al., 2004d, MNRAS, 355, 641
Lípari S. L., Terlevich R., Zheng W., Garcia-Lorenzo B., Sanchez S. F., Bergmann M., 2005, MNRAS, 360, 416
Lípari S. L. et al., 2006, Bol. AAA Meeting, 49, 267
Lípari S. L. et al., 2007a, in Benaglia P., Cellone S., eds, Workshop of Theoretical Astronomy in Argentina, p. 55 (arXiv:0707.1493)
Lípari S. L. et al., 2007b, Bol. AAA Meeting, 50, 259 (arXiv:0712.0288)
Lonsdale C. J., Lonsdale C. J., Smith H., Diamond P., 2003, ApJ, 592, 804
Magain P., Latawe G., Courbin F., Jablonka P., Jahnke K., Meyland J., Wizotski L., 2005, Nat, 437, 381
Maiolino R., Juarez Y., Mujica R., Nagar N., Oliva E., 2003, ApJ, 596, L155
Maiolino R., Oliva E., Ghinassi F., Pedani M., Mannucci F., Mujica R., Juarez Y., 2004a, A&A, 420, 889
Maiolino R., Schneider R., Oliva E., Bianchi S. Ferrara A.Mannucci F., Pedani M., Roca Sogorb M., 2004b, Nat, 431, 533
Markarian B. E., 1969, Astrophyzika, 5, 286
Mendez de Olivera C., Plana H., Amram P., Bolte M., Boulesteix J., 1998, ApJ, 507, 691
Mihos C., Hernquist L., 1996, ApJ, 464, 641
Murray N., Chiang J., Grossman S., Voit G., 1995, ApJ, 464, 641
Neff S., Ulvestad J., 1988, AJ, 96, 841

Noguchi M., 1991, MNRAS, 251, 360
Nomoto K., Maeda K., Mazzali A., Umeda H., Deng J., Iwamoto K., 2004, in Fryer C., ed., Stellar Colapse. Kluwer, Dordretch, p. 277
Nomoto K., Tominaga N., Umeda H., Kobayashi Ch., Maeda K., 2006, in Langanke K., ed., Special Issue on Nuclear Astrophysics, preprint (astro-ph/0605725)
Nomoto K., Tanaka M., Tominaga N., Maeda K., Mazzali P., 2007, New Astron. Rev., in press (arXiv:0707.2219)
Norman C., Ikeuchi S., 1989, ApJ, 395, 372
Osterbrock D., Cohen R., 1982, ApJ, 261, 64
Ostriker B., Cowie S., 1981, ApJ, 243, L127
Peng C. Y., Ho L., Impey C., Rix H., 2002, AJ, 124, 266
Piatti A., Bica E., Claria J., Santos J., Ahumada A., 2002, MNRAS, 335, 233
Plana H., Bouleteix J., 1996, A&A, 307, 391
Proga D., Stone J., Kallman T., 2000a, ApJ, 543, 686
Proga D., Stone J., Kallman T., 2000b, ApJ, 543, 685
Punsly B., 1999a, ApJ, 527, 609
Punsly B., 1999b, ApJ, 527, 624
Punsly B., Lípari S., 2005, ApJ, 623, L101
Quillen A., McDonald C., Alonso-Herrero A., Lee A., Shaked S., Rieke M., Rieke G., 2001, ApJ, 547, 129
Rieke G. H., Low F., 1972, ApJ, 176, L95
Rieke G. H., Low F., 1975, ApJ, 200, L67
Reuland M. et al., 2003, ApJ, 532, 170
Roederer J. G., 1963, Mecanica Elemental. Editorial Eudeba, Buenos Aires
Rudy R., Foltz C., Stocke T., 1985, ApJ, 288, 531
Rupke D., Veilleux S., Sanders D., 2002, ApJ, 570, 588
Ruvin V., Ford W., 1983, ApJ, 271, 556
Sanchez S. F., 2004, Astron. Nachr., 325, 167
Sanchez S. F., 2006, Astron. Nachr., 327, 850
Sanchez S. F., Cardiel N., 2005, Calar Alto Newslett., 10
Sanchez S. F., Garcia-Lorenzo B., Mediavilla E., Gonzales-Serrano J., Cristensen L., 2004, ApJ, 615, 156
Sanchez S. F., Garcia-Lorenzo B., Jahnke K., Mediavilla E., Gonzales-Serrano J., Cristensen L., Wisotzqui L., 2006a, New Astron. Rev., 49, 501
Sanchez S. F., Garcia-Lorenzo B., Jahnke K., Mediavilla E., Gonzales-Serrano J., Cristensen L., Wisotzqui L., 2006b, Astron. Nachr., 327, 167
Scannapieco E., Broadhurst T., 2001, ApJ, 549, 28
Shull M., 1980, ApJ, 237, 769
Shull M., McKee C. F., 1979, ApJ, 227, 122
Smith N. et al., 2007, ApJ, 666, 1116
Soifer B. et al., 2000, AJ, 119, 509
Sprayberry D., Foltz C., 1992, ApJ, 390, 39
Steidel C. et al., 2000, ApJ, 532, 170
Surace J., Sanders D., Vacca W., Veilleux S., Masarella M., 1998, ApJ, 492, 116
Taylor G., Silver C., Ulvestad J., Carrilli C., 1999, ApJ, 519, 185
Tenorio-Tagle G., Silich S., Kunth D., Terlevich E., Terlevich R., 1999, MNRAS, 309, 332
Terlevich E., Diaz A., Terlevich R., 1991, MNRAS, 242, 271
Turnsheck D., Monier E., Sirola C., Espey B., 1997, ApJ, 476, 40
Ulvestad J., Wrobel J., Carilli C., 1999a, ApJ, 516, 127
Ulvestad J., Wrobel J., Roy A., Wilson A., Falcke H., Krichbaun T., 1999b, ApJ, 517, L81
Veilleux S., Bland-Hawthorn J., Tully R., Filippenko A., Sargent W., 1994, ApJ, 433, 48
Veron M., Joly M., Veron P., Boroson T., Lípari S., Ogle P., 2006, A&A, 451, 851
Voit G., Weymann R., Korista K., 1993, ApJ, 413, 95
Wisotzki L., Becker T., Christensen L., Helms A., Jahnke K., Keltz A., Roth M., Sanchez S. F., 2003, A&A, 408, 455
Wisotzki L., Schechter P., Chen H., Richstone D., Jahnke K., Sanchez S. F., Reimers D., 2004, A&A, 419, L31
White R., Helfand D., Becker R., Glikman E., Vries W., 2006, ApJ, 654, 99
Zepf S., 1993, ApJ, 407, 448

APPENDIX A: THE GALFIT-3D METHOD FOR DECOUPLED THE QSO AND HOST GALAXY 3D SPECTRA

The method developed to decouple the host and the nucleus spectra is an extension of what has been done for decades to decouple the host and the nucleus in the analysis – of these kinds of objects – based on direct imaging (e.g. Dunlop et al. 2003; Peng et al. 2002; Sanchez et al. 2004, and references therein). It has been extended to integral field spectroscopy and tested over simulations and real data sets with different objects, and generalized to decouple the spectra in crowded fields. In this paper (Section 5), we have quoted several references about published studies where the technique GALFIT-3D is theoretical described and observational tested (see for details Sanchez & Cardiel 2005; Garcia-Lorenzo et al. 2005).

In Section 5, we have explained that in general the GALFIT-3D method comprise a fit of the 3D spectroscopic data using a narrow Gaussian function (to model the nucleus) and a de Vocouleur law (to model the galaxy), both deconvolved with a PSF. Thus, a main and first step – in this method – is to obtain the best PSF. For Mrk 231, a PSF was derived – in this paper – at any wavelength range based on the shape of the broad line region of the nucleus, know to whatever extended to be always point-like. Therefore at whatever wavelength the nuclear part may be characterize as a PSF convolved with a delta function, which can be described analytically as a very narrow Gaussian function (with an FWHM of the fraction of the pixel). Any computational convolution in general, and the one performed by GALFIT-3D in particular, it is not an exact computation, and we cannot narrow the Gaussian to the infinite. In order to know which is the best width for this Gaussian function, we fit the PSF with a Gaussian function convolved with itself. The derived width would be the maximum accuracy that can produce GALFIT-3D when a PSF is fitted to itself.

We did not use a pure Gaussian function to characterize the nuclear emission, but a narrow Gaussian (i.e. almost a delta function), convolved with the empirically derived PSF. This is the best possible characterization of the nuclear region and it does not underestimate the extent of the winds of the PSF, since it is included in the modelling. Even more, the galactic profile is also convolved with such a PSF in the fitting process.

In relation to the assumed model, we consider that the object data cube is characterized by

$\mathrm{Obj}(x,y,\lambda) = \mathrm{Nucleus}(x,y,\lambda) + \mathrm{Gal}(x,y,\lambda) + \mathrm{Irr}(x,y,\lambda)$, where 'Obj' is the data set, 'Nucleus' is the nuclear component, 'Gal' is the smooth component of the galaxy and 'Irr' is the irregularities or substructures. For years it is assumed that

$\mathrm{Irr} \ll \mathrm{Nuc} + \mathrm{Gal}$.

Therefore it is possible to model the object with two analytical functions, including one for the nucleus and one of the galaxy, and that the irregularities are entering the rms of the fitting process. The real representation of the host galaxy would not be just 'Gal', but 'Gal + Irr', being the Nucleus just subtracted.

In the characterization of 'Gal' the morphological parameters must be kept correlated with the wavelength since no galaxy is known to change abruptly its general morphology, but to change smoothly from blue to red. We admit that on the wavelength regions dominated by gas emission it may be the case that the irregularities, as defined before, may be of the order of the galaxy flux (Irr $\sim$ Gal), and it is due to that that keeping correlated the morphological parameters it is possible to derive and integrated flux for the smooth component of the galaxy at this wavelength (Gal), which we decouple them from any substructures (Irr).

Thus, the GALFIT-3D method is an extension to 3D of the method used for decades to detect substructures in galaxies, which subtract the smooth component, that describe the average properties of the galaxy.

APPENDIX B: DIFFERENTIAL ATMOSPHERIC REFRACTION CORRECTION

A relevant advantage of integral field spectroscopic observations is the following fact: using IFS data is possible to determine and – in many cases – to correct the spectra from the effects of DAR. For long-slit spectroscopic observations the presence of DAR impose strong restrictions which can not be easily corrected (Arribas et al. 1999). By using IFS data is possible to estimate and correct in the spectra this effect of DAR, since the information is spread all over de IF unit (see Arribas et al. 1999, for a detailed description of DAR correction of IFU data).

Using IFU data, the DAR could be corrected with theoretical formulae or with empirical methods. Filippenko (1982) presents a summary of the theory behind the estimation of differential/relative atmospheric refraction correction. This theory assumes that the layer of different refraction index in the atmosphere is infinitely flat, parallel between themselves and perpendicular to the zenith. These three assumptions are just right to the first order, and have produces errors in the DAR derivation and correction, especially for high air masses. Telescopes are normally mounted on peaky mountains and in many cases in islands nearby the sea. In both cases the assumption that the layers are infinitely flat and parallel is not right. The low layers of the atmosphere, responsible of a considerable amount of the DAR, follow the shape of the mountain rather than being flat. Extensive campaigns with PMAS at the 3.5-m telescope on Calar Alto Observatoy has demonstrate that we have two optical zeniths (defined as the locations of minimal DAR), instead of just one, and only one of them coincident with the zenith of the telescope. We performed comparisons between the DAR derived using the Filippenko formulae and the one provided by a direct estimation on real data based on calibration stars observed during several campaigns, using the procedure described in this paper. There are severe deviations between both derivations that strongly recommend us to use an empirical DAR correction when is possible (i.e. using 3D spectroscopy/IFU).

Thus, using high-resolution GMOS–IFUs spectroscopy with small field of views covering large wavelength ranges, it is important to use empirical DAR corrections (since the use the theoretical formulae could be incorrect).

This paper has been typeset from a TEX/LATEX file prepared by the author.